

2023-08-01

Biomass-Mediated Metastable Zinc(ii) Oxide Nanoparticles And Its Nanocomposites For Sustainable Water Treatment

Kazi Afroza Sultana
University of Texas at El Paso

Follow this and additional works at: https://scholarworks.utep.edu/open_etd



Part of the [Environmental Engineering Commons](#)

Recommended Citation

Sultana, Kazi Afroza, "Biomass-Mediated Metastable Zinc(ii) Oxide Nanoparticles And Its Nanocomposites For Sustainable Water Treatment" (2023). *Open Access Theses & Dissertations*. 3942. https://scholarworks.utep.edu/open_etd/3942

This is brought to you for free and open access by ScholarWorks@UTEP. It has been accepted for inclusion in Open Access Theses & Dissertations by an authorized administrator of ScholarWorks@UTEP. For more information, please contact lweber@utep.edu.

BIOMASS-MEDIATED METASTABLE ZINC(II) OXIDE NANOPARTICLES AND ITS
NANOCOMPOSITES FOR SUSTAINABLE WATER TREATMENT

KAZI AFROZA SULTANA

Doctoral Program in Environmental Science and Engineering

APPROVED:

Juan C. Noveron, Ph.D., Chair

Peter Golding, Ph.D.

Musa J. Hussein, Ph.D.

Jose A. Hernandez-Viezcas, Ph.D.

Stephen L. Crites, Jr., Ph.D.
Dean of the Graduate School

Copyright ©

by

Kazi Afroza Sultana

2023

Dedication

This dissertation is dedicated:

To my parents, whose love and guidance laid the solid foundation of my academic journey.

To my husband, whose support and encouragement pushed my abilities to reach this milestone.

To my kids, whose unconditional love, and sacrifices motivated me to accomplish this goal.

BIOMASS-MEDIATED METASTABLE ZINC(II) OXIDE NANOPARTICLES AND ITS
NANOCOMPOSITES FOR SUSTAINABLE WATER TREATMENT

by

KAZI AFROZA SULTANA, M.S.

DISSERTATION

Presented to the Faculty of the Graduate School of

The University of Texas at El Paso

in Partial Fulfillment

of the Requirements

for the Degree of

DOCTOR OF PHILOSOPHY

Department of Environmental Science and Engineering

THE UNIVERSITY OF TEXAS AT EL PASO

August 2023

Acknowledgments

I would like to express my deepest gratitude and sincere appreciation to my advisor, Dr. Juan C. Noveron for his guidance and support throughout my Ph.D. journey. His expertise, depth of knowledge, and mentoring skills broadened my boundaries and played an important role in shaping my academic development. Being able to work in this lab with full access to the resources and instruments will facilitate the development of vital skills required for my professional endeavors.

I sincerely thank the members of my dissertation committee, Dr. Peter Golding, Dr. Musa J. Hussein, and Dr. Jose A. Hernandez-Viezcas, for their valuable advice and suggestions during conducting research projects and working on my dissertation.

I am grateful to Dr. Mahesh Narayan, Dr. Jorge Gardea-Torresdey, Dr. Alejandro Meta, and Dr. David Roberson for giving me access to the instruments in the lab.

To all the people in the lab, I have worked with them, who created a collaborative environment, and shared their knowledge, I would like to express my heartfelt appreciation to them. I am deeply grateful for the countless and enriching brainstorming conversations we've shared, which have not only contributed significantly to my academic learning but have also made the entire learning journey an immensely enjoyable and rewarding experience.

A special acknowledgment to Dr. Md Tariqul Islam, Dr. Md Ariful Ahsan, Dr. Luis Barrera, Javier Hernandez Ortega, and Liliana Cuevas for their friendship, collaboration, and assistance during my work in the lab.

I am truly grateful to Environmental Science and Engineering program for the funding support throughout my study. The knowledge I have gained through this program will undoubtedly shape my professional path.

Finally, I would like to thank my beautiful family and friends who were always there for me as a constant source of support and motivation during the Ph.D. journey. I consider myself incredibly fortunate to have each one of you in my life.

Abstract

Water is undeniably the most crucial resource that allows all living entities to thrive and survive. Due to a continuously growing population and the expansion of industrial sectors, water pollution has emerged as a global issue. Consequently, people face challenges in obtaining the required quantity and quality of water for their daily activities such as drinking, cooking, hygiene, and agriculture. Hence, there is a compelling need to develop an effective and environmentally friendly approach to eliminate harmful pollutants in water, promoting the establishment of a sustainable society with widespread access to clean and safe water resources. Although there are a lot of existing available water treatment facilities to ensure the provision of potable water, the establishment and maintenance of such facilities come at a significant cost with advanced instrumentation and labor-intensive techniques. To effectively address these issues, the integration of advanced functional nanomaterials, coupled with the application of nanotechnology could facilitate the potential solutions for the wastewater treatment processes. This approach can contribute to the advancement of water treatment technologies and the development of sustainable water management strategies. This dissertation primarily focuses on a sustainable method of synthesizing, characterizing, and evaluating the properties of nanomaterials, specifically metal oxide nanoparticles and their nanocomposites to contribute to the water treatment processes.

Chapter 2 presents a sustainable and reproducible approach for preparing zinc oxide nanoparticles (ZnO) using sawdust as a sacrificial template. The synthesized ZnO nanoparticles exhibit a porous morphology, which enhances their effectiveness in the photocatalytic degradation of the organic pollutant Methyl Orange (MO). The study reveals that the ZnO nanoparticles demonstrate nearly equal activity in both deionized water (DIW) and simulated fresh drinking water (FDW) under UV-B light irradiation.

Chapter 3 reports a facile and fast synthesis method of ZnO through the aerobic combustion of saccharides such as glucose, fructose, starch, and dextrin. This synthesis approach results in the formation of ZnO nanoparticles with high surface area and surface energy, contributing to their enhanced photocatalytic activity in MO degradation under UV-B light and sunlight irradiation.

Chapter 4 introduces a modified method for synthesizing ZnO nanoparticles, aiming to improve their photocatalytic performance in degrading MO under both UV light and sunlight. The modified synthesis approach resulted in ZnO nanoparticles that exhibited higher efficiency by increasing the surface area and crystallinity of nanoparticles in degrading MO compared to the ZnO synthesized in the previous chapter.

Chapter 5 presents, a novel and facile method for synthesizing a regenerable adsorbent, Zinc Oxide, and Carbon Nanocomposite (ZnO@C) by the combustion method. This composite is designed for the efficient removal of anionic and cationic organic pollutants Methyl Orange (MO), Methylene Blue (MB), Congo Red (CR), and Bisphenol A (BPA) from water through adsorption. The maximum adsorption capacity of the ZnO@C composite was determined to be 345 mg/g for MO, 286 mg/g for MB, 244 mg/g for CR, and 345 mg/g for BPA, respectively. With its high adsorption potential for organic pollutants, these nanocomposites hold great promise for water purification applications.

Table of Contents

Dedication	iii
Acknowledgments	v
Abstract	vii
Table of Contents	ix
List of Tables	xiii
List of Figures	xiv
List of Illustrations	xvii
Chapter 1: Multifunctional Nano Materials for Sustainable Water Treatment Processes	1
1.1. Introduction	1
1.2. Water Contamination	2
1.3. Water Treatment Processes	6
1.4. Objectives and Contributions	9
Chapter 2: Sustainable Synthesis of Zinc Oxide Nanoparticles for Photocatalytic Degradation of Organic Pollutants and Generation of Hydroxyl Radical	13
2.1. Introduction	13
2.2 Materials and Methods	16
2.2.1 Materials	16
2.2.2. Characterization Techniques	17
2.2.3 Synthesis of ZnO Nanoparticles	18
2.2.4. Photodegradation Experiments	19
2.2.5 Terephthalic Acid Photoluminescence Test	20
2.3. Results and Discussions	20
2.3.1. SEM images, EDX, and ICP-OES Elemental Analysis of ZnO Nanoparticles	22
2.3.2. XRPD Pattern of ZnO Nanoparticles	24
2.3.3. TEM images of ZnO Nanoparticles	26
2.3.4. UV-Visible Spectrum of ZnO Nanoparticles	27

2.3.5. Photocatalytic Degradation of Methyl Orange	29
2.3.6. Cyclic Stability and Reproducibility of the Method of ZnO-n Preparation.....	34
2.3.7. Determination of the ROS Generated in the Photocatalytic Process	35
2.3.8. Proposed Mechanism for the Photocatalytic Degradation of Organic Pollutants.....	37
2.4. Conclusions and Summary	39
Chapter 3: Preparation of Metastable Zinc Oxide Nanoparticles with High Photocatalytic Activity for Water Decontamination and Sanitation	40
3.1. Introduction.....	40
3.2. Materials and Methods.....	43
3.2.1. Materials	43
3.2.2. Characterization Instrumentation	44
3.2.3. Synthesis of ZnO NPs.....	44
3.2.4. Methyl Orange (MO) Photodegradation Reaction Procedure	45
3.2.5. Fluorescence Test for the Hydroxyl Radicals Detection	46
3.3. Results and Discussion	46
3.3.1. TEM Analysis of the ZnO NPs.....	49
3.3.2. SEM Image and EDX Spectrum of the ZnO NPs.....	50
3.3.3. UV–visible Spectrum of the ZnO NPs.....	52
3.3.4. XRPD Analysis of the ZnO NPs.....	54
3.3.5. XPS Analysis of the ZnO NPs.....	55
3.3.6 Photocatalytic Degradation of Methyl Orange (MO).....	56
3.3.7. Determination of ROS generation by the ZnO NPs.....	63
3.2.8. Mechanism •OH Generation and the Organic Pollutants Degradation.....	65
3.2.9. Cyclic Stability of the ZnO NPs.	66
3.4. Conclusions.....	66
Chapter 4: Method Development for the Synthesis of ZnO Nanoparticles to Improve Photocatalytic Performance Under UV Light and Sunlight.	68
4.1. Introduction.....	68
4.2. Materials and Methods.....	70
4.2.1. Materials	70

4.2.2. Characterization Techniques.....	71
4.2.3. ZnO NPs Synthesis	72
4.2.4. Photocatalytic Degradation Experiments Procedure	73
4.3. Results and Discussion	73
4.3.1. SEM and EDX Spectrum of the ZnO NPs.....	74
4.3.2. TEM Images of the ZnO NPs	75
4.3.3. XRD of the ZnO NPs.....	76
4.3.4. XPS of the ZnO NPs.....	78
4.3.5. MO Photodegradation Reaction under UV-B Light	79
4.3.6. MO Photodegradation Reaction under Sunlight.....	81
4.4. Synthesis of Transition Metal Doped ZnO NPs	82
4.5. Surface Coating of Clay Pot Interior using ZnO NPs.....	85
4.6. Conclusion	87
Chapter 5: Adsorptive Removal of Methyl Orange, Methylene Blue, Congo Red, and Bisphenol A from Water using Zinc Oxide and Carbon Nanocomposite.	89
5.1. Introduction.....	89
5.2. Materials and Methods.....	91
5.2.1. Materials	91
5.2.2. Characterization Techniques.....	92
5.2.3. Preparation of the ZnO@C Nanocomposite	92
5.2.4. Batch Adsorption Experiments	94
5.3. Results and Discussions.....	95
5.3.1. SEM and EDX Spectrum of the ZnO@C Nanocomposite	95
5.3.2. TEM image of the ZnO@C Nanocomposite	96
5.3.3. XRD of the ZnO@C Nanocomposite	98
5.3.4. XPS of the ZnO@C-2 Nanocomposite.....	100
5.3.5. Adsorption Capacity of ZnO@C-2 for MO, MB, CR, and BPA.....	102
5.3.6. Adsorption Isotherms (Langmuir and Freundlich) Model.....	103
5.3.7. Adsorption Kinetics	106
5.3.8. Adsorption Thermodynamics.....	107

5.4. Regeneration Study of ZnO@C-2 Nanocomposite	108
5.5. Quantification of the Percentage of Carbon and ZnO from ZnO@C Nanocomposite	113
5.6. Photodegradation Of MO using ZnO Derived from ZnO@C	114
5.7. Conclusion	116
Chapter 6: Conclusion and Future Directions.....	118
References.....	120
Appendix.....	153
Vita.....	154

List of Tables

Table 1.1: Structure of targeted pollutants.....	9
Table 2.1 Summary of the photocatalytic degradation of MO in different water matrices on the ZnO-n.....	33
Table 3.1: Rate constants of all the photocatalytic reactions performed in this study.....	62
Table 5.1: Experimental parameters for the batch adsorption study of MO, MB, CR, and BPA.	95
Table 5.2: Atomic % of elements calculated through XPS and key molar ratios.....	100
Table 5.3: Binding energy of the sample.	100
Table 5.4: Percentage of the carbon combustion and the remaining ZnO content after the carbonization process.....	114

List of Figures

Figure 1.1: a) 2d chemical structure or skeletal formula of water molecule showing bond angle and bond length, b) 3d image of a water molecule.	1
Figure 1.2: Earth's Water Distribution.	3
Figure 1.3: Sources of pollutants in water.	5
Figure 1.4: Wastewater treatment methods.	6
Figure 1.5: Photocatalytic degradation and adsorption for treatment processes.	8
Figure 2.1: a) Typical SEM image of ZnO-4, b) EDX spectra of ZnO-4 showing the elemental composition, c) SEM backscattered electron image of ZnO-4, d) X-ray EDS mapping image of zinc, e) X-ray EDS mapping image of oxygen, and f) X-ray EDS mapping image of calcium. ..	23
Figure 2.2: XRPD pattern of the ZnO-n (n=1-4), ZnO-control, and sawdust oxides (SDO) showing their crystallinity.....	25
Figure 2.3: a-b) TEM images of ZnO-4 with two different magnifications. Inset: Size distribution of the ZnO-4 based on the TEM image 2b.	27
Figure 2.4: a) UV-visible absorption spectrum of ZnO-n and SDO suspension in ethanol and b) Tauc plot for the determination of bandgap of ZnO-n.....	28
Figure 2.5: Time-dependent a) UV-visible spectrum of MO solution during photocatalysis by ZnO-4 in DIW, b) percent degradation of MO by different ZnO-n catalysts, c) Pseudo-first order kinetics of the degradation of MO, and d) digital photograph showing the gradual decolorization of MO solution during the photocatalysis by ZnO-4.	30
Figure 2.6: Time-dependent a) UV-visible spectrum of MO solution in simulated FDW during the photocatalysis by ZnO-4, b) percent degradation of MO by different ZnO-n catalysts, and c) Pseudo-first order kinetics of the photocatalytic degradation of MO.	32
Figure 2.7: a) Cyclic stability of the ZnO-4 for MO degradation and b) Photocatalytic activity of ZnO-4 prepared in three independent trials.	35
Figure 2.8: a) Reaction of terephthalate with •OH radical to form 2-hydroxy terephthalate, b) Time-dependent fluorescence spectrum of the 2-hydroxy terephthalate solution catalyzed by ZnO-2 (as a representative), and c) kinetics (fluorescence intensity at 425 nm Vs time) of the generation of •OH radical by different catalysts.	37
Figure 3.1: TEM images of the ZnO NPs a) Dextrin-ZnO, b) Fructose-ZnO, c) Glucose-ZnO, d) Starch-ZnO, and e) the average size of the ZnO NPs based on the TEM image.	50
Figure 3.2: SEM Image and EDX Spectrum of the ZnO NPs.	50
a) SEM image of the Glucose ZnO; b) SEM backscattered electron images of the ZnO NPs; c, d) X-ray EDS mapping of zinc and oxygen, respectively e) SEM image of the Fructose ZnO; f) SEM backscattered electron image of the ZnO NPs; g, h) X-ray EDS mapping of zinc and oxygen, respectively i) SEM image of the Dextrin ZnO; b) SEM backscattered electron images of the ZnO NPs; c, d)X-ray EDS mapping of zinc and oxygen, respectively m) SEM image of the Starch ZnO; n) SEM backscattered electron images of the ZnO NPs; o, p)X-ray EDS mapping of zinc and oxygen, respectively q) SEM image of the ZnO Control; r) SEM backscattered electron images of the ZnO NPs; s, t)X-ray EDS mapping of zinc and oxygen, respectively.	51
Figure 3.3: EDX spectra showing the elemental composition of a) Glucose-ZnO, b) Fructose-ZnO, c) Dextrin-ZnO, d) Starch-ZnO, and e) ZnO Control, f) weight percent of Zn and O in each ZnO NPs obtained from SEM-EDX elemental analysis.	52
Figure 3.4: UV-visible absorption spectrum of ZnO NPs suspension in ethanol.	53
Figure 3.5: XRPD patterns of the ZnO NPs.	54

Figure 3.6: a) XPS survey spectrum of Glucose ZnO, b) XPS spectrum of Zn 2p, c) XPS spectrum of O 1s; d) XPS survey spectrum of Fructose ZnO, e) XPS spectrum of Zn 2p, f) XPS spectrum of O 1s; g) XPS survey spectrum of Dextrin ZnO, h) XPS spectrum of Zn 2p, i) XPS spectrum of O 1s; j) XPS survey spectrum of Starch ZnO, k) XPS spectrum of Zn 2p, l) XPS spectrum of O 1s.	56
Figure 3.7: a) UV-vis spectra of MO (5 ppm) solution in DIW by Fructose-ZnO, b) percent degradation of MO with time by ZnO NPs, c) Pseudo-first order kinetics reaction of MO degradation, and d) A digital photograph of degradation of MO solution during photocatalysis by Fructose-ZnO.	58
Figure 3.8: a) UV-vis spectra of the 5 ppm MO solution with time by Fructose-ZnO in simulated FDW, b) percent degradation of MO with time by different ZnO NPs derived from saccharides, and c) Pseudo-first order kinetics of the MO degradation reaction.	60
Figure 3.9: a) percent degradation of MO with time by different ZnO NPs derived from saccharides, and b) Pseudo-first order kinetics of the MO degradation reaction.	61
Figure 3.10: a) Reaction of terephthalate with the photo catalytically generated •OH radical to form 2-hydroxy terephthalate, b) time-dependent fluorescence emission spectra of 2-hydroxy terephthalate solution without ZnO NPs, c) fluorescence emission spectra of 2-hydroxy terephthalate solution photocatalyzed by Dextrin-ZnO with respect to time, and d) fluorescence emission intensity at 425 nm versus time graph for different ZnO NPs.....	64
Figure 3.11. Cyclic stability of the ZnO NPs of MO degradation for 3 cycles.	66
The photocatalytic activity of ZnO NPs over the course of 3 cycles illustrates Figure 12. The results demonstrate that the ZnO NPs exhibited reliable performance throughout the study. In each cycle, more than 95% of MO was degraded by the ZnO NPs. Based on these findings, it can be inferred that the ZnO NPs synthesized in this study have the potential to serve as a durable and effective photocatalyst for the degradation of organic pollutants in wastewater.	66
Figure 4.1: a) Typical SEM image of ZnO@600 °C, b) EDX spectra of ZnO showing the elemental composition, c) SEM backscattered electron image of ZnO d) X-ray EDS mapping image of zinc, e) X-ray EDS mapping image of oxygen.....	75
Figure 4.2: TEM image of ZnO@800 °C.	76
Figure 4.3: XRD of the ZnO NPs	77
Figure 4.4: (a) XPS survey spectrum of the ZnO NPs, b) XPS spectrum of the Zn 2p, (c) XPS spectrum of the O 1s.	79
Figure 4.5: Time-dependent percent degradation of MO by ZnO prepared by the modified method compared with the hotplate method.	81
Figure 4.6: UV-vis spectra of MO (5 ppm) solution in DIW by ZnO @ 600 b) percent degradation of MO with time by ZnO NPs, c) Pseudo-first order kinetics reaction of MO degradation.....	82
Figure 4.7: a) UV-vis spectra of the 5 ppm MO solution with time in DWI during the photocatalysis by Fructose ZnO-coated clay pot, b) percent degradation of MO with time by and ZnO@600C coated clay pot.....	85
Figure 4.8: a) UV-vis spectra of the 5 ppm MO solution with time in DWI during the photocatalysis by Fructose ZnO-coated clay pot, b) percent degradation of MO with time by and ZnO@600C coated clay pot, c) digital photograph representing the decolorization of 5 ppm MO solution after photocatalysis by Fructose ZnO.	87
Figure 5.1: a) Typical SEM image of ZnO@C-2 b) EDX spectra of ZnO@C-2 showing the elemental composition, c) SEM backscattered electron image of ZnO@C-2 d) X-ray EDS	

mapping image of zinc, e) X-ray EDS mapping image of oxygen, and f) X-ray EDS mapping image of carbon.....	96
Figure 5.2: a) and c) are the dark field image, b) and d) are the bright field image at two different sites of ZnO@C-2, respectively.....	98
Figure 5.3: XRD pattern of ZnO@C nanocomposite.	99
Figure 5.4: XPS High-resolution spectra for core levels of: a) XPS survey of 2gZnOC. b)C 1s,c) Zn 2p, d) O1s and e)N1s, along with deconvolution peaks.....	101
Figure 5.5: Adsorption capacity of ZnO@C-2 composite for MO, MB, CR, and BPA at different initial concentrations.	103
Figure 5.6: The linear form of the a) Langmuir and b) Freundlich adsorption isotherms for the adsorption of MO, MB, CR and BPA by ZnO@C-2 composite, respectively.	105
Figure 5.7: a) Time-dependent percent adsorption of MO, MB, CR, and BPA by ZnO@C-2 composite, (Initial concentration = 50 ppm, V = 20 mL and adsorbent = 20 mg) and (b) the corresponding pseudo-second-order kinetics adsorption.....	107
5.8: Temperature-dependent a) adsorption capacity b) percent adsorption of BPA by ZnO@C-2 composite, (Initial concentration = 100 ppm, V = 20 mL and adsorbent = 10 mg).	108
Figure 5.9: Regeneration of ZnO@C-2 for the adsorption of MO dye.	109
Figure 5.10: a) The UV-vis spectra of the 5 ppm MO solution by ZnO@1were recorded at different time intervals during the photocatalytic degradation process, b) time-dependent percent degradation of MO by solution by ZnO@1, ZnO@2, and ZnO@4.	115

List of Illustrations

Scheme 2.1: Sawdust-mediated synthesis of ZnO nanoparticles and chemical reaction involved in the synthesis.	21
Scheme 2.2: Proposed scheme for the photocatalytic generation of ROS by the ZnO nanoparticles followed by the degradation of organic pollutants.	38
Scheme 3.1: Saccharides (glucose on the scheme above) mediated combustion synthesis of ZnO NPs.....	49
Scheme 3.2. Proposed mechanism for generating hydroxyl radicals ($\bullet\text{OH}$) and organic pollutants degradation by ZnO NPs.....	65
Scheme 4.1: Preparation of ZnO NPs by the modified method.....	72
Scheme 4.2: Preparation of ZnO-coated clay pot by a dip coating method.	86
Scheme 5.1: Chemical reactions and pictorial scheme showing the steps involved in the preparation of ZnO@C nanocomposites.....	93

Chapter 1: Multifunctional Nano Materials for Sustainable Water Treatment Processes

1.1. Introduction

Water is a simple triatomic polar molecule, and it is made up of two hydrogen (H) atoms and one oxygen (O) atom¹. The three atoms of water molecule make an H-O-H angle, the bond angle between two hydrogen atoms is approximately 105° and the O-H bond length is 95.84 picometres². A single water droplet contains billions of water molecules³. Figure 1.1 shows the chemical structure of a water molecule.

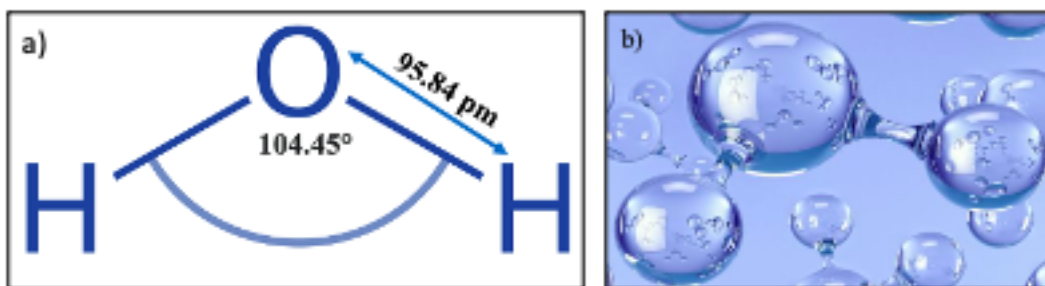


Figure 1.1: a) 2d chemical structure or skeletal formula of water molecule showing bond angle and bond length, b) 3d image of a water molecule.

Water is an essential resource for sustaining life on Earth⁴. It comes as no surprise that all living organisms depend on water for their existence^{5,6}. It plays a significant role in the various aspects of human life and in the global economy. Clean water is crucial for promoting and maintaining good health. Access to clean water helps to prevent waterborne diseases and improves overall welfare and it serves as a valuable resource that impacts numerous aspects of our everyday lives⁷. In our households, we rely on water for a multitude of purposes such as cooking, cleaning, bathing, and sanitation^{8,9}. Moreover, water is integral to the production processes of our daily use items, including food, clothing, vehicles, electronic devices, books, and so on. Additionally, it is involved in constructing our homes, schools, and roads¹⁰. It is estimated that about 70% of

freshwater resources are utilized for agricultural purposes¹¹. Approximately 6.5% of the global protein consumption comes from fishing, whether in freshwater or saltwater environments¹². Water is important for economic development as well such as industries, manufacturing, and energy production including powering plants, and to generate electricity, and so on¹². Water ecosystem and diversity provides a food source and habitat for countless living organism, and it is a key element in maintaining ecological balance¹³. Overall, water is an essential and fundamental resource that is vital for sustainable economic development, poverty alleviation, and the overall welfare of societies. The availability and management of water resources are of utmost importance to ensure the continuation of economic progress and enhance the well-being of communities¹⁴.

1.2. Water Contamination

Around 71% of the Earth's surface is enveloped by water, including oceans, seas, lakes, rivers, and various water bodies. While water may seem abundant to us, approximately 97.5% of total water is saline water found in oceans and seas, and only a small fraction of it, around 2.5%, of the Earth's water is considered fresh water. Unfortunately, more than two-thirds of this freshwater is trapped in glaciers and polar ice caps, making it not accessible for immediate use¹⁵. Although water covers a substantial portion of the Earth's surface, the availability of accessible freshwater resources is relatively limited. This limited amount of fresh water is essential for sustaining our life, agricultural purposes, supporting various industries, and other applications¹⁶. The depletion of this limited number of freshwater resources has become increasingly concerning because of rapid population expansion and the development of industrialization. Insufficient wastewater treatment infrastructure and the unregulated discharge of untreated wastewater into the environment have led to a significant rise in freshwater pollution. This has contributed to the

contamination of freshwater resources at an alarming rate. Figure 1.2. is showing the world's water distribution image.

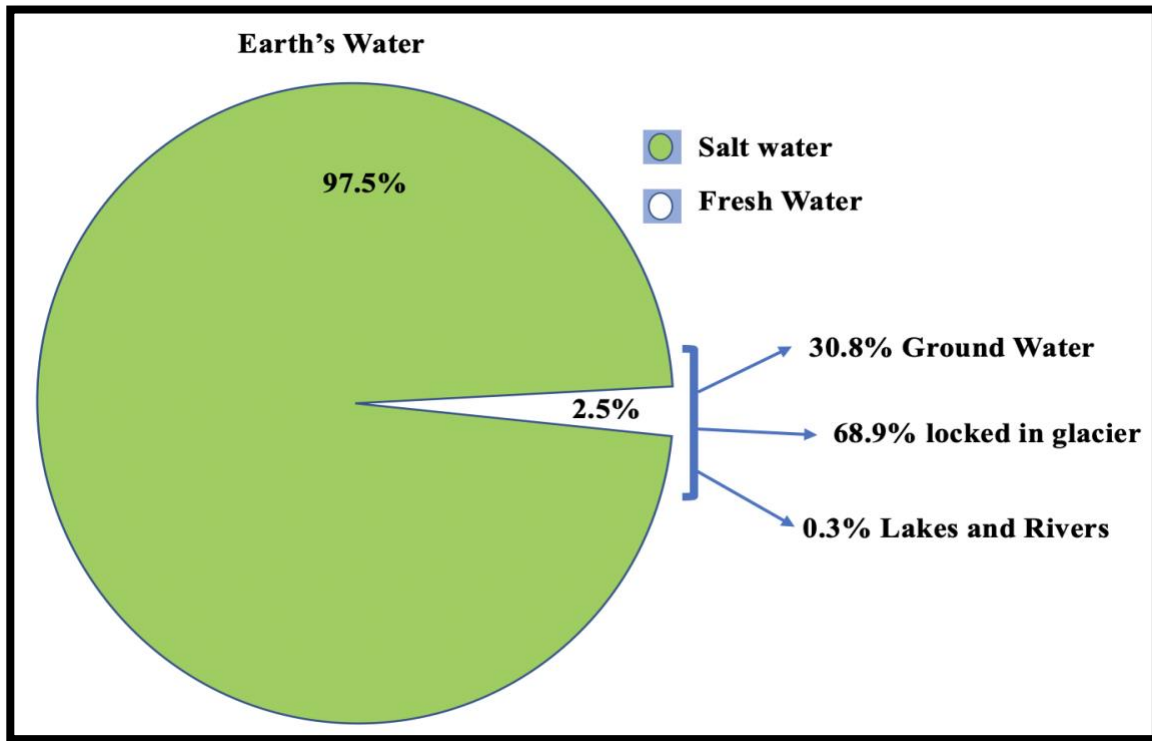


Figure 1.2: Earth's Water Distribution.

Water can be contaminated by a wide range of pollutants originating from diverse sources in the environment. Unfortunately, in the past two centuries, water has become the ultimate destination for pollutants released into the environment, thereby water contamination is increasing day by day¹⁷. Broadly, water contaminants can be divided into biological, inorganic, and organic categories¹⁸. The biological contaminants are bacteria, viruses, and protozoan cysts. Although these contaminants are too small to see by the naked eye, they can cause of serious health problems. Inorganic contaminants are elements and chemicals that do not contain carbon¹⁹. The hardness of water is the consequence of naturally occurring inorganic contaminants which are measured by the amount of magnesium and calcium present in the water²⁰. In addition to hardness, various inorganic substances like arsenic, fluoride, copper, lead, chromium, antimony, mercury, and

cyanide can contaminate water²¹. They can be found in water from natural sources, industrial processes, and plumbing systems. While all inorganic contaminants do not occur naturally, some of them are produced because of man-made pollution. For example, nitrate can be generated through the oxidation of ammonia present in fertilizers²². Wastewater from industrial processes is a common source of very toxic heavy metal contamination²¹. Once these contaminants accumulate in the water, they can persist and pose serious risks to human health if consumed in high concentrations and have toxic effects on aquatic organisms, as well as on the environment. Interestingly, small amounts of some of the inorganic substances are beneficial for human health, but larger quantities can be extremely harmful so, obtaining the right balance is crucial²³. For instance, a specific amount of fluoride is beneficial for dental health whereas excessive exposure can cause tooth discoloration²⁴⁻²⁶. Organic contaminants consist of carbon and hydrogen and are commonly associated with issues such as odor, taste, and discoloration in groundwater²⁶. They can be artificially introduced into the environment or originate naturally through the decomposition of vegetation. If organic contaminants persist and accumulate in the water, and it is consumed or used for various purposes it possesses serious risks to aquatic life as well as potentially impact human health. Industrial and agricultural activities can contaminate water bodies. Improper discharge of chemicals, heavy metals, fertilizers, and pesticides into the water bodies through runoff, can lead to water contamination²⁷⁻²⁹. Untreated sewage and wastewater disposal into the water is another source of contaminants as it can introduce chemicals, pathogens, and other pollutants into the water. Rainwater drainage from agricultural fields, urban areas, and industrial sites can transport pollutants, including sediments into nearby water sources. Natural sources such as mineral deposits, and volcanic activity can occur water pollution as well³⁰. Figure 1.3 is showing the sources of pollutants which accumulate and pollute water. The effective elimination of these

contaminants from water is essential to maintain water sources, protect human health, preserve ecosystems, and encourage sustainable water usage. Hence, this is essentially required to develop an effective, secure, cost-effective, and easily accessible method for the water treatment processes³¹. The existing water treatment methods have remained unchanged for more than a century and demand extensive infrastructure due to their limited efficiency and large-scale operational requirements. Therefore, there is a need to innovate and improve upon these methods to enhance their efficiency and enable more widespread implementation³².



Figure 1.3: Sources of pollutants in water.

1.3. Water Treatment Processes

Wastewater treatment methods play a vital role in removing contaminants and pollutants for the management of a safe and sustainable environment^{33,34}. There are numerous methods applied for the treatment of water that is contaminated with organic pollutants such as physical treatment methods which includes adsorption, filtration, coagulation, or flocculation^{35,36}. Chemical methods include an advanced oxidation process^{37,38}. Oxidation techniques used for water treatment include photocatalytic degradation, electrochemical oxidation, and ozonation³⁹. Biological treatment methods utilize living organisms, such as microorganisms, to break down and eliminate pollutants from wastewater⁴⁰. Figure 1.4 is the visual representation of different water treatment methods.

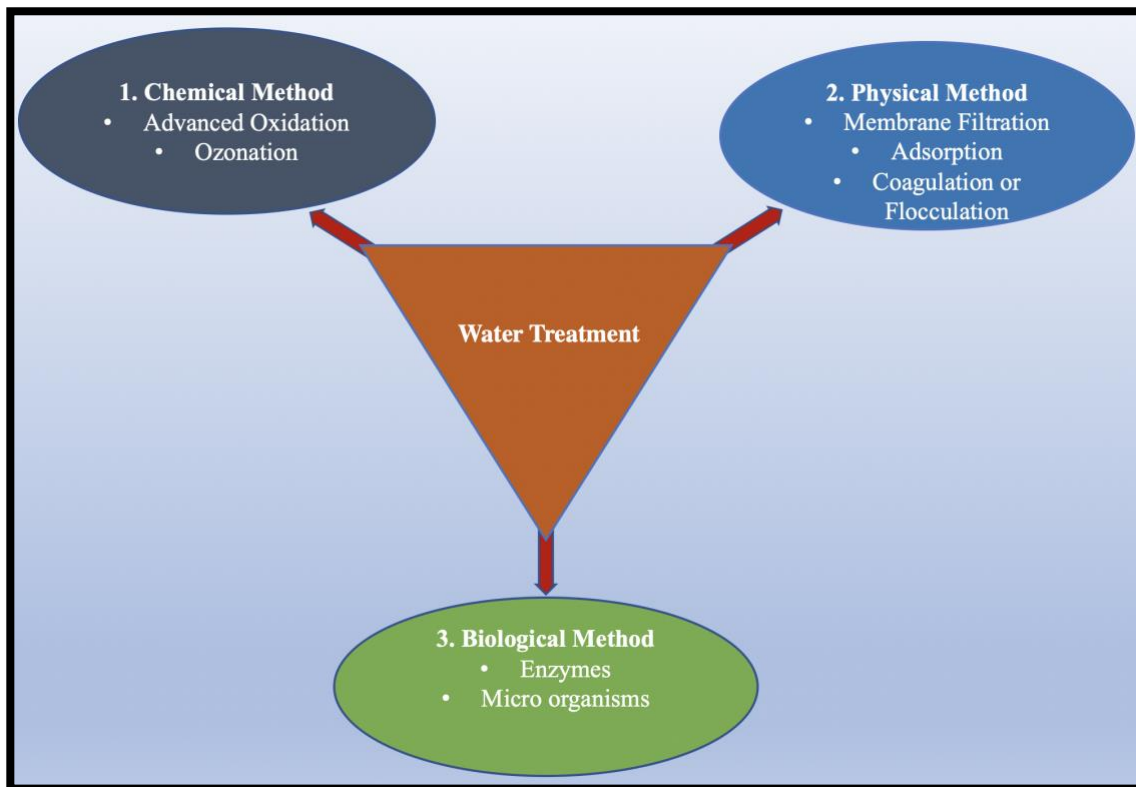


Figure 1.4: Wastewater treatment methods.

Among these methods, photocatalytic degradation and adsorption are preferred approaches for water remediation processes due to their ease of use and cost-effectiveness, and eco-friendly nature^{32,33}. Figure 1.5 represents the pollutants removal approaches by photocatalysis and adsorption. Photocatalytic degradation is an environmentally friendly and sustainable method since it does not require any other additional reagents or chemicals to degrade the organic pollutants in water³³. When a photocatalyst is exposed to pollutants in the presence of UV light, it causes the electrons within the material to become energized and move to higher energy levels. These energized electrons can then engage in chemical reactions with nearby molecules, including organic and inorganic pollutants found in water⁴¹. Moreover, photocatalysis can be utilized for the treatment of water which are contaminated with toxic and persistent pollutants, and which is challenging to treat by conventional methods. Finally, the key advantage of this method is the ability to completely degrade and mineralize the organic pollutants, converting them into simpler and non-toxic compounds. In summary, this process significantly offers the benefits of degrading pollutants effectively and ensures the elimination of harmful substances from the water source³³. Some persistent pollutants include heavy metals (such as mercury, lead, and cadmium) present in wastewater which is challenging to degrade by catalysis that can be removed by adsorbents. Adsorbents have a high surface area with active site and selectively adsorb pollutants on its surface thereby removing these pollutants from water, resulting in clean water for various applications⁴². Moreover, adsorption studies can optimize experimental conditions and parameters for the treatment of water. By investigating the variables such as adsorbent dosage, pH, temperature, and time researchers can precisely identify the optimal conditions to achieve maximum adsorption efficiency or capacity in the study⁴³. Overall, by developing the adsorbent materials and optimizing the treatment processes, the adsorption study will not only allow valuable

insight into the potential water treatment methods but also it will contribute to obtaining the ultimate provision of safe and clean water^{44,45}.

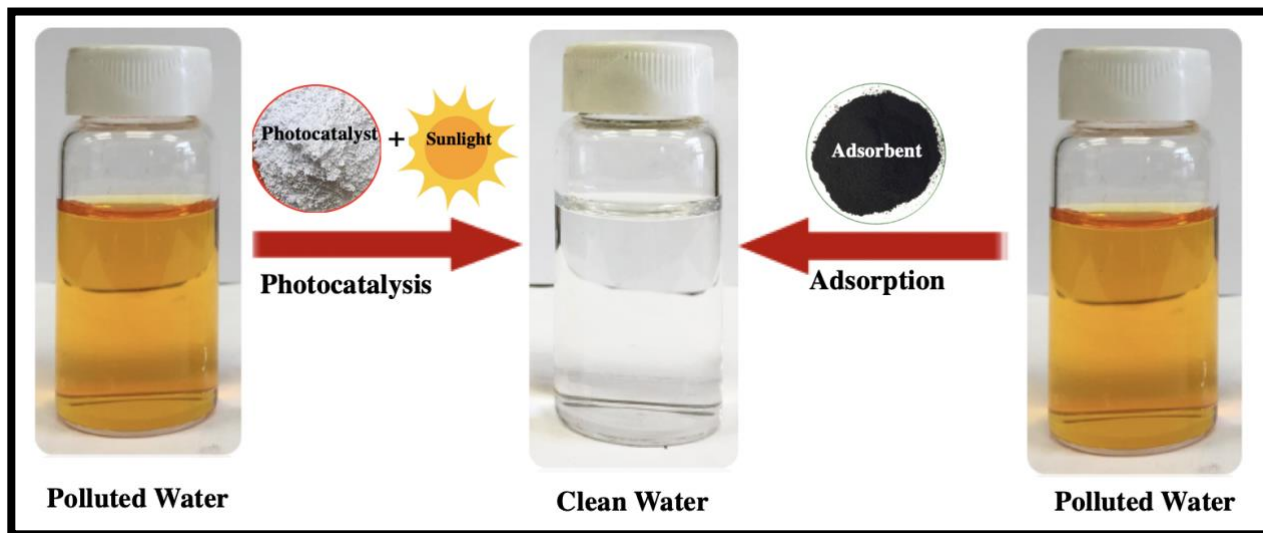


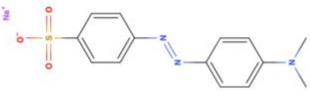
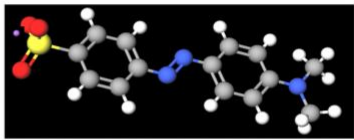
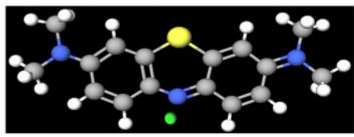
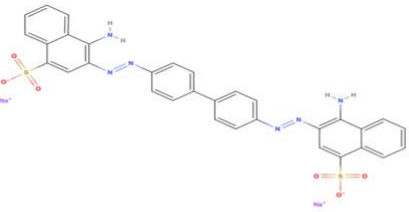
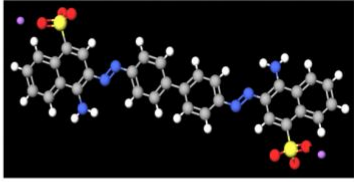
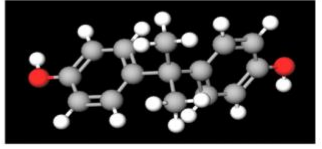
Figure 1.5: Photocatalytic degradation and adsorption for treatment processes.

In this report, utilizing advanced functional nanomaterials and incorporating nanotechnology could open new possibilities in addressing the challenges posed by organic contaminants in water. Nanomaterials offer various processes such as chemical, electrocatalytic, photocatalytic, adsorptive, and advanced oxidation for the effective and targeted removal of pollutants from water. These processes offer the advantage of efficient degradation of contaminants without generating any other additional pollutants. The advancement of catalytic nanoparticles holds the potential to revolutionize water decontamination, allowing the expansion of portable water treatment systems that can be beneficial for resource-limited rural areas worldwide.

This dissertation introduces facile and innovative methods for synthesizing functional nanomaterials, specifically, metal oxide nanoparticles, and nanocomposites, and explores their applications in photocatalytic, and adsorptive water treatment processes. Finally, extensive

research has been conducted to thoroughly examine these methods for the removal or degradation of organic pollutants including Methyl Orange (MO), Methylene Blue (MB), Congo Red (CR), and Bisphenol A (BPA) from water. The chemical structures of the MO, MB, CR, and BPA are given in Table 1.1.

Table 1.1: Structure of targeted pollutants.

Target pollutants	2D Chemical Structure	3D Chemical Structure
Methyl Orange (MO)		
Methylene Blue (MB)		
Congo Red (CR)		
Bisphenol A (BPA)		

1.4. Objectives and Contributions

The objective of this dissertation is to develop experimental methodologies for synthesizing nanomaterials for the application of sustainable water treatment processes. Herein, a highly active photocatalyst, Zinc Oxide (ZnO) nanoparticles, and a carbon-based adsorbent, Zinc Oxide and Carbon nanocomposite (ZnO@C) were successfully synthesized using a facile combustion method. ZnO nanoparticles and ZnO@C were utilized for the effective degradation and removal of organic pollutants in water, respectively. overall, this report provides a valuable

resource for obtaining the current state of research in sustainable water treatment. The research projects that have been added to this report are briefly given below.

A sustainable and reproducible method for the preparation of zinc oxide nanoparticles (ZnO) using sawdust and their application in photocatalytic degradation of organic pollutants (MO) is reported in Chapter 2. Sawdust has been utilized as a sacrificial template for the synthesis of porous morphology of ZnO. The average size of the ZnO nanoparticles size was found to be about 23 nm. It was found that ZnO nanoparticles were almost equally active in deionized water (DIW) and simulated fresh Drinking water (FDW) and almost complete decolorization of MO solution was achieved after 42 min of UV light irradiation. Additionally, the reproducibility of the synthesis method and the cyclic stability of the as-prepared ZnO were thoroughly studied. Moreover, the reproducibility of the synthesis methodology and the cyclic stability of the as-prepared ZnO nanoparticles were thoroughly studied, and found that nanoparticles are fairly active throughout the cycles over the 5 cycles of use. Finally, it was found that the ZnO nanoparticles, prepared in this study, leached less amount of zinc in water compared to the commercial ZnO; which indicated its better safety and sustainability regarding the photocatalytic water treatment.

A simple and fast method for the synthesis of ZnO using the aerobic combustion of saccharides such as glucose, fructose, dextrin, and starch for the degradation of organic pollutants is reported in Chapter 3. It was obtained that saccharide helped the formation of high surface area and high surface energy of ZnO nanoparticles with enhanced photocatalytic activity for pollutant degradation. The XPS results confirmed the high purity of the ZnO NPs. XRD measurements indicated the metastable states of the ZnO NPs resulting in excellent photocatalytic performance. The saccharide-derived ZnO NPs exhibited significant efficiency in eliminating MO dye from the

aqueous solutions under UV light as well as sunlight illumination. ZnO nanoparticles showed nearly equal MO degradation efficiency in DIW and simulated FDW matrices. A fluorescence test was performed to evaluate the photocatalytic hydroxyl radicals ($\bullet\text{OH}$) generation by the ZnO nanoparticles. Moreover, the stability of the ZnO NPs was obtained to assess their durability and long-term effectiveness by using the nanoparticles over multiple cycles in this chapter.

Method development for the synthesis of ZnO nanoparticles by modified synthesis method to improve photocatalytic performance for MO degradation under UV light and Sunlight is presented in Chapter 4. It was found that ZnO synthesized by the modified method showed enhanced MO degradation efficiency under UV light and sunlight than the ZnO synthesized in the previous report (chapter 3). SEM image revealed the highly porous structure resembling a powdery aggregate pattern. TEM image depicted the crystallinity of the synthesized product with bimodal size distribution. XRD pattern revealed the crystalline properties of ZnO nanoparticles, and it is characteristic of the hexagonal wurtzite crystal structure of the ZnO.

Chapter 5 reports a novel method for the synthesis of a regenerable adsorbent, Zinc Oxide, and Carbon Nanocomposite (ZnO@C) for the adsorptive removal of anionic and cationic organic pollutants (MO, MB, CR, BPA) from water. From the SEM image, it was found that the morphology of the zinc oxide and carbon nanocomposite is highly porous with a high surface area. This could be a reason for the high adsorptive capacity of the nanocomposite. The EDX spectra and the elemental mapping image of the zinc oxide and carbon nanocomposite have confirmed the presence of Zinc, oxygen, and Carbon. The TEM images were found, and they showed interconnected two-dimensional carbon nanosheets with embedded ZnO nanoparticles. The carbon nanosheets displayed a layered structure, while the ZnO nanoparticles appeared within the carbon matrix, confirming successful integration. The maximum adsorption capacity (Q_m) was determined

to be 385 mg/g, 286 mg/g, 244 mg/g, and 385 mg/g, for MO, MB, CR, and BPA, respectively. Finally, the adsorbent was regenerated and reused with only a slight decrease in its ability to adsorb. Our findings demonstrated that ZnO@C have great potential as effective adsorbents for efficiently eliminating MO, MB, CR, and BPA from water.

Chapter 2: Sustainable Synthesis of Zinc Oxide Nanoparticles for Photocatalytic Degradation of Organic Pollutants and Generation of Hydroxyl Radical

2.1. Introduction

The growing use of organic dyes in textile, cosmetics, pharmaceuticals, papermaking, and food industries has been causing serious environmental pollution, especially to water sources⁴⁶⁻⁴⁸. A major portion of these dyes (~10-20%) are discarded in the environment and most of these dyes exhibit varying degrees of toxicity, carcinogenicity, and mutagenicity to the living organisms^{49,50}. Additionally, these dyes are chemically and physically robust in nature and thereby can hardly be degraded by physical and chemical means such as light, heat, oxidizing agents, and biological agents⁵¹. A lot of these treatments use organic and inorganic chemicals, which cause secondary pollution in water by themselves and by their degradation products. Therefore, it is necessary to develop an efficient, sustainable, and chemical-free method for the removal or degradation of these dyes and other hazardous organic pollutants from water to make sure a sustainable society with access to clean water.

Among many other synthetic dyes, azo dyes such as methyl orange (MO) are reported to be used as a coloring agent in the pharmaceutical, food, brewing, cosmetic, textile, and leather industries. As an azo dye MO is toxic, mutagenic, carcinogenic, and resistant to biodegradation⁵². The release of MO from various industries into water bodies causes both short- and long-term effects on the environment, living organisms, and especially, human health⁵³. Special methods such as reverse osmosis, membrane filtration, coagulation, ion exchange, catalytic reduction, oxidation, complexometric methods, and aerobic and anaerobic biological methods are required for the degradation or removal of such recalcitrant pollutants⁵⁴. Recently, advanced oxidation processes (AOP) has emerged as an efficient method for the degradation of organic pollutants from

water⁵⁵. Because the AOP degrades the hazardous pollutants at an extremely faster rate, it is advantageous and more favorable over other methods such as adsorption, filtrations, precipitation, coagulation, biological treatment, and so forth⁵⁶⁻⁵⁸. Among AOP, the photocatalytic processes are of prime interest because of the requirement of no chemicals, generation of no secondary pollutants, and environmental sustainability⁵⁹⁻⁶¹. In photocatalytic processes, semiconductor-type metal oxides such as ZnO and TiO₂ are used as photocatalysts, which can degrade organic pollutants through the generation of reactive oxygen species such as hydroxyl radicals⁶²⁻⁶⁴. The strong oxidizing nature of these radicals can degrade the organic pollutants to CO₂ and H₂O, which is also known as the mineralization organics. In addition to the reactive oxygen species, photocatalysts have the ability to oxidize and/or reduce organic pollutants on their surface by redox reactions, which eventually cause the degradation of the pollutants⁶⁵⁻⁶⁷.

Among various photocatalysts, ZnO nanoparticles are one of the extensively studied semiconductor-type metal oxides with a band gap of ~ 3.37 eV. It is known to be one of the best photocatalysts for the degradation of environmental contaminants due to its high photocatalytic activity, relatively low cost, absence of toxicity, and excellent chemical stability under various conditions⁶⁸. In addition to the photocatalytic water treatment, ZnO nanoparticles are used in a number of applications in many fields, such as in solar cells, sensors, photoelectrochemical cells, antibacterial activity, and photocatalysis⁶⁹⁻⁷¹. For all of the above-mentioned applications, nanoscopic ZnO is of best-suited in contrast to the bulk or macroscopic ZnO⁷². These ZnO nanoparticles not only provide a high surface area but also offers a suitable bandgap for the separation of the exciton and thereby provide a feasible environment for enhanced photocatalytic activity⁷³. Therefore, different methods have been reported for the synthesis of ZnO nanoparticles with a wide range of morphologies (nanowires, nanorods, nanobelts, nanotubes, and whiskers)

using techniques such as ball-milling, combustion synthesis, sol-gel process, hydrothermal, spray pyrolysis, chemical vapor deposition, etc⁷⁴⁻⁷⁶. Most of these methods require sophisticated techniques, instrumentation, expensive chemicals, and prolonged reaction time^{65,77,78}. Therefore, there is a need for the development of a facile and environmentally friendly method for the synthesis of ZnO nanoparticles (1-100 nm in size) that are highly active for photocatalytic and many other applications.

In this study, we report a facile, inexpensive, reproducible, and sustainable method for the preparation of ZnO nanoparticles by burning a mixture of finely-ground sawdust and zinc nitrate hexahydrate salt. Sawdust has been utilized as a sacrificial template because it is renewable, readily available, cheap, and non-edible biomass. The porous sawdust was impregnated with zinc nitrate salt and this impregnated sawdust was combusted at 600 °C under the flow of air to obtain the ZnO nanoparticles. The porous morphology of the sawdust assisted and templated the formation of the ZnO nanoparticles with the control in their size and shape. Sawdust further assisted in the formation of ZnO in the nanoscopic size range (1-100 nm) by preventing their growth to the macroscopic size range. Four different ZnO nanoparticle samples [ZnO-n, where n = 1-4] were prepared by varying the mass ratio of sawdust and zinc nitrate salt to obtain the best-performing ZnO nanoparticles. The ZnO-n nanoparticles were used as the photocatalyst for the degradation of methyl orange (MO) under UV-B light irradiation into two different water matrices such as deionized and simulated fresh drinking water. A fast degradation of the MO was observed with a degradation of ~ 95% within 42 min of UV light irradiation. The ZnO-2 and ZnO-4 nanoparticles mediated degradation of MO was found to be 24 and 27 times faster compared to the ZnO-control under UV-B light irradiation. Additionally, the photocatalytic generation of hydroxyl radicals ($\bullet\text{OH}$) on the ZnO nanoparticle's surface was studied by the terephthalic acid fluorescence tests.

Finally, the reproducibility of the ZnO nanoparticles synthesis method was confirmed by triplicating the experiments. There are three important significances of this report from the synthesis and application point of view. Firstly, the synthesis procedure is novel, inexpensive, sustainable, and reproducible that can be adapted for the preparation of a wide variety of metal and mixed metal oxide nanoparticles just by using different metal nitrate salt as the precursor. Secondly, the ZnO nanoparticles demonstrate an excellent photocatalytic ability to degrade organic pollutants and generate hydroxyl radicals in water by UV light irradiation. Finally, yet importantly, it was found that the ZnO nanoparticles, prepared in this study, leached less amount of zinc in water compared to the commercial ZnO; which indicated its better safety and sustainability in regard to the photocatalytic water treatment.

2.2 Materials and Methods

2.2.1 Materials

Zinc nitrate hexahydrate [$\text{Zn}(\text{NO}_3)_2 \cdot 6\text{H}_2\text{O} \geq 98\%$], terephthalic acid [$\text{C}_8\text{H}_6\text{O}_4 = 98\%$], and sodium hydroxide ($\text{NaOH} \geq 98\%$) were purchased from Sigma Aldrich. Methyl Orange ($\text{C}_{14}\text{H}_{15}\text{N}_3\text{O}_3\text{S} >98.0\%$) and sawdust were obtained from TCI AMERICA and local shop, respectively. Sodium bicarbonate (NaHCO_3), calcium chloride dihydrate ($\text{CaCl}_2 \cdot 2\text{H}_2\text{O}$), magnesium sulfate heptahydrate ($\text{MgSO}_4 \cdot 7\text{H}_2\text{O}$), sodium nitrate (NaNO_3) and sodium silicate nonahydrate ($\text{Na}_2\text{SiO}_3 \cdot 9\text{H}_2\text{O}$), sodium fluoride (NaF), and sodium phosphate hydrate ($\text{NaH}_2\text{PO}_4 \cdot \text{H}_2\text{O}$) of analytical grades were purchased from Alfa Aesar and Sigma Aldrich. UVP Ultraviolet Crosslinker (Model CL-1000), equipped with UV-B fluorescent tube lamps, was used for the photocatalytic degradation of MO and the generation of hydroxyl radicals. Light Meter LX1330B was used to measure the intensity of light in the UV box reactor. The UV lamps generated ~ 302 nm wavelength of light, as per the vendor specification and the light intensity on

the reaction surface was measured to be ~21,500 lux. Syringe filters (PTFE) with 0.45 μ m pore size were purchased from VWR and utilized to filter the reaction mixture for the UV-visible spectroscopic analysis. Milli-Q water having resistivity >18.20 M Ω .cm, obtained from the Milli-Q water filter system, was used as a source of deionized water. The simulated fresh drinking water (FDW) was prepared by dissolving 147 mg /L CaCl₂.2H₂O, 252 mg /L NaHCO₃, 124 mg /L MgSO₄.7H₂O, 95 mg/L Na₂SiO₃.9H₂O, 2.2 mg /L, NaF, 12 mg /L NaNO₃, and 0.18 mg /L NaH₂PO₄.H₂O in Milli-Q water.

2.2.2. Characterization Techniques

UV-Visible spectroscopic analysis was performed on Agilent Cary 50 Conc UV-Visible Spectrophotometer. Standard quartz cuvette (10 mm path length) was used as the sample holder and the measurements were in the ranges of 200–800 nm with an accuracy of 1 nm. Transmission electron microscopy (TEM) images were obtained by using a Hitachi H-7650 Microscope with an acceleration voltage of 80 kV. Carbon filmed copper grid (200 mesh) was deposited with a suspension of ZnO nanoparticles (0.2 mg/mL) in water and air-dried before imaging. For scanning Electron Microscopy (SEM) images and Energy Dispersive X-ray (EDX) experiments, a JEOL JSM-IT100 microscope was used. For SEM and EDX analysis, carbon tape was used as the sample holder and the acceleration voltage of 10 and 30 kV were used for the SEM image and EDX analyses, respectively. Bruker D8 Discover X-ray diffractometer equipped with Cu K α radiation was used to obtain the X-ray diffraction (XRD) pattern of the ZnO nanoparticles. Copper K-alpha X-ray emission having a wavelength of 1.5406 Å was used and the measurements were in the range of 20-80 degrees with a scan rate of 4 degrees per minute. Elemental analysis (zinc and calcium) of the synthesized nanoparticles was performed using a PerkinElmer Optima 4300 DV ICP-OES. Nanoparticles were weighed, added to 50 mL conical plastic centrifuge tubes, and

dissolved using 4 mL of concentrated nitric acid (Plasma Pure, SCP Science). After all, the nanoparticles were dissolved, the solutions were diluted with distilled water ($18.2 \text{ M}\Omega\cdot\text{cm}$) to a final volume of 40 mL. The samples were then analyzed via ICP-OES using a multi-elemental standard for calibration. Four replicates were analyzed for each sample and the results were averaged.

2.2.3 Synthesis of ZnO Nanoparticles

Four different ZnO nanoparticle samples [ZnO-n, where $n = 1-4$] were synthesized following the same experimental procedure. The only difference was the variation in the mass ratio of the zinc nitrate hexahydrate to sawdust. In all the synthesis the amount of sawdust was kept constant (4g) while the amount of $\text{Zn}(\text{NO}_3)_2\cdot 6\text{H}_2\text{O}$ was varied. In the synthesis where 2g $\text{Zn}(\text{NO}_3)_2\cdot 6\text{H}_2\text{O}$ was used, the ZnO nanoparticles were named ZnO-2. Likewise, the ZnO nanoparticles samples were named as ZnO-1, ZnO-2, and ZnO-4. As a representative, the synthesis of ZnO-2 is explained in detail. In a 250 ml glass beaker, 4g sawdust and 2g $\text{Zn}(\text{NO}_3)_2\cdot 6\text{H}_2\text{O}$ salt was mixed with 25 ml deionized water. Then the mixture was honk sonicated for 1 hr. to impregnate the pores of the sawdust with $\text{Zn}(\text{NO}_3)_2\cdot 6\text{H}_2\text{O}$. Afterward, the mixture was partially dried in an oven at 100°C for about 2 h. The partially dried/wet sawdust powder impregnated with $\text{Zn}(\text{NO}_3)_2\cdot 6\text{H}_2\text{O}$ was heated at 600°C for 2 h in a tube furnace under the continuous flow of air. A ceramic crucible was used as a sample holder. The heating rate of $5^\circ\text{C}/\text{min}$ was used and natural cooling was used to cool the furnace. It is important to note that the heating temperature of 600°C was chosen to make sure complete combustion of the sawdust. The resulting ZnO-2 nanoparticles were white in color and the amount of product obtained was about 700 mg, which was washed with DI water. For washing, 25 ml deionized water was added with 700 mg ZnO-2 in a glass vial and bath sonicated for 20 min. Then the mixture was filtered through gravity filtration and washed

with an additional 100 ml DI water. The ZnO-2 powder was dried under ambient conditions for 24 hrs. The final product was ~500 mg, which was saved in a glass vial for characterization as well as photocatalytic applications. The washing process was performed to remove any soluble salts present in the ZnO samples and it greatly improved the photocatalytic activity of the ZnO nanoparticles.

Following the same experimental procedure, a control ZnO sample (ZnO-control) was prepared, where sawdust was not used. In other words, the ZnO-control was prepared by heating 4 gm of pure Zn (NO₃)₂·6H₂O for 2 h at 600 °C in a tube furnace under the flow of air. The Photocatalytic activity of the sawdust-mediated ZnO was compared with the ZnO-control. Likewise, only sawdust was heated in the tube furnace at 600 °C in the presence of air to make sawdust oxides (SDO) as the 2nd control of this study.

2.2.4. Photodegradation Experiments

Photocatalytic degradation of MO was carried out in a glass beaker (Pyrex) with 250 mL of capacity and dimensions of diameter × height = 7 cm × 9 cm. Methyl orange solution having a concentration of 5 ppm (mg/L) was used for the photocatalytic experiments. In detail, 30 mg of the catalyst was homogeneously dispersed in 30 ml of 5 ppm MO solution by 15 min of bath sonication in the dark. The bath sonication facilitated the homogeneous dispersion of the ZnO-n and the establishment of adsorption-desorption equilibrium between the ZnO-n and MO. Afterward, the mixture was irradiated under the UV lamps in the box reactor while continuously stirring at about 300 rpm. At a regular interval of 7 min, ~1.2 mL sample (MO solution) was withdrawn and filtered through a syringe filter (0.26 μm PTFE filter) for UV-visible spectroscopic analysis. The characteristic absorption of MO at 464 nm was used for the calculation of percent degradation.

For the cyclic stability experiments, the ZnO-n used in the first cycle was recovered by the gravity settling and reused for the following cycles. In detail, the reaction mixture (30 mL MO solution and 30 mg ZnO-n) was allowed to settle down by gravity, the supernatant was carefully decanted, and the recovered ZnO-n was used in the same way for the subsequent cycles. The percent degradation of MO was calculated after 42 min of photocatalysis by taking a sample (MO solution) from the reaction mixture.

2.2.5 Terephthalic Acid Photoluminescence Test

The experimental procedure was similar to the photocatalytic MO degradation tests. In this case, instead of MO solution, 30 ml of 5×10^{-3} M sodium terephthalate solution was used. A stock solution of 5×10^{-3} M sodium terephthalate was prepared by the reaction of a required amount of terephthalic acid with a stoichiometric amount of NaOH in water. During the photocatalytic reaction, ~1 mL sample (sodium terephthalate solution) was taken and filtered through the syringe filter in every 7 min. The fluorescence spectroscopy of the samples (3X diluted) was carried out with an excitation wavelength of 315 nm and the fluorescence emission intensity of hydroxy terephthalate was measured at 425 nm.

2.3. Results and Discussions

Due to the great potential of semiconductor type metal oxide photocatalysts, there is a need for the development of a facile, low-cost, fast, and environmentally green method for the synthesis of highly active metal oxide nanoparticles. This study demonstrates an extremely simple and sustainable route for the synthesis of highly active zinc oxide nanoparticles. The zinc oxide nanoparticles were prepared by the combustion of a mixture of sawdust impregnated with zinc nitrate hexahydrate salt at 600 °C, Scheme 2.1. In this reaction sawdust worked as a porous sacrificial template for the origin of the ZnO nanoparticles. Chemically, sawdust acted as the fuel

and zinc nitrate hexahydrate acted as the oxidizing agent in the synthesis. We believe that the porous morphology of the sawdust mediated the formation and the size and shape of the ZnO-n.



Scheme 2.1: Sawdust-mediated synthesis of ZnO nanoparticles and chemical reaction involved in the synthesis.

There are several significances of the present method in terms of the synthesis and applications which include I) the simplicity in the experimental conditions and procedures, II) robustness and reproducibility of the experimental procedure, III) the utilization of sawdust as a cheap, readily available, renewable, and non-edible biomass, IV) the avoidance of expensive or hazardous materials/solvents, V) excellent photocatalytic activity of the as-prepared ZnO nanoparticles, and VI) less zinc leaching properties compared to commercial ZnO. Moreover, this method can potentially be adapted for the large-scale synthesis of a wide variety of other metal and metal oxide nanoparticles. For example, if cobalt or cerium nitrate salt is used instead of zinc nitrate, this method can generate cobalt or cerium oxide nanoparticles. Also, heating the sawdust-impregnated metal nitrate salts under an inert gas atmosphere can generate nanocomposites of carbon and metal oxides, which can be utilized for a number of applications.

In recent years, photocatalytic treatment has attracted extensive attention in wastewater treatment; especially, in the degradation of hazardous organic pollutants. The photocatalytic processes have received much attention due to their greener approach, chemical-free treatment, potential in the utilization of solar light, and applicability in resource-limited areas. Photocatalytic water treatment can be considered an effective approach to a sustainable water treatment technology. Due to rapid industrialization and improper disposal of waste materials, access to clean water is shrinking all over the world. Therefore, the development of an efficient and sustainable photocatalytic water treatment technology employing can not only provide access to clean water but also make sure sustainable economic development.

2.3.1. SEM images, EDX, and ICP-OES Elemental Analysis of ZnO Nanoparticles

Scanning electron microscopy (SEM) images were obtained to visualize the surface morphology, whereas the EDX spectra was taken to reveal the quantitative and qualitative elemental composition of the as synthesized ZnO nanoparticles. The SEM image of the ZnO-4 (as the representative) is shown in Figure 2.1a. From the SEM image, the ZnO-4 were seen to be aggregated with powder like morphology. The SEM image also revealed the sawdust-like porous morphology of the ZnO nanoparticles, which is assumed to be templated from the porous architecture of the wood tissue in the sawdust.

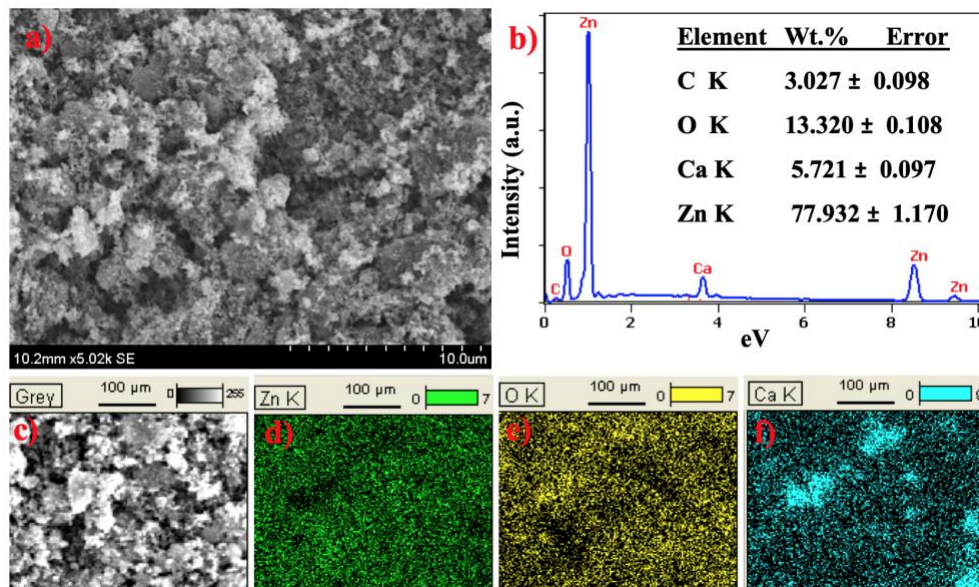


Figure 2.1: a) Typical SEM image of ZnO-4, b) EDX spectra of ZnO-4 showing the elemental composition, c) SEM backscattered electron image of ZnO-4, d) X-ray EDS mapping image of zinc, e) X-ray EDS mapping image of oxygen, and f) X-ray EDS mapping image of calcium.

Chemical composition of the ZnO-4 (as a representative) was studied by the EDS spectral and elemental mapping images, 1b-f. It was found that the ZnO-4 was composed of Zn (79.93 % wt.), O (13.31% wt.), Ca (5.72% wt.), and C (3.02 % wt.). The presence of Zn and O indicated the formation of zinc oxide; whereas the origin of Ca and O indicated the presence of calcium oxide in the ZnO-4 sample. The presence of calcium oxide in the ZnO-4 samples is assumed to be originated from the minerals present in the sawdust. The presence of calcium oxide was further identified and quantified by the ICP-OES and XRPD analysis, which is discussed in section 3.3. A weak carbon peak was also observed in the EDS spectrum, which may have originated from the carbon tape that was used as the substrate for SEM imaging.

The elemental (zinc and calcium) composition of ZnO-n nanoparticles was further quantified by the ICP-OES analysis. The results revealed that the ZnO-4 nanoparticles consisted of 67.28% zinc and 4.02% of calcium. The ratio of zinc to calcium was 16.76 ± 0.15 . The ZnO-2

nanoparticles were composed of 65.26% and 7.65% of calcium. The ratio of zinc to calcium was 8.54 ± 0.17 . The ZnO-1 nanoparticles were composed of 46.01% zinc and 10.55% of calcium. The ratio of zinc to calcium was 4.36 ± 0.06 . The SDO-control particles had trace levels of zinc of around 0.27% and 26.60% of calcium. The ratio of zinc to calcium was, on average, 0.01 ± 0.001 . Therefore, it was confirmed that the ratio of zinc to calcium in the ZnO-n nanoparticles increased with the increasing mass ratio of zinc nitrate to sawdust in the starting material and vice-versa.

2.3.2. XRPD Pattern of ZnO Nanoparticles

The X-ray powder diffraction (XRD) pattern provides crystalline properties such as atomic and molecular structure, lattice plane identification, and crystallite size of crystalline material. Thus, the crystalline properties of ZnO nanoparticles were studied by the XRPD pattern, Figure 2.2. Sharp diffraction peaks centered at $2\theta = 31.7^\circ, 34.4^\circ, 36.2^\circ, 47.5^\circ, 56.5^\circ, 62.8^\circ, 66.3^\circ, 67.9^\circ, 69.0^\circ, 72.6^\circ, \text{ and } 77.2^\circ$ are characteristic to (100), (002), (101), (102), (110), (103), (200), (112), (201), (004), and 202 lattice planes of crystalline hexagonal wurtzite ZnO (Zincite, JCPDS 5-0664), Figure 3b-e^{68,79}.

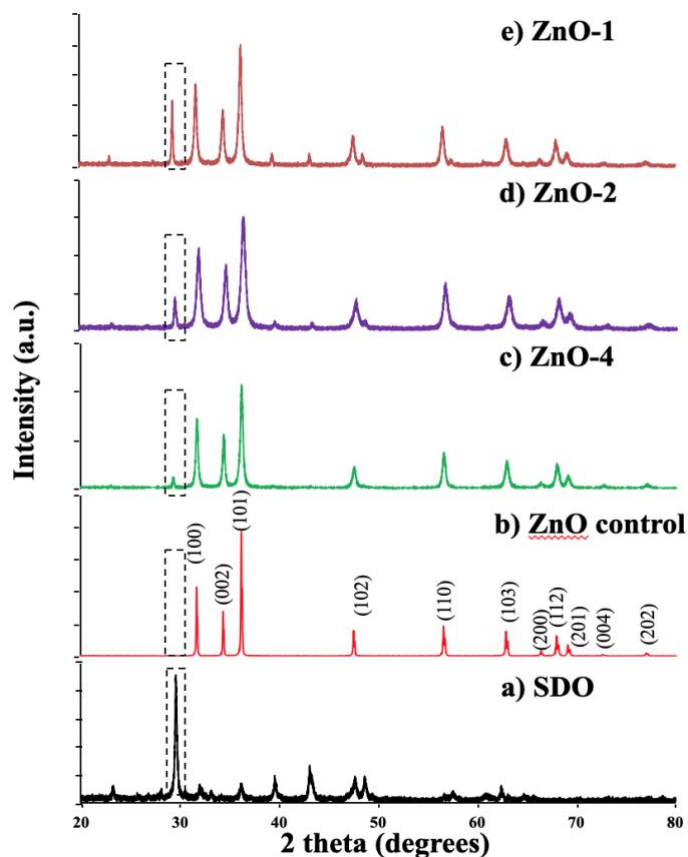


Figure 2.2: XRPD pattern of the ZnO-n (n=1-4), ZnO-control, and sawdust oxides (SDO) showing their crystallinity.

Employing the Debye–Scherrer’s formula (Equation 1) the average crystallite size of the ZnO nanoparticles was determined.

$$\text{Debye–Scherrer’s Equation, } d = k\lambda / \beta\cos\theta \quad (1)$$

where d is the crystallite size, λ is the wavelength of Cu $K\alpha$ X-ray radiation (1.54 Å), θ is the Bragg diffraction angle, k is the shape factor (0.9), and β is the full width at half-maximum of the most intense (101) diffraction peak. The average crystallite size of the ZnO-1, ZnO-2, and ZnO-4, and ZnO-control were calculated to be 27.3, 20.7, 26.7, and 75.5 nm respectively. It could be noted that the average crystallite size of the ZnO-4 is somewhat different from the particle size

measured from the TEM images. This is because the crystallite size is the size of the coherently diffracting domain, which may not be equal to the particle size measured from TEM images.

In addition, the XRD pattern of the ZnO-control and SDO was obtained to study the presence of impurities in the ZnO-n nanoparticles. The ZnO-control and ZDO were prepared by heating the zinc nitrate hexahydrate salt and sawdust separately in the tube furnace at 600 °C under an air atmosphere. The absence of any undesired peaks in the XRPD pattern of ZnO-control, shown in the dashed rectangle, indicates its high purity. The ZnO-control was highly pure because of the use of no sawdust in its synthesis. The XRPD pattern of the SDO indicated mostly the presence of calcium oxide, Figure 2a. It was found that the intensity of one of the calcium oxides peaks at 29°, shown in the dashed rectangle, gradually increased with the higher mass of sawdust used in the ZnO synthesis. For example, the ZnO-control (where no sawdust was used) did not show any calcium oxide peak, whereas the ZnO-1 through ZnO-4 showed the gradually lower intensity of the calcium carbonate peak (shown in the dashed rectangle), which is proportional to the amount of sawdust used. From this study, it was confirmed that the ZnO-n was composed of calcium oxide/others and the weight percentage of calcium oxide increased with the increase in the mass ratio of sawdust to zinc nitrate salt used in the synthesis. A similar trend was found in the ICP-OES elemental quantitative analysis and the EDS-elemental analysis, Figure 1b. The varying percentage of calcium oxide eventually adversely affected the catalytic performance, which is discussed in the photocatalytic performance section.

2.3.3. TEM images of ZnO Nanoparticles

The transmission Electron Microscopy (TEM) images of the ZnO-4 (as a representative) are shown in Figure 2.3a-b with two different magnifications. The TEM images confirmed the formation and morphology of ZnO nanoparticles. The TEM images showed that the ZnO-4 were

in a variety of shapes with faceted surfaces, which indicated high crystallinity of the ZnO-4, Figure 2.3b. Some shapes that could be identified from the TEM image were spherical, cubic, hexagonal, and pentagonal. It was also found that the ZnO-4 tended to aggregate, which could be attributed to the high surface area and surface energy of the ZnO-4.

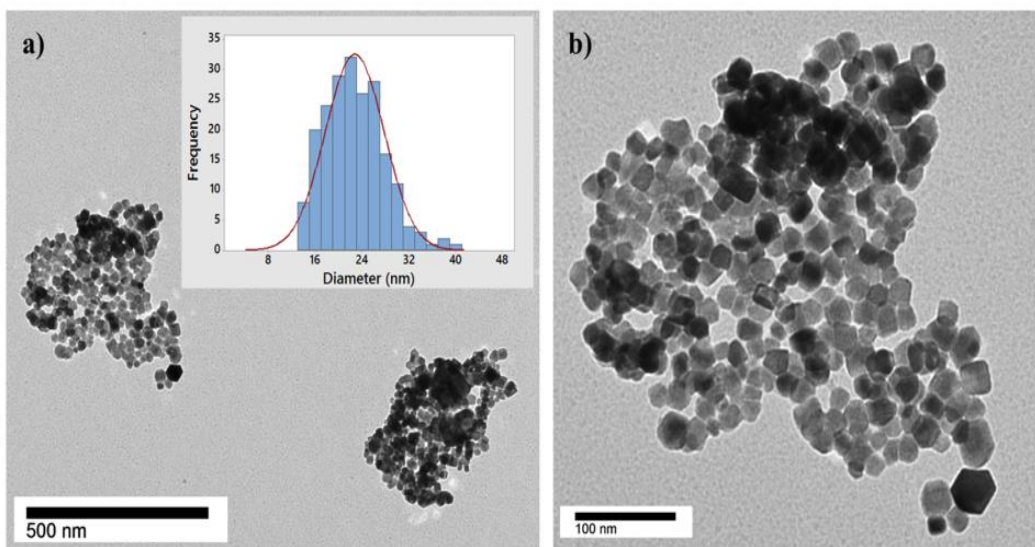


Figure 2.3: a-b) TEM images of ZnO-4 with two different magnifications. Inset: Size distribution of the ZnO-4 based on the TEM image 2b.

In Figure 2.3a (inset), the size distribution histogram of the ZnO-4 is shown. The size distribution was obtained by measuring the size of 200 randomly picked nanoparticles utilizing the ImageJ software. From the histogram, it was found that the ZnO-4 had an average size of about 23 nm. This also demonstrated that the size of the ZnO-4 was not monodispersed rather it ranged from about 14 to 40 nm.

2.3.4. UV-Visible Spectrum of ZnO Nanoparticles

Zinc oxide nanoparticles are known to have band gaps falling in the semiconductor region. Therefore, the UV-visible spectrum was performed to determine the band gap energy of the ZnO-*n* (*n*=1-4). For this, suspension of ZnO-*n* in ethanol (0.125 mg/mL) was used, and the UV-vis. spectrum is shown in Figure 2.4. The ZnO suspension generated a UV-vis absorption band

centered at 352, 354, and 366 nm for ZnO-1, ZnO-2, and ZnO-4, respectively. The absorption band at this region can be attributed to the excitation of electrons from the valence band to the conduction band ($O2p \rightarrow Zn3d$). For ZnO-4, the absorption band was sharper than ZnO-2, which was followed by ZnO-1. The widening and shifting of the absorption band from ZnO-4 to ZnO-1 could be attributed to the presence of a higher percentage of calcium oxides originating from sawdust. The gradual increase in the percentage weight of calcium oxides from ZnO-4 to ZnO-1 was found in the XRPD analysis. On the other hand, the SDO did not show any characteristic absorption band like zinc oxide nanoparticles, which indicated its absence of any specific band gap, Figure 2.4. Additionally, it was observed that the ZnO-n were highly absorptive in the UV region (<400 nm) of the electromagnetic spectrum in contrast to the visible region. This further explains why ZnO nanoparticles are a highly active photocatalyst under UV light irradiation in contrast to visible light.

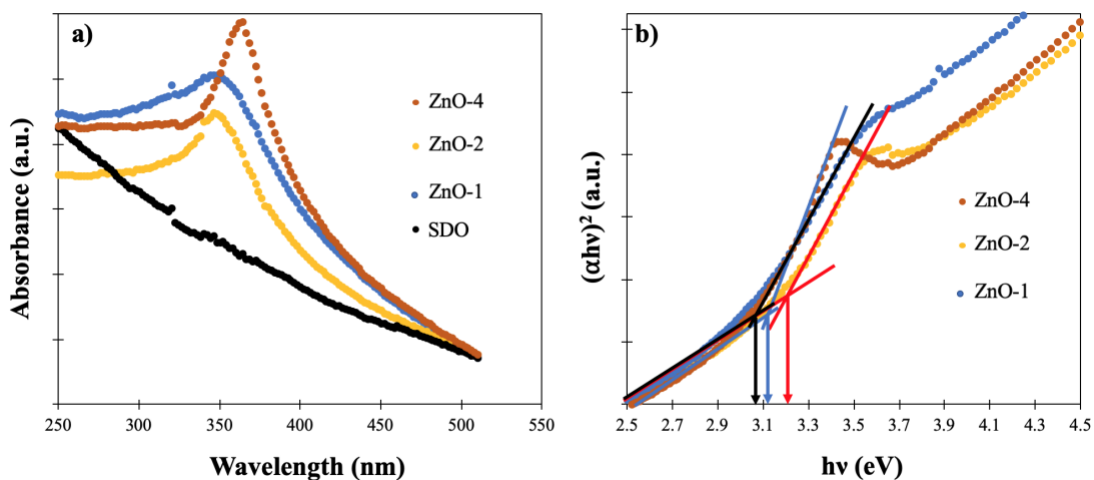


Figure 2.4: a) UV-visible absorption spectrum of ZnO-n and SDO suspension in ethanol and b) Tauc plot for the determination of bandgap of ZnO-n.

From the UV-visible absorption spectrum, the optical band gap of the ZnO-n was estimated utilizing the Tauc equation. The estimated band-gap energy of ZnO-1, ZnO-2, and ZnO-4 was calculated to be 3.15 eV, 3.21 eV, and 3.09 eV, respectively.

The results indicated that all the ZnO nanoparticles samples had band gaps that are lower than the band gap of bulk ZnO (3.37 eV). This reduction of the band gap may be attributed to the presence of defect levels within the band gap and due to the presence of valence band-donor atoms in the nanoparticles. We assume the presence of calcium and different other elements in the sawdust may have doped the ZnO to narrow down their band gap.

2.3.5. Photocatalytic Degradation of Methyl Orange

The photocatalytic degradation of MO in DIW and simulated FDW was studied using the ZnO-n under UV light irradiation. The percent degradation of MO was calculated using the following Equation.

$$\text{Percent MO degradation} = \frac{C_0 - C_t}{C_0} \times 100 \% = \frac{A_0 - A_t}{A_0} \times 100 \% \quad (2)$$

Where C_0 and C_t represent the concentrations of MO at the beginning and at time t of the photocatalytic reactions; A_0 and A_t represent the absorbance of MO at the beginning ($t = 0$) and at time t of the photocatalytic reactions, respectively. The MO degradation kinetics was analyzed by the pseudo-first order reaction kinetics, which can be expressed by the following equation.

$$\text{Pseudo - first order rate equation, } \ln \frac{C_t}{C_0} = kt \quad (3)$$

where k represents the pseudo-first order rate constant (min^{-1}) and t represents time in min.

Figure 2.5a shows the time-dependent UV-visible absorption spectrum of 5 ppm MO solution in DIW and its gradual degradation during its photocatalysis in the presence of ZnO-4.

As shown in Figure 2.5a, the concentration of MO gradually decreased with respect to the time of photocatalysis. The characteristic absorption maxima of MO at 464 nm and 275 nm disappeared almost completely after 42 min of photocatalysis, which indicated its efficient degradation in DIW.

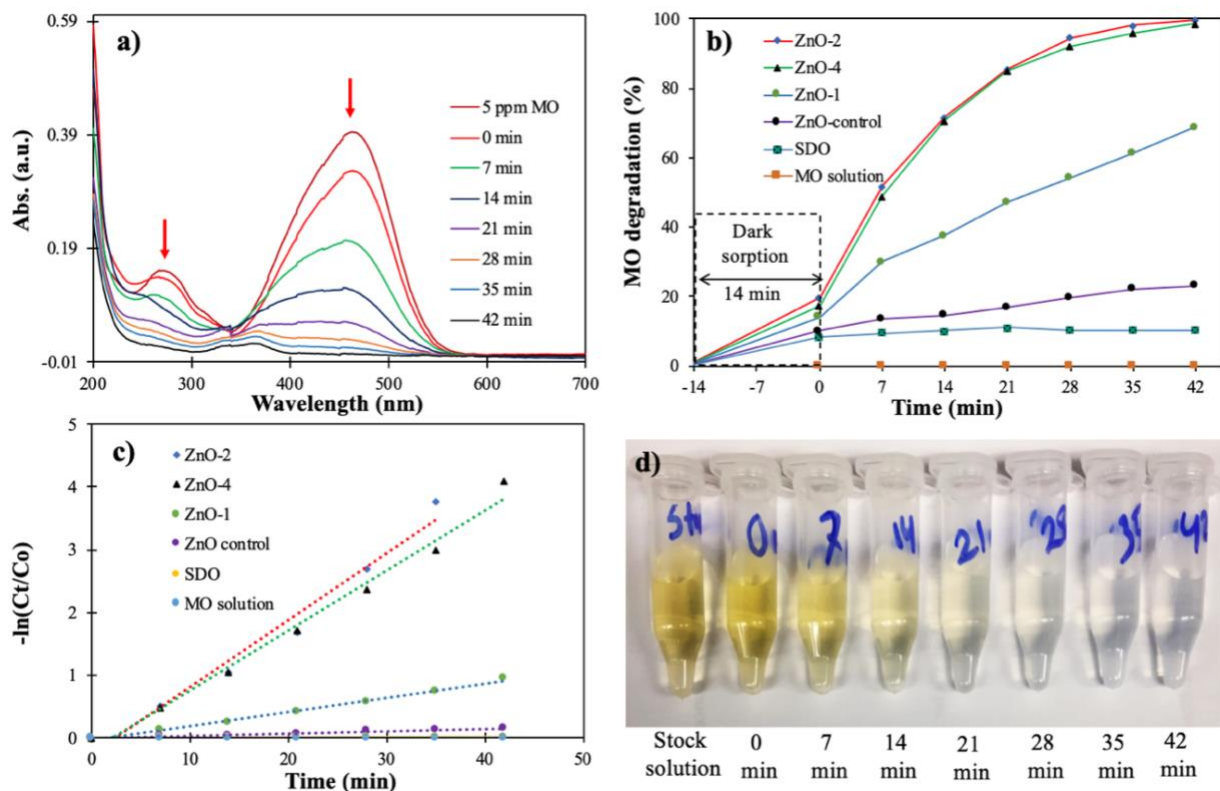


Figure 2.5: Time-dependent a) UV-visible spectrum of MO solution during photocatalysis by ZnO-4 in DIW, b) percent degradation of MO by different ZnO-n catalysts, c) Pseudo-first order kinetics of the degradation of MO, and d) digital photograph showing the gradual decolorization of MO solution during the photocatalysis by ZnO-4.

The time-dependent percent degradation of MO in DIW by different ZnO-n samples is shown in Figure 2.5b, whereas the digital photograph of the MO solution during the degradation is shown in Figure 2.5d. It was found that ZnO-4 and ZnO-2 were almost equally active and, in both cases, almost complete decolorization of MO solution was achieved after 42 min of light irradiation. On the other hand, ZnO-1 demonstrated comparatively slower activity, and about 69

% of MO was decolorized after 42 min. The slower photocatalytic activity of ZnO-1 compared to ZnO-4 and ZnO-2 could be attributed to the presence of a higher percentage of calcium oxide in ZnO-1, which was confirmed by XRD and EDX analyses. The ZnO-control showed only about 23 % MO degradation after 42 min of light irradiation. The slow photocatalytic activity of ZnO-control could be attributed to the presence of bulk/macroscale size of ZnO in it, which formed when no sawdust was used. Therefore, it could be inferred that sawdust mediated the formation of zinc oxide nanoparticles, which demonstrated higher photocatalytic activity in the degradation of MO in water. In other words, without sawdust, the method produces bulk/macroscale zinc oxide particles, which are not as active as ZnO-n for photocatalytic applications. Furthermore, it was found that the SDO had very low/no photocatalytic activity in the MO degradation, rather it showed about 9 % removal of MO by adsorption, Figure 2.5b. Also, the MO solution did not undergo any photolysis by UV light irradiation. About 10-20 % of the MO was adsorbed during the 14 min sonication and equilibration time, Figure 2.5b. Therefore, it could be confirmed that the decolorization of MO in the presence of ZnO-n happened via photocatalysis, not by adsorption and photolysis.

The presence of dissolved salts is one of the factors that can affect the photocatalytic performances of a photocatalyst. To determine whether the photocatalytic performance of ZnO-n was affected by dissolved salts (ionic strength), photocatalytic degradation of MO was carried out in simulated fresh drinking water, Figure 2.6. The time-dependent UV-visible spectrum of MO in simulated FDW during its photocatalysis by the ZnO-4 is shown in Figure 2.6a. In about 42 min of light irradiation, the characteristic peaks of MO flattened indicating its almost complete degradation. The photocatalytic performance of ZnO-n was found to be almost same as the DIW, which indicated that ZnO-n, synthesized in this study, is almost equally active in the degradation

of MO in water irrespective of the presence of dissolved salts, Figure 2.6b. For instance, ZnO-2 and ZnO-4 took about 42 min to degrade more than 98 percent of the MO in the simulated FDW matrix, which is similar to the deionized water as described before.

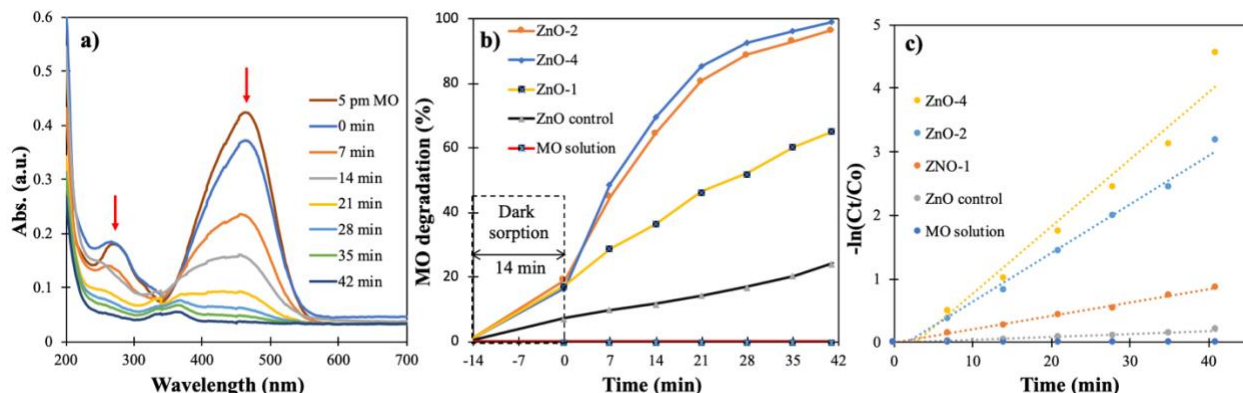


Figure 2.6: Time-dependent a) UV-visible spectrum of MO solution in simulated FDW during the photocatalysis by ZnO-4, b) percent degradation of MO by different ZnO-n catalysts, and c) Pseudo-first order kinetics of the photocatalytic degradation of MO.

The kinetics of the MO degradation was further analyzed by fitting the experimental results to the Pseudo-first order kinetic model. It was found that the $-\ln(C_t/C_0)$ vs. time (t) graph followed a linear trend, Figures 2.5c and 2.6b. Therefore, according to equation 3, it could be considered that the MO photocatalysis in DIW and simulated FDW followed pseudo-first-order reaction kinetics. Moreover, the linear relationship between $-\ln(C_t/C_0)$ and time (t) indicated the degradation of MO following the Langmuir–Hinshelwood (LH) mechanism. From the slope of the $-\ln(C_t/C_0)$ vs. time (t) graph the apparent rate constants (k_{app}) of the photocatalytic degradation of MO were calculated. The k_{app} of MO degradation in DIW was calculated to be 2.23×10^{-2} , 1.063×10^{-1} , 9.50×10^{-2} , and $3.80 \times 10^{-3} \text{ min}^{-1}$, $4.00 \times 10^{-4} \text{ min}^{-1}$, and 0.0 min^{-1} for ZnO-1, ZnO-2, ZnO-4, ZnO-control, SDO, and MO photolysis, respectively. Similarly, the k_{app} of MO degradation in FDW was calculated to be 2.10×10^{-2} , 7.68×10^{-2} , 1.05×10^{-1} , and $4.80 \times 10^{-3} \text{ min}^{-1}$, 0.0 min^{-1} for ZnO-1, ZnO-2, ZnO-4, ZnO-control, and MO photolysis, respectively. From these values it was

found that the degradation of MO over ZnO-2 and ZnO-4 in DIW were more than 24 and 27 times faster compared to the ZnO-control, respectively. Similar results were observed for the degradation of MO in simulated fresh drinking water.

The photocatalytic performance of ZnO-n for the degradation of MO in different water matrices are summarized in Table 2.1

Table 2.1 Summary of the photocatalytic degradation of MO in different water matrices on the ZnO-n.

Pollutants	Water Matrix	ZnO type	Rate constant (min ⁻¹)
MO	DIW	ZnO-4	9.50×10^{-2}
MO	DIW	ZnO-2	1.063×10^{-1}
MO	DIW	ZnO-1	2.23×10^{-2}
MO	DIW	ZnO-control	3.80×10^{-3}
MO	DIW	SDO	4.00×10^{-4}
MO	FDW	ZnO-4	1.05×10^{-1}
MO	FDW	ZnO-2	7.68×10^{-2}
MO	FDW	ZnO-1	2.10×10^{-2}
MO	FDW	ZnO-control	4.80×10^{-3}
MO	DIW	no catalyst	0.0
MO	FDW	no catalyst	0.0

Therefore, photocatalysis experiments suggested that the ZnO-n synthesized in this study, especially ZnO-2 and ZnO-4, could potentially be utilized for the photocatalytic degradation of MO in water under UV light irradiation. The ZnO-n prepared by the use of sawdust was found to be much more active than the one viz. ZnO-control synthesized without the sawdust. Therefore, it could be inferred that the sawdust mediated the formation of nanosized ZnO, which eventually provided photocatalytic activities. This also indicates the adaptability of the method for the preparation of other metal oxide nanoparticles using nitrate salts of different metals.

2.3.6. Cyclic Stability and Reproducibility of the Method of ZnO-n Preparation

Cyclic stability is one of the most important and desired properties of a photocatalyst. Therefore, the cyclic stability of the ZnO-4 (as the representative) was determined by conducting the degradation of MO for 5 cycles, Figure 2.7a. This result proved that the ZnO-4 was fairly active in the degradation of MO throughout the cycles although a minor loss of activity was observed over the cycles of use. The ZnO-4 degraded more than 95 percent MO in every cycle and a very slow gradual decrease in activity was observed. This decrease in activity could be attributed to the loss of ZnO and the photobleaching of ZnO, which is an inherent property of ZnO. Therefore, from the results of this study, it could be inferred that the ZnO-n, synthesized in this study, could be utilized as a robust and long-lasting photocatalyst for the degradation of organic contaminants in water.

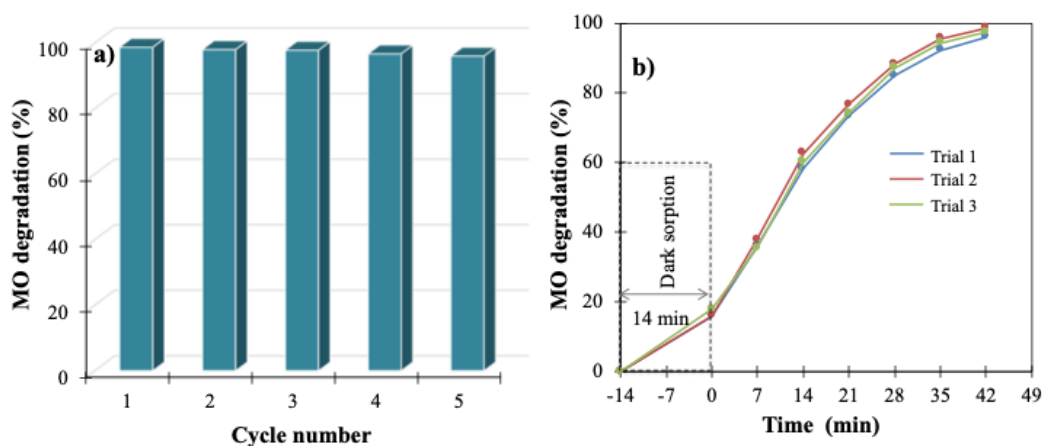


Figure 2.7: a) Cyclic stability of the ZnO-4 for MO degradation and b) Photocatalytic activity of ZnO-4 prepared in three independent trials.

The methodology for the preparation of ZnO-n was validated by synthesizing the ZnO-4 in three different trials followed by the analysis of their photocatalytic activity. It was found that the ZnO-4 synthesized in three different trials demonstrated similar activity in the degradation of 5 ppm MO in deionized water, Figure 2.7b. This result indicated that the method for the preparation of ZnO-n is very robust and reproducible while providing high photocatalytic activity.

2.3.7. Determination of the ROS Generated in the Photocatalytic Process

The generation of reactive oxygen species (ROS) such as hydroxyl radicals ($\bullet\text{OH}$), superoxide radical anions ($\text{O}_2^{\bullet-}$), and hydrogen peroxide (H_2O_2) is an important process towards the photocatalytic degradation organic pollutants on the semiconductor type metal oxide nanoparticles⁸⁰. These ROS, especially the $\bullet\text{OH}$, is a nonselective oxidizing agent, which leads to the degradation and eventually the mineralization of the organic pollutants via a series of reactions on the photocatalyst surface. The reaction involves the oxidation of hydrocarbon to alcohol, aldehyde, and carboxylic acid, and eventually, the decarboxylation to generate CO_2 and H_2O . As hydroxyl $\bullet\text{OH}$ is considered the primary ROS causing the degradation, the photocatalytic

generation of $\bullet\text{OH}$ on the ZnO-n was determined by the terephthalic acid (TA) photoluminescence (PL) technique. The working principle of this technique can be explained as follows: I) photocatalytically generated $\bullet\text{OH}$ on the ZnO-n reacts with sodium terephthalate to form 2-hydroxy terephthalate, II) 2-hydroxy terephthalate produces a strong fluorescence emission band centered at 425 nm at an excitation wavelength of 315 nm, Figure 8a. The fluorescence intensity is proportional to the generation of $\bullet\text{OH}$ on the catalyst surface.

The results of terephthalic acid photoluminescence tests are shown in Figure 2.8. The time-dependent fluorescence emission spectrum of 2-hydroxy terephthalate solution catalyzed by the ZnO-2 (as a representative) is shown in Figure 2.8b. The fluorescence intensity of the 2-hydroxy terephthalate solution increased with respect to time, which indicated the ZnO-2 produced a higher amount of $\bullet\text{OH}$ with respect to the time of UV light irradiation.

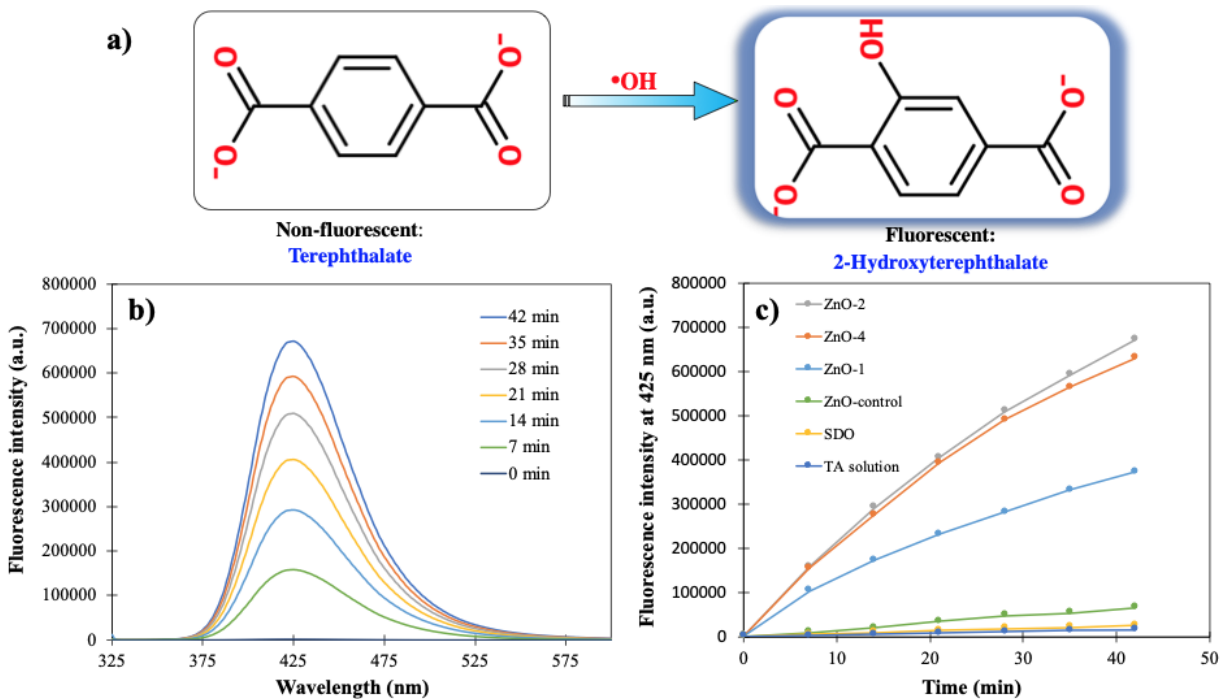
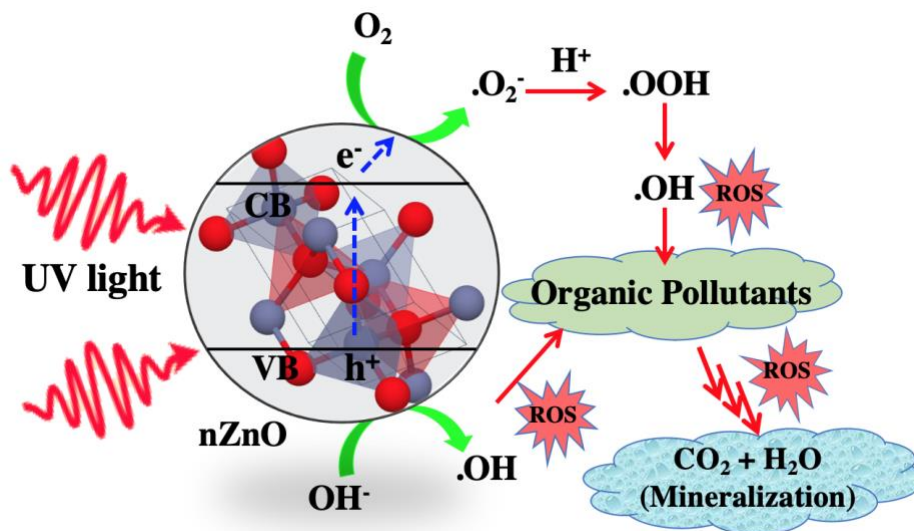


Figure 2.8: a) Reaction of terephthalate with $\bullet\text{OH}$ radical to form 2-hydroxy terephthalate, b) Time-dependent fluorescence spectrum of the 2-hydroxy terephthalate solution catalyzed by ZnO-2 (as a representative), and c) kinetics (fluorescence intensity at 425 nm Vs time) of the generation of $\bullet\text{OH}$ radical by different catalysts.

Figure 2.8c shows the kinetics of the generation of $\bullet\text{OH}$, studied through the fluorescence tests, by different ZnO-n prepared in this study. Figure 2.8c was obtained by plotting the fluorescence intensity of 2-hydroxy terephthalate solution at 425 nm Vs. the time of light irradiation. It was found that the rate of $\bullet\text{OH}$ generation by ZnO-2 and ZnO-4 was highest and almost similar compared to ZnO-1, ZnO-control, SDO, and TA solution only. These results further confirmed the higher photocatalytic activity of the ZnO-2 and ZnO-4 towards the degradation of MO (discussed before) compared to ZnO-1, ZnO-control, and SDO. Therefore, it is confirmed that the ZnO has the ability to generate ROS such as $\bullet\text{OH}$ under UV light irradiation, which leads to the degradation of organic pollutants in water.

2.3.8. Proposed Mechanism for the Photocatalytic Degradation of Organic Pollutants

The photocatalytic degradation of pollutants on semiconductor-type metal oxide nanoparticles such as ZnO can be depicted in Scheme 2.2. The mechanism is proposed based on findings ($\bullet\text{OH}$ generation studies, band gap analysis) of the current study and previously reported studies⁶². As ZnO is an n-type semiconductor metal oxide and has bandgap energy (E_g) of ~ 3.37 eV, it has two electronic band structures called valence (VB) band and conduction band (CB). The band gap of ZnO-1, ZnO-2, and ZnO-4 were found to be 3.15 eV, 3.21 eV, and 3.09 eV, respectively.



Scheme 2.2: Proposed scheme for the photocatalytic generation of ROS by the ZnO nanoparticles followed by the degradation of organic pollutants.

When the UV light of energy (in this case, ~ 302 nm or ~ 4.1 eV) equal or greater than the band gap of ZnO irradiates on the ZnO (in this case, 3.15 eV, 3.21 eV, and 3.09 eV for ZnO-1, ZnO-2, and ZnO-4, respectively), the photons of the incident light excites the VB electrons to the CB. The excitation of an electron leaves a hole (lack of electron) on VB. In this stage, several photochemical reactions happen simultaneously on the ZnO surface in the presence of water and oxygen. These holes (h^+) on the VB oxidize organic pollutants or inorganic species such as hydroxyl (OH^-) ions or H_2O to $\cdot OH$. The photoexcited e^- on the CB can reduce oxygen to generate various ROS such as $\cdot O_2^-$, $\cdot OOH$, and $\cdot OH$. These ROS are short-lived and highly reactive, which initiate a series of oxidation reactions leading to the gradual oxidative degradation of organic pollutants to CO_2 and H_2O , also known as mineralization. Therefore, generating reactive oxygen species is crucial for the photocatalytic activity of ZnO and other semiconductor-type metal oxide nanoparticles. However, the recombination of the exciton (photo-generated holes and electron pair) can lead to the loss of photocatalytic activity and the generation of photothermal heat.

2.4. Conclusions and Summary

Highly stable and photo-catalytically active zinc oxide nanoparticles (ZnO-n) of about 23 nm in size were synthesized by combusting a mixture of zinc nitrate salt and sawdust. Characterization of the ZnO-n was carried out by TEM, SEM, EDX, XRD, ICP-OES, and UV-visible spectroscopic analysis. The ZnO-4 and ZnO-2 displayed excellent efficiency toward the photocatalytic degradation of MO in aqueous solutions. >96% MO could be photo-catalytically degraded in about 42 min of UV light irradiation. The ZnO-4 and ZnO-2 demonstrated almost equal activity for the degradation of MO in deionized and simulated fresh drinking water matrices. As the generation of ROS species is a major step towards the degradation of organic pollutants, the generation of hydroxyl radical on the ZnO-n was confirmed by the terephthalic acid photoluminescence tests. Moreover, the reproducibility of the synthesis methodology was confirmed by triplicating the experiments and the ZnO-n demonstrated similar photocatalytic activities in every trial. Additionally, the ZnO nanoparticles demonstrated excellent robustness in terms of the photo leaching of zinc in solution over the commercial zinc oxide nanoparticles. Therefore, the ZnO nanoparticles, synthesized in this study, could potentially be utilized for sustainable water treatment technologies. The synthesis method could also be extended for the preparation of a wide variety of metal and mixed metal oxide nanoparticles for numerous applications.

Chapter 3: Preparation of Metastable Zinc Oxide Nanoparticles with High Photocatalytic Activity for Water Decontamination and Sanitation

3.1. Introduction

Nanomaterials possess fascinating physical⁸¹, chemical⁸², and biological⁸³ properties that can help to solve critical scientific and engineering problems today. They have received significant attention in a broad spectrum of applications, including but not limited to chemical catalysis⁸⁴, optics⁸⁵, photovoltaics⁸⁶, energy storage⁸⁷, sensors^{88,89}, electronics⁸⁹, biological and biomedical applications, and environmental remediation⁹⁰. Among various nanomaterials, Zinc Oxide (ZnO) is the most extensively used material owing to its physicochemical properties, stability, availability, nontoxicity, and low cost^{91,92}. As a photocatalyst, ZnO NPs have an excellent capability to degrade organic pollutants in water. However, for photocatalytic applications, nanoscopic ZnO (size 1-100 nm) is most suitable compared to macroscopic ZnO^{93,94}. The nanoscopic ZnO has a higher specific surface area, surface energy, and a suitable bandgap for separating the exciton that eventually allows for additional activation sites for the interaction and degradation of the pollutant⁹⁵. The degradation of organic pollutants by photocatalysis happens on the surface of the zinc oxide nanoparticles via redox processes⁹⁶. It is initiated by the electronic excitation between the valence band and conduction bands^{97,98}. Photocatalytic degradation is beneficial over other chemical processes as it is a chemical-free process and does not give rise to any other contamination⁹⁹.

Several strategies have been followed to synthesize photocatalytic ZnO NPs with various morphologies, such as nanorods, nanotubes, nanobelts, nanowires, and Nano mushrooms⁹⁸. Commonly employed techniques for synthesizing ZnO NPs include ball-milling, combustion synthesis, sol-gel process hydrothermal spray pyrolysis and chemical vapor deposition¹⁰¹⁻¹⁰³.

However, most techniques need expensive chemicals, complex approaches, and a long response time. Sometimes, it is challenging to synthesize nanomaterials with controlled particle size with reproducibility^{104,105}. Therefore, it is required to bring a facile, cost-effective, and environment safely technique to synthesize nanoparticles for photocatalytic applications if they have highly active catalytic activity via achieving metastable crystal states^{105,106}.

The combustion synthesis is a well-known and practical approach for synthesizing various metal oxide nanoparticles due to its simplicity, scalability, stability, and reproducibility^{107–109}. This synthesis procedure involves a mixture of metal salt, an oxidizer, and fuels heated to a high temperature (500 °C); the mixture goes through a fast decomposition reaction in the presence of air, producing high-purity metal oxide nanoparticles¹¹⁰. The problem that often emerges is that this process tends to produce metal oxides that have achieved thermodynamic stability, which tends to impart catalysis on their surface¹¹¹.

Modern dyes are extensively used in textile dyeing, cosmetics, pharmaceuticals, papermaking, food industries, and so on. Many of these dyes and their degradation products are toxic and can cause severe health conditions such as respiratory tract infection, vomiting, pain, hemorrhage, and other diseases^{112–114}. Most of these dyes are not readily degraded by light, heat, and biological agents available in nature. So, removing these dyes from the water bodies is essential before discharging them into the environment^{112,115}.

Methyl orange (MO) is a cationic dye, and it has many applications in food, cosmetics, textile, medicine, and leather-based industries^{116,117}. The release of MO into the aquatic environment from various sources poses severe environmental threats and toxic effects on living beings, considering that this dye is genotoxic, carcinogenic mutagenic, and resistant to degradation and remediation^{118,119}. The persistent pollution of these water sources caused by the dye at a rapid

pace poses a significant threat to the ecological balance of the environment as well¹²⁰. The elimination of organic contaminants in water has been a major concern in the treatment of wastewater due to the persistent nature of these pollutants¹²¹. Therefore, the degradation or removal of MO is essential to prevent its adverse effects¹²². A variety of physical, chemical, and biological methods have recently been used to eliminate MO from water. However, photocatalytic advanced oxidation processes (AOP) have recently drawn considerable scientific interest in degrading organic pollutants effectively from an aqueous environment due to their advantages over other approaches such as adsorption, coagulation, precipitation, filtration, and so on. Photocatalytic oxidative degradation is the chemical-free method for removing dyes and pollutants from the water^{123–125}. This process no longer produces any other pollutants and can degrade organic contaminants to mineralization, whereas other techniques move pollution from one area to another^{126,127}.

This paper reports a simple and fast method for the synthesis of ZnO NPs by using a biomass product such as saccharides to generate a new metastable form of ZnO NP with higher-than-normal photocatalytic chemistry to generate reactive oxygen species (ROS). The saccharides investigated were glucose, fructose, dextrin, and starch. Four different ZnO nanoparticle samples (Glucose-ZnO, Fructose-ZnO, Dextrin-ZnO, Starch-ZnO) were synthesized by burning the corresponding zinc nitrate hexahydrate $[Zn(NO_3)_2 \cdot 6H_2O]$ paste, and each of the saccharides at 500 °C and then used them as photocatalysts to degrade the MO dye (organic pollutants) in water. The photocatalytic activity and stability of the ZnO NPs was obtained through the photocatalytic degradation of MO dye in deionized water (DIW) and the simulated fresh drinking water (FDW) under UV-B light irradiation (360 nm) and sunlight irradiation. A fluorescence test evaluated the photocatalytic hydroxyl radicals ($\bullet OH$) generation by the ZnO NPs.

3.2. Materials and Methods

3.2.1. Materials

Glucose ($C_6H_{12}O_6 \geq 99.5\%$), fructose ($C_6H_{12}O_6 \geq 99\%$), dextrin ($(C_6H_{10}O_5)_n \geq 99.5\%$, starch [$(C_6H_{10}O_5)_n, \geq 95\%$]), zinc nitrate hexahydrate [$Zn(NO_3)_2 \cdot 6H_2O \geq 98\%$], Terephthalic acid [$C_8H_6O_4 = 98\%$] and sodium hydroxide ($NaOH \geq 98\%$) were purchased from Sigma Aldrich. Methyl Orange ($C_{14}H_{15}N_3O_3S > 98.0\%$) was purchased from TCI AMERICA. Salts used for the preparation of simulated fresh drinking water matrices such as sodium bicarbonate ($NaHCO_3, 99.5-100.5\%$), calcium chloride dihydrate ($CaCl_2 \cdot 2H_2O, \geq 99.5\%$), magnesium sulfate heptahydrate ($MgSO_4 \cdot 7H_2O, \geq 98. \%$), sodium silicate nonahydrate ($Na_2SiO_3 \cdot 9H_2O, \geq 98. \%$), sodium nitrate ($NaNO_3, \geq 99. \%$), sodium fluoride ($NaF, \geq 99. \%$), sodium phosphate hydrate ($NaH_2PO_4 \cdot H_2O, \geq 98. \%$) were purchased from Sigma Aldrich. The Analogue Hot Plate Stirrer (Fisher Scientific 11-600-49sh Isotemp) was used for the synthesis of ZnO NPs as a heating source. An ultraviolet box reactor (UVP Ultraviolet Cross-linker, Model CL-1000) containing UV-B fluorescent tube lamps was used for the photocatalytic degradation of MO and hydroxyl radical generation. The intensity of light was measured using a digital Light Meter LX1330B, and the intensity of light on the surface of the reaction was measured to be $\sim 22,000$ lux for the UV light in the box reactor and $\sim 100,000$ lux for sunlight. Syringe Filters with $0.45\mu m$ pore size were obtained from VWR to filter the reaction mixture for the UV-visible spectroscopic analysis. Milli-Q water ($> 18.20 M\Omega \cdot cm$ resistivity) was obtained from the Milli-Q (Advantage A-10) water filter system. The simulated fresh drinking water (FDW) was prepared by dissolving 252 mg/L $NaHCO_3$, 147 mg/L $CaCl_2 \cdot 2H_2O$, 124 mg/L $MgSO_4 \cdot 7H_2O$, 95 mg/L $Na_2SiO_3 \cdot 9H_2O$, 12 mg/L $NaNO_3$, 2.2 mg/L, NaF , and 0.18 mg/L $NaH_2PO_4 \cdot H_2O$ in the DIW which was formulated in accordance with the Nanotechnology Enabled Water Treatment guidelines.

3.2.2. Characterization Instrumentation

Scanning Electron Microscopy (SEM) images and Energy Dispersive X-ray (EDX) experiments were conducted using the Hitachi SU3500 microscope where carbon tape was used as a substrate for sample analysis. Transmission electron microscopy (TEM) experiments were conducted using a Hitachi H-7650 Microscope with an acceleration voltage of 80 kV. Carbon-film copper grid (200 mesh) was deposited with a suspension of ZnO NPs (0.2 mg/mL) in water and air-dried before imaging. Bruker D8 Discover X-ray diffractometer equipped with Cu K α radiation was used to obtain the ZnO nanoparticle X-ray diffraction (XRD) pattern. X-ray photoelectron spectroscopy (XPS) equipped with Al K α radiation was used to investigate the surface elemental composition and purity of ZnO NPs. The UV-Visible spectroscopic analysis was performed on the Agilent Cary 50 Conc UV-Visible Spectrophotometer. Standard quartz cuvette (10 mm path length) was used as the sample holder for the UV- vis studies.

3.2.3. Synthesis of ZnO NPs

Four different ZnO nanoparticle samples (Named Glucose-ZnO, Fructose-ZnO, Dextrose-ZnO, and Starch-ZnO) were synthesized using a similar experimental procedure shown in Scheme 1. For example, the synthesis of Glucose-ZnO is explained here. Glucose [1200 mg (3.51 mmol)], Zn (NO₃)₂·6H₂O [3569.88 mg (12 mmol)], and 2 mL of deionized water were thoroughly mixed in 150 ml of a glass beaker. The beaker was then placed on the hot plate, which was preheated to ~500 °C, and confirmed with an IR temperature gun. Within a minute of heating or burning, the mixture on the hot plate turned into a thick/viscous solution and instantly decomposed into a blackish-brown foam while producing yellowish-brown gases. The hot plate with blackish-brown powder/foam was put in a well-ventilated fume hood as the NO₂ and NO_x gases formed due to the breakdown of the zinc nitrate salt. Afterward, the form turned into a powder/foam that was placed

on the surface of the hot plate. During heating, the blackish-colored powder became a yellowish-white colored powder of ZnO NPs. After cooling, the ZnO NPs powder became white and was utilized for the characterization and the photocatalytic studies.

Additionally, A control ZnO sample (named ZnO-control) was also obtained using the same experimental procedure except without using any saccharides in the reaction mixture. In detail, the ZnO-control was synthesized by burning a mixture of [3569.88 mg (12 mmol)] Zn (NO₃)₂·6H₂O and 2 ml DIW (without using a saccharide) at ~500 °C in a 150 ml glass beaker on the same hot plate.

3.2.4. Methyl Orange (MO) Photodegradation Reaction Procedure

The performance of ZnO NPs towards the photodegradation of MO in DIW and simulated fresh drinking water was studied under UV and sunlight illumination. A concentration of 5 ppm (mg/L) MO solution was utilized for the photodegradation test in a 250 mL glass beaker. For effective photodegradation under the UV light, 30 mg ZnO NPs were taken in 30 ml MO (5 ppm) solution, and the mixture was put on for bath sonication for 15 min in the dark to reach the adsorption-desorption equilibrium between the MO dye and ZnO photocatalyst. Afterward, the mixture (MO dye and ZnO photocatalyst) was placed under the UV light in a box reactor. While the mixture was shined under the UV light, a 1 mL sample was drawn every 5 min. The same study was conducted under direct sunlight. 30 mg ZnO NPs were taken in 30 ml MO (5 ppm) solution, the mixture was put on for bath sonication for 5 min, and a 1 mL sample was drawn every 3 min. Then filtered with a syringe filter (0.45µm pore size) for UV-vis spectroscopic analysis. Finally, the MO degradation rate was monitored by the observing absorbance of MO at 464 nm wavelength.

3.2.5. Fluorescence Test for the Hydroxyl Radicals Detection

A 5×10^{-3} M stock solution of sodium terephthalate was prepared by adding terephthalic acid with a stoichiometric amount of sodium hydroxide in DIW. 30 ml of sodium terephthalate solution was taken in a glass beaker from the stock solution, and photo-reacted with the ZnO NPs under UV light. About 1 mL sample was drawn and filtered with the 0.45 μ m pore size syringe filters every 5 min at the time of photocatalysis. The fluorescence spectrum was obtained with an excitation wavelength of 315 nm, and to determine the qualitative amount of hydroxyl radicals in the solution, the fluorescence emission intensity at 425 nm was utilized.

3.3. Results and Discussion

This report describes a facile method to prepare ZnO NPs by combusting a mixture of saccharides (glucose, fructose, dextrin, and starch) and Zinc nitrate on a hot plate. Four highly active ZnO NPs samples named Glucose-ZnO, Fructose-ZnO, Dextrose-ZnO, and Starch-ZnO were prepared, and their photocatalytic properties in DIW and simulated FDW under UV light and sunlight irradiation were thoroughly studied. The wide bandgap energy of ZnO NPs allows them to absorb UV light, triggering a series of reactions that generate highly reactive oxygen species (ROS). These ROS play a crucial role in the degradation process and effectively break down organic pollutants such as MO.

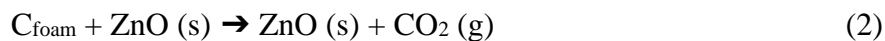
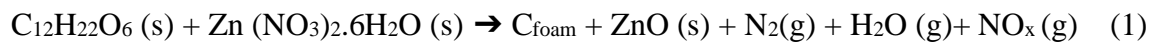
The present method offers several significant and notable advantages in terms of synthesis and applications. These include the simplicity of experimental conditions and procedures, robustness, and reproducibility, as well as the utilization of readily available poly or monosaccharides as precursor materials. Additionally, this method refrains from utilizing costly or hazardous materials and solvents, considering both cost-effectiveness and safety issues. The resulting ZnO nanoparticles demonstrate excellent photocatalytic activity for the degradation of

organic pollutants. Moreover, this method shows potential for large-scale synthesis of various metal and mixed-metal oxide nanoparticles by simply substituting zinc nitrate with nitrate salt of other metals such as magnesium, cobalt, cerium, copper, or iron. The synthesis methodology presented here will be able to generate the corresponding metal oxide nanoparticles based on the nitrate salt used. This versatility allows for the production of a wide range of nanoparticles, expanding the scope of potential applications in various fields. Overall, the choice of ZnO nanoparticles in this study is supported by their facile synthesis method, well-established photocatalytic activity, stability, cost-effectiveness, abundance, and environmental compatibility.

Because of industrialization and unsuitable removal of the contaminants from wastewater, getting clean water is narrowing down everywhere in the world. Improving existing water treatment processes and developing novel nanomaterials synthesis with intriguing properties can ensure sustainable water treatment technology with economic development. Recently the application of photocatalytic treatment for degrading hazardous organic pollutants in wastewater has gained attention due to its environmentally friendly nature, non-chemical treatment process, utilization of solar light, and suitability for economically low resources settings area. Therefore, there is a pressing need to develop a simple and rapid approach for preparing photo-catalytically active nanomaterials. Such advancements can greatly contribute to the optimization of photocatalytic water treatment systems, ultimately leading to improved access to clean water resources worldwide.

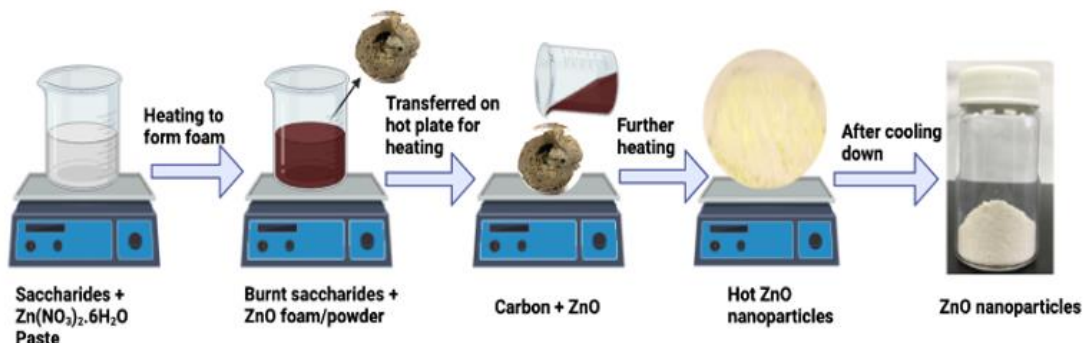
The ZnO NPs were prepared by burning Zn (NO₃)₂·6H₂O, and different poly or monosaccharides paste at ~500 °C on top of a hot plate as described in detail in the synthesis section. Scheme 3.1. Chemically, the poly or monosaccharides participated as the fuel, and zinc

nitrate salt participated as the oxidant in the combustion synthesis. The following reactions take place during the preparation of ZnO NPs:



Based on previous studies, the proposed mechanism for forming glucose ZnO NPs can be explained here. While the $\text{Zn} (\text{NO}_3)_2 \cdot 6\text{H}_2\text{O}$ and glucose mixture dissolves in water, it becomes concentrated to form a thick paste due to heating on the hot plate, thereby it undergoes a series of chemical reactions. On additional heating, the $\text{Zn} (\text{NO}_3)_2 \cdot 6\text{H}_2\text{O}$ immediately begins to decompose to form CO_2 , NO_2 , N_2 , H_2O , and nitrogenous gases. The decomposition reaction is represented by Equation 1. Simultaneously, glucose undergoes partial carbonization, resulting in the formation of a foam-like composite. It is considered that ZnO NPs become embedded within this partly carbonized glucose foam, Equation 1. This partially carbonized glucose acts as the interface/barrier and thus prevents the growth of ZnO enabling the nanoscopic size. Upon further heating, the partly carbonized foam undergoes oxidation at high temperatures, where the carbon converts to carbon dioxide (CO_2) through combustion. This combustion process leads to the liberation of carbon dioxide gas and the formation of yellowish-white ZnO NPs, Equation 2. The color of the ZnO NPs appears yellowish white when hot due to oxygen vacancies in the ZnO crystal lattice. However, the oxygen vacancies are filled upon cooling to room temperature, resulting in the ZnO NPs appearing white in color¹²⁸. This synthesis method allows for the integration of ZnO nanoparticles within the carbonized glucose matrix, providing a unique composite material with potential applications. Overall, the mechanism involves the decomposition of $\text{Zn} (\text{NO}_3)_2 \cdot 6\text{H}_2\text{O}$, partial carbonization of glucose, combustion of the carbonized foam, and the formation of ZnO

nanoparticles. This process allows for the synthesis of glucose-ZnO nanoparticles through a facile and scalable combustion method.



Scheme 3.1: Saccharides (glucose on the scheme above) mediated combustion synthesis of ZnO NPs.

3.3.1. TEM Analysis of the ZnO NPs

The results of TEM images suggested that the ZnO NPs (Dextrin-ZnO, Fructose-ZnO, Glucose-ZnO, and Starch-ZnO) were of different sizes and shapes with smooth surfaces, Figures 3.1 a, b, c, d. The TEM images also revealed that the particles tended to interconnect and overlap to form aggregates. The high surface energy and the high surface area of ZnO NPs could indicate the formation of aggregates and clusters. Using the ImageJ software, measuring the 100 randomly picked nanoparticles size, the ZnO NP's average size was determined. It revealed that Dextrin-ZnO had an average size of 20 nm, Fructose-ZnO had 35 nm, Glucose-ZnO had 32 nm, and Starch-ZnO had 22 nm, Figure 3.1e.

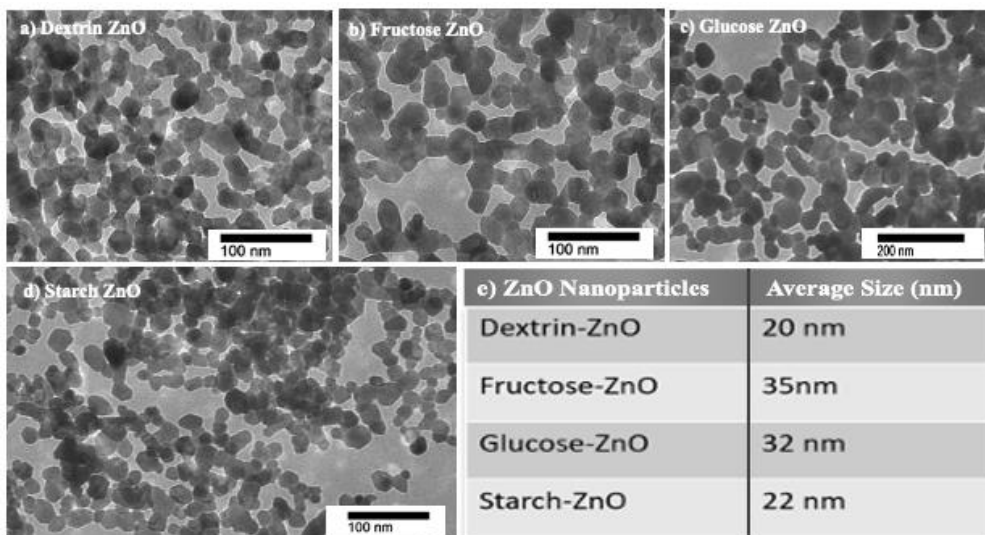


Figure 3.1: TEM images of the ZnO NPs a) Dextrin-ZnO, b) Fructose-ZnO, c) Glucose-ZnO, d) Starch-ZnO, and e) the average size of the ZnO NPs based on the TEM image.
 3.2.2. SEM Image and EDX Spectrum of the ZnO NPs.

3.3.2. SEM Image and EDX Spectrum of the ZnO NPs

The SEM and EDX images were obtained to observe the bulk morphology and the composition of elements of the ZnO NPs, respectively. The SEM image of the ZnO NPs (Dextrin-ZnO, Fructose-ZnO, Glucose-ZnO, Starch-ZnO, and ZnO Control) are shown in Figure 3.2 and The SEM image shows that the ZnO NPs were a powder-like texture with an aggregation pattern. The high surface energy of the nanoparticles might cause this aggregation.

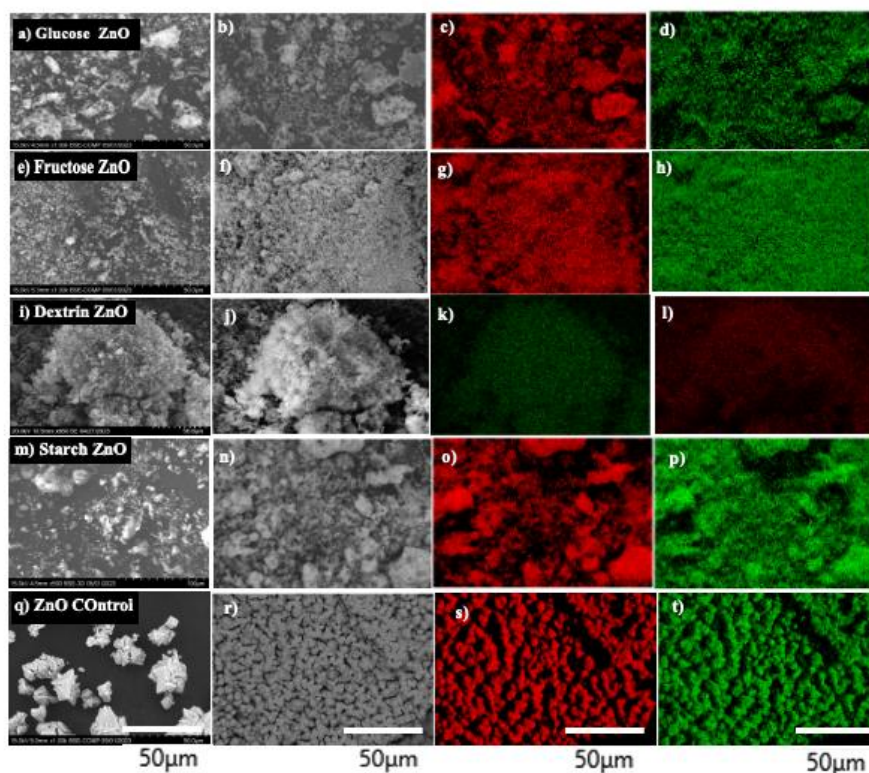


Figure 3.2: a) SEM image of the Glucose ZnO; b) SEM backscattered electron images of the ZnO NPs; c, d) X-ray EDS mapping of zinc and oxygen, respectively e) SEM image of the Fructose ZnO; f) SEM backscattered electron image of the ZnO NPs; g, h) X-ray EDS mapping of zinc and oxygen, respectively i) SEM image of the Dextrin ZnO; b) SEM backscattered electron images of the ZnO NPs; c, d)X-ray EDS mapping of zinc and oxygen, respectively m) SEM image of the Starch ZnO; n) SEM backscattered electron images of the ZnO NPs; o, p)X-ray EDS mapping of zinc and oxygen, respectively q) SEM image of the ZnO Control; r) SEM backscattered electron images of the ZnO NPs; s, t)X-ray EDS mapping of zinc and oxygen, respectively.

To obtain the elemental composition, the SEM-EDX spectrum was taken on Glucose-ZnO Fructose-ZnO, Dextrin ZnO, Starch ZnO, and ZnO control which is shown in Figure 3.3 a, b, c, d, and e respectively. Figure 3f represents the weight percent of Zn and O in each ZnO NPs which was obtained from the SEM-EDS spectrum. The EDX spectrum of all saccharides derived ZnO nanoparticles determined that no impurity or adulteration was there in the as-synthesized product since strong and prominent peaks generated by EDX spectra corresponding to Zn and O, Figure 3

(a-e). We believe that some other peaks originated except Zn and O is carbon peak which is originated from the carbon tape as carbon tape was used for the analysis as a substrate. This result of the SEM-EDX spectrum also confirmed the successful formation of ZnO nanostructures.

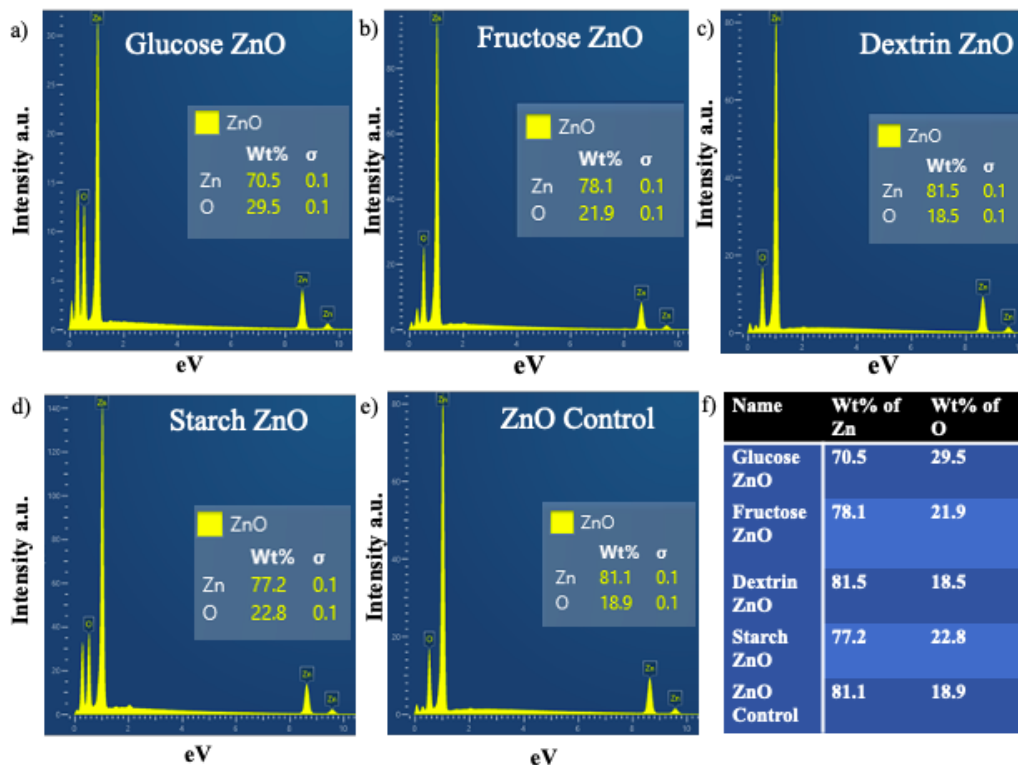


Figure 3.3: EDX spectra showing the elemental composition of a) Glucose-ZnO, b) Fructose-ZnO, c) Dextrin-ZnO, d) Starch-ZnO, and e) ZnO Control, f) weight percent of Zn and O in each ZnO NPs obtained from SEM-EDX elemental analysis.

3.3.3. UV-visible Spectrum of the ZnO NPs

To determine the bandgap energy of the ZnO NPs, zinc oxide nanoparticles suspension in ethanol (0.125 mg/mL) was used, and a UV-visible spectrum was carried out. The UV-visible spectrum of the ZnO NPs is shown in Figure 3.4. All the ZnO NPs generated a characteristic UV-vis absorption band centered at around 375 nm. The presence of a characteristic peak at around 375 nm across all ZnO NPs samples indicates that they share a common optical property in the

UV region. This observation suggests that there are no significant differences in the absorbance behavior of these samples at that wavelength. The absorption band in this region could be the excitation of electrons from the valence band to the conduction band ($O2p \rightarrow Zn3d$). It was also noticed that all the synthesized ZnO nanoparticle samples were very absorptive at the UV region in distinction to the visible region of the electromagnetic spectrum. These results further support that all the ZnO NPs used in this study acted as immensely active photocatalysts under UV light illumination.

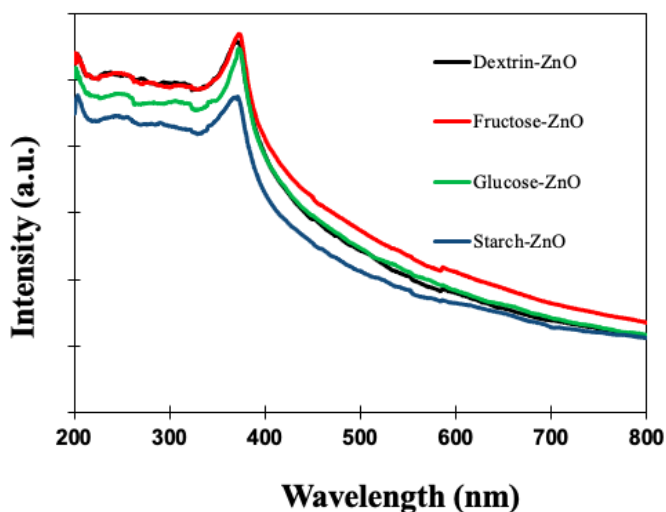


Figure 3.4: UV-visible absorption spectrum of ZnO NPs suspension in ethanol.

The band-gap energy was calculated from the following equation based on the absorption maximum.

$$E = hc/\lambda \quad (3)$$

where E is the energy (J), h is Planck's constant ($h = 6.626 \times 10^{-34}$ Js), c is the velocity of light (2.998×10^8 ms⁻¹), and λ is the wavelength (maximum absorption). The band-gap energy of 3.32 eV, 3.31 eV, 3.31 eV, and 3.32 eV were obtained for Dextrin-ZnO, Fructose-ZnO, Glucose-ZnO, and Starch-ZnO, respectively.

3.3.4. XRPD Analysis of the ZnO NPs

The ZnO NPs were further characterized by X-ray Powder Diffraction (XRPD) measurement to obtain the sample's crystalline structure and crystallite particle size. In Figure 3.5, it was shown that there exist sharp diffraction patterns and peaks which point out the ZnO nanoparticle's crystalline nature. Additionally, the diffraction peaks at $2\theta = 31.70^\circ, 34.20^\circ, 36.20^\circ, 47.46^\circ, 56.50^\circ, 62.70^\circ, 66.20^\circ, 67.80^\circ, 68.99^\circ, 72.40^\circ,$ and 77.10° are characteristic to the (100), (002), (101), (102), (110), (103), (200), (112), (201), (004), and (202) lattice planes of the crystalline hexagonal wurtzite structure of ZnO nanoparticles (JCPDS 5-0664), respectively¹²⁹.

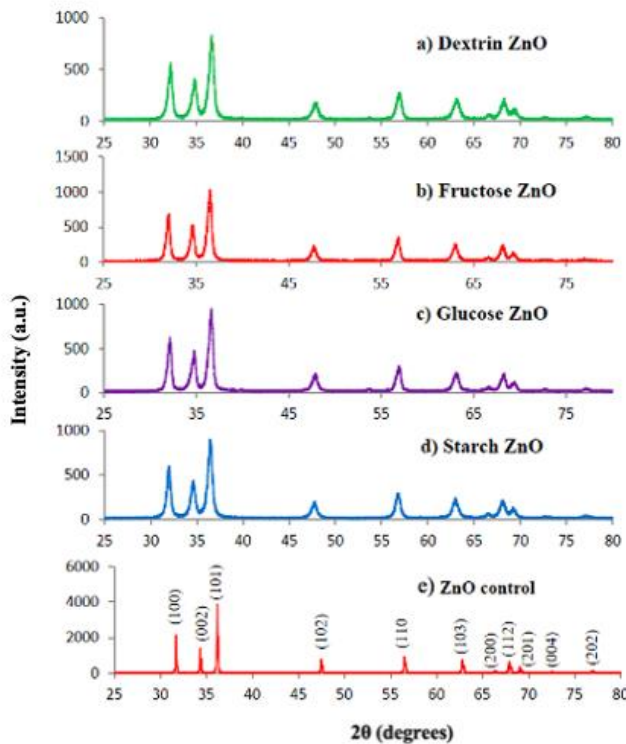


Figure 3.5: XRPD patterns of the ZnO NPs.

Moreover, the XRD pattern was conducted to observe whether any impurities were present in the ZnO NPs. Based on the XRPD pattern, it was obtained that the ZnO (101) diffraction peaks intensity is more prominent than any other peak, which is consistent with the expected trend that

ZnO NPs have a preferred growth toward the (101) crystallographic direction. However, the remarkable broadness of the diffraction peaks in the saccharides-derived ZnO NPs clearly indicates a semi-crystalline nature that points out a metastable phase that may be responsible for enhanced photocatalysis.

3.3.5. XPS Analysis of the ZnO NPs

The XPS analysis was conducted to assess the elemental composition, and chemical state of all the saccharides derived from ZnO NPS as well as investigate the purity of ZnO NPs. Figure 3.6. a, d, g, and h are the XPS survey spectrum of Glucose ZnO, Fructose ZnO, Dextrin ZnO, and starch ZnO, respectively¹³⁰. The XPS survey spectrum revealed that all the ZnO NPs derived from saccharides primarily consist of Zn and O with a small amount of C. It was assumed that this minimal amount of C was detected due to the contamination of the instrument. The XPS survey spectrums of ZnO NPs also showed the characteristic binding energies corresponding to the various Zn and O states^{130,131}. Figure 3.6.b represented the Zn 2p_{3/2} and Zn 2p_{1/2} peaks of Glucose ZnO at 1021.8 and 1045.4 eV for Zn element in ZnO NPs, respectively. Figure 3.6.e represented the Zn 2p_{3/2} and Zn 2p_{1/2} peaks of Fructose ZnO at 1022.4 and 1045.5 eV for the Zn element in ZnO NPs, respectively¹³². Figure 3.6.h represented the Zn 2p_{3/2} and Zn 2p_{1/2} peaks of Dextrin ZnO at 1022.7 and 1045.8 eV for the Zn element in ZnO NPs, respectively. Figure 3.6.k represented the Zn 2p_{3/2} and Zn 2p_{1/2} peaks of Starch ZnO at 1022.6 and 1045.7 eV for the Zn element in ZnO NPs, respectively. The peak observed at around 532 eV in the O 1s binding energy indicated the presence of O in the ZnO NPs in Figure 3.6. c, f, I, j. Moreover, O 1s exhibited two distinguishable peaks at about 532 eV and 533 eV which are attributed to the characteristic peaks of the Zn–O and the Zn-OH bonds, respectively on the surface of all the ZnO NPs. The OH group was more likely formed due to the breaking down of the Zn-O-Zn bond and the subsequent formation of the Zn-

OH bond during the synthesis. These results confirmed the purity of all saccharides derived ZnO NPs.

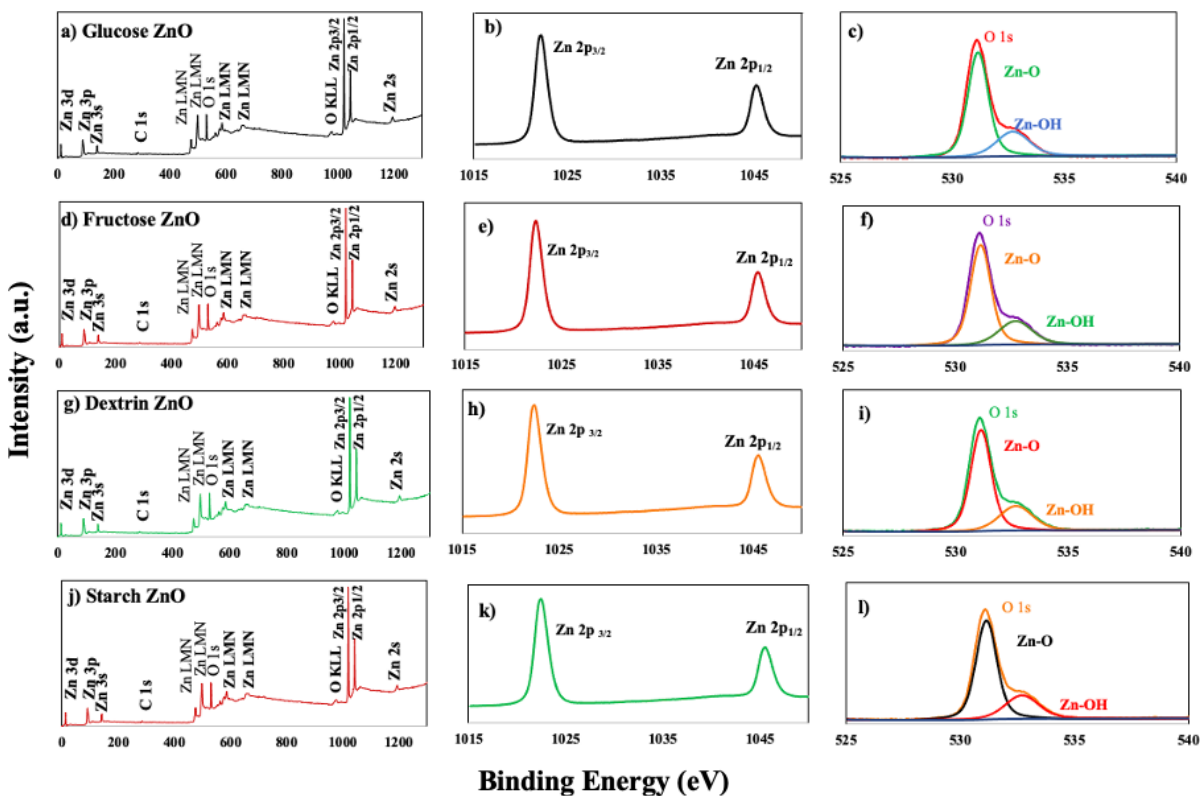


Figure 3.6: a) XPS survey spectrum of Glucose ZnO, b) XPS spectrum of Zn 2p, c) XPS spectrum of O 1s; d) XPS survey spectrum of Fructose ZnO, e) XPS spectrum of Zn 2p, f) XPS spectrum of O 1s; g) XPS survey spectrum of Dextrin ZnO, h) XPS spectrum of Zn 2p, i) XPS spectrum of O 1s; j) XPS survey spectrum of Starch ZnO, k) XPS spectrum of Zn 2p, l) XPS spectrum of O 1s.

3.3.6 Photocatalytic Degradation of Methyl Orange (MO).

All four ZnO NPs samples and the control ZnO sample synthesized in this study were subjected to degrade the MO dye in deionized water (DIW) and simulated fresh drinking water (FDW) under UV light and sunlight irradiation. The photocatalytic efficiency was determined by the percent degradation of MO using Equation 4. The degradation of MO was determined by its characteristic absorbance at 464 nm using UV-visible spectroscopy.

$$\text{Percent degradation} = \frac{C_0 - C_t}{C_0} \times 100\% = \frac{A_0 - A_t}{A_0} \times 100\% \quad (4)$$

C_0 is the initial concentration, C_t is the equilibrium concentration or concentration at time t of MO, A_0 is the initial absorbance, and A_t is the absorbance at time t of MO at 464 nm on the absorbance spectra, respectively.

As a representative, the UV-vis spectrum of the photocatalytic degradation of 5 ppm MO solution with the time by Fructose-ZnO in DIW is shown in Figure 3.7a. It could be found that with respect to the time during photocatalysis, the concentration of MO gradually decreased. The absorption maxima dropped almost to baseline at 464 nm after 20 min of reaction, which suggested the efficient MO photodegradation in water by Fructose-ZnO.

The percentage of MO degradation with time by different types of ZnO NPs in DIW is in Figure 3.7b. It was found that fructose-ZnO was the most active photocatalyst, whereas Glucose-ZnO and Dextrin-ZnO achieved complete decolorization after 25 min. Starch-ZnO demonstrated comparatively slower activity and reached complete degradation of MO after 35 min. Starch-ZnO shows relatively slower photocatalytic activity, which could be indicated by the dissimilarity in the formation of Starch-ZnO compared to others. When starch and zinc nitrate hexahydrate were mixed in water, it formed a thick dough-type suspension instead of a viscous solution for other saccharides. During burning on the hot plate, the starch and zinc nitrate hexahydrate mixture formed less foam during the decomposition, indicating a less specific surface area.

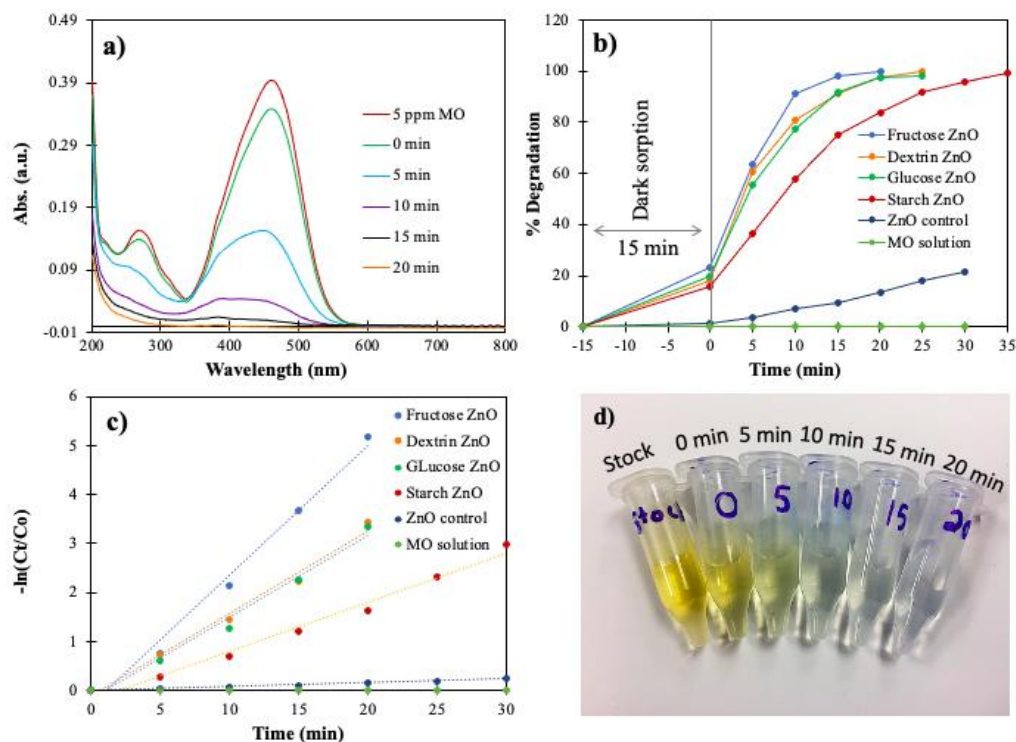


Figure 3.7: a) UV-vis spectra of MO (5 ppm) solution in DIW by Fructose-ZnO, b) percent degradation of MO with time by ZnO NPs, c) Pseudo-first order kinetics reaction of MO degradation, and d) A digital photograph of degradation of MO solution during photocatalysis by Fructose-ZnO.

After 30 min time of UV light exposure, the ZnO-control represented only about 22 % MO degradation under the same experimental conditions, which was possibly due to the more thermodynamically stable state achieved when no saccharide was used during the synthesis and its very low specific surface area and huge particle size as seen on SEM images. Moreover, no decolorization of MO solution was observed by just the UV light irradiation. Therefore, it could be concluded from the SEM images and the photocatalytic performances that saccharides assisted the formation of a metastable state of ZnO with nanoscopic size ranges and with a high active specific surface area that allowed high photocatalytic performance.

The photocatalytic degradation kinetics of MO by ZnO NPs was obtained by the pseudo-first-order kinetic model which is as follows.

$$kt = -\ln (C_t/C_o) \quad (5)$$

k is the reaction's photodegradation rate constant (min^{-1}). C_o is the initial concentration of the MO, which was at the beginning of the reaction, and C_t is the concentration of the MO at time t .

Figure 3.7c shows that MO photodegradation in DIW followed the pseudo-first-order kinetics mechanism, and the $-\ln (C_t/C_o)$ versus the time (t) graph followed the linear trends, and this linear relationship also suggested that the photocatalytic reaction of MO degradation followed the Langmuir–Hinshelwood model¹³³. A digital photograph of degradation of MO solution during photocatalysis by Fructose-ZnO in Figure 3.7d.

The photodegradation of MO was further studied in simulated fresh drinking water, considering the presence of dissolved salts is a factor that influences the photocatalytic performances of a photocatalyst. The UV-visible spectrum of MO photodegradation with time in simulated fresh drinking water (FDW) by the Fructose-ZnO as a representative is shown in Figure 3.8a. After 30 min of UV light illumination, it was found that the performance of all the ZnO NPs was almost the same as the DIW. Therefore, it could be inferred that the ZnO NPs prepared for MO photodegradation in water are nearly equally active in the presence of dissolved salts, Figure 3.8b.

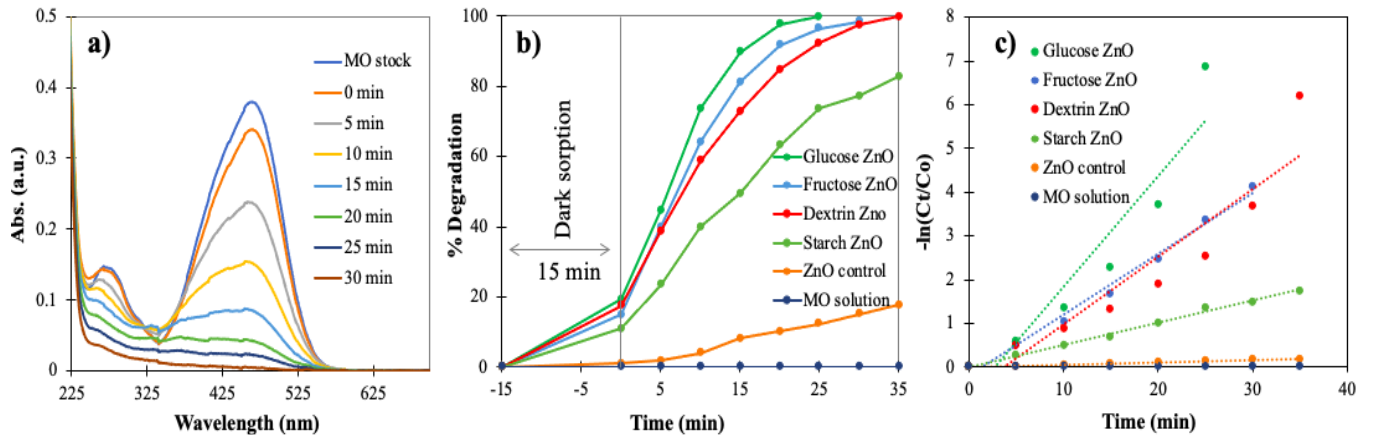


Figure 3.8: a) UV-vis spectra of the 5 ppm MO solution with time by Fructose-ZnO in simulated FDW, b) percent degradation of MO with time by different ZnO NPs derived from saccharides, and c) Pseudo-first order kinetics of the MO degradation reaction.

The $-\ln(C_t/C_0)$ vs. time (t) graph followed a linear trend in MO degradation in simulated FDW, like the MO degradation in DIW, in Figure 3.8c. Therefore, it is indicated that the MO photodegradation kinetics of DIW and simulated FDW followed the pseudo-first-order reaction mechanism. Moreover, this relationship between $-\ln(C_t/C_0)$ and time (t) of the photodegradation of MO followed the Langmuir–Hinshelwood (LH) mechanism as well¹³⁴. The rate constants (k_{app}) of MO degradation were calculated from the slope of the $-\ln(C_t/C_0)$ vs. time (t) graph which are given in Table 3.1 below.

The applicability of the ZnO NPs was further evaluated by the degradation of MO under sunlight irradiation. A bright sunny day was chosen to conduct the MO photodegradation reaction under sunlight irradiation. A very bright sunny day was chosen to conduct the MO photodegradation reaction under sunlight, and the average sunlight intensity was measured at ~100000 lux. The percentage of MO degradation with time by different types of ZnO NPs in DIW under sunlight is in Figure 3.9a. It was found that fructose-ZnO was the most active photocatalyst under direct sunlight as UV light and achieved almost complete degradation in 12 min, whereas Dextrin-ZnO achieved almost complete decolorization after 15 min and Glucose-ZnO achieved 92% decolorization after 15 min of Sunlight exposure. Starch- ZnO demonstrated comparatively slower activity and reached 92% degradation of MO after 18 min. It was assumed that for the same reason as MO photodegradation under UV light, Starch-ZnO shows relatively slower photocatalytic activity compared to others under direct sunlight.

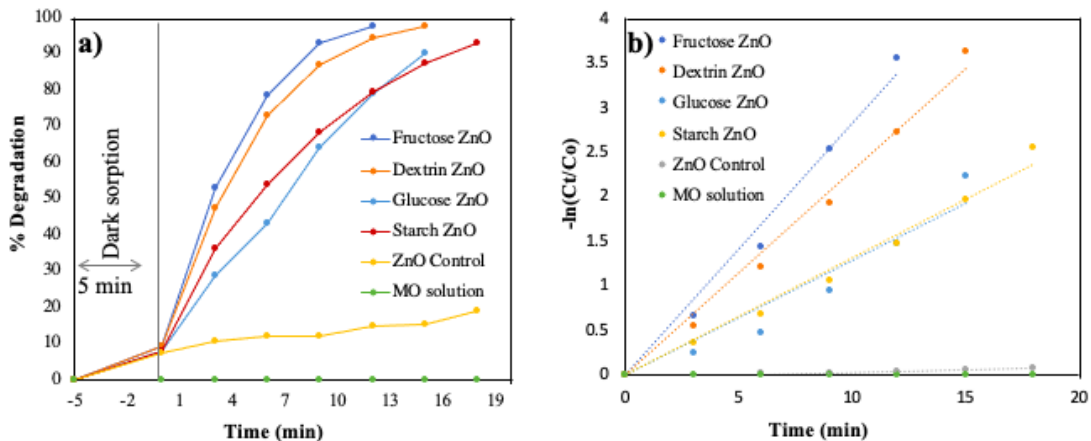


Figure 3.9: a) Time-dependent percent degradation of MO by different ZnO NPs derived from saccharides under sunlight, and b) Pseudo-first order kinetics of the MO degradation reaction.

After 18 min time of sunlight light exposure, the ZnO-control represented about 19 % MO degradation under the same experimental conditions when no saccharide was used during the synthesis. So, it appears here as well that saccharides assisted the formation of highly active ZnO NP with a specific surface area during the photocatalytic performance.

Figure 3.9b shows that MO photodegradation in DIW under sunlight followed the pseudo-first-order kinetics mechanism, and the $-\ln(C_t/C_0)$ versus the time (t) graph followed the linear trends, and this linear relationship showed that the photocatalytic reaction of MO degradation followed the Langmuir–Hinshelwood model as well.

Comparing the MO degradation under UV light and sunlight irradiation, it was found that the MO degradation was faster under sunlight illumination. This could be due to the higher intensity of sunlight (~100,000 lux) compared to UV light (22,000 lux) in the box reactor. Within the solar spectrum, UV light accounts for approximately 3-5% ($\lambda < 400$ nm), while 47% is attributed to visible light ($400 < \lambda < 700$ nm), and the rest is in the infrared region¹³⁵. This UV portion of the sunlight might have caused the photocatalytic activity of the ZnO NPs in MO degradation.

The rate constant of all the ZnO NPs for the MO photodegradation in DIW and simulated FDW are given in Table 3.1.

Table 3.1: Rate constants of all the photocatalytic reactions performed in this study.

ZnO Sample	MO Concentration	Water Matrix	Light source	Rate constant (min ⁻¹)
Glucose-ZnO	5 ppm	DIW	UV	1.62×10^{-1}
Fructose-ZnO	5 ppm	DIW	UV	2.65×10^{-1}
Dextrin-ZnO	5 ppm	DIW	UV	2.00×10^{-1}
Starch-ZnO	5 ppm	DIW	UV	1.19×10^{-1}
ZnO-Control	5 ppm	DIW	UV	7.62×10^{-3}
Glucose-ZnO	5 ppm	FDW	UV	2.54×10^{-1}
Fructose-ZnO	5 ppm	FDW	UV	1.39×10^{-1}
Dextrin-ZnO	5 ppm	FDW	UV	1.54×10^{-1}
Starch-ZnO	5 ppm	FDW	UV	5.03×10^{-2}
ZnO- Control	5 ppm	FDW	UV	5.57×10^{-3}
Glucose-ZnO	5 ppm	DIW	Sunlight	1.28×10^{-1}
Fructose-ZnO	5 ppm	DIW	Sunlight	2.82×10^{-1}
Dextrin-ZnO	5 ppm	DIW	Sunlight	2.29×10^{-1}
Starch-ZnO	5 ppm	DIW	Sunlight	1.32×10^{-1}
ZnO- Control	5 ppm	DIW	Sunlight	3.50×10^{-3}
MO Solution	5 ppm	DIW and FDW	UV	0.0
MO Solution	5 ppm	DIW	Sunlight	0.0

3.3.7. Determination of ROS generation by the ZnO NPs

The hydroxyl radicals ($\bullet\text{OH}$) generation was confirmed by the terephthalic acid (TA) photoluminescence (PL) study. The mechanism of action of this study is explained as follows: Sodium terephthalate reacts with the $\bullet\text{OH}$ (photo catalytically generated) on the ZnO NPs to form 2-hydroxy terephthalate which denotes a strong fluorescence emission band centered at 425 nm at an excitation wavelength of 315 nm. Therefore, it could be said that the higher the fluorescence intensity, the greater the quantity of generation of $\bullet\text{OH}$ at the water-catalyst interface.

The results of the TA PL tests are shown in Figure 3.10. The reaction of terephthalate with the photo catalytically generated $\bullet\text{OH}$ radical to form 2-hydroxy terephthalate is shown in Figure 3.10a. Figure 10b shows the fluorescence emission spectra of 2-hydroxy terephthalate solution with respect to time without the presence of ZnO. The fluorescence intensity of the 2-hydroxy terephthalate solution gradually elevated with the increment of the UV-light exposure time, which proved the graduate increase in the production of $\bullet\text{OH}$ with respect to the time under the UV light illumination. The time-dependent fluorescence emission spectra of 2-hydroxy terephthalate solution photocatalyzed by Dextrin-ZnO are shown in Figure 3.10c. Figure 3.10d shows the qualitative comparison in the production of $\bullet\text{OH}$ by the different ZnO nanoparticle samples synthesized in this report. Figure 3.10d was obtained by plotting the fluorescence intensity of 2-hydroxy terephthalate solution at 425 nm Vs. the time of light irradiation (kinetics of the generation of $\bullet\text{OH}$ radical by different ZnO NPs).

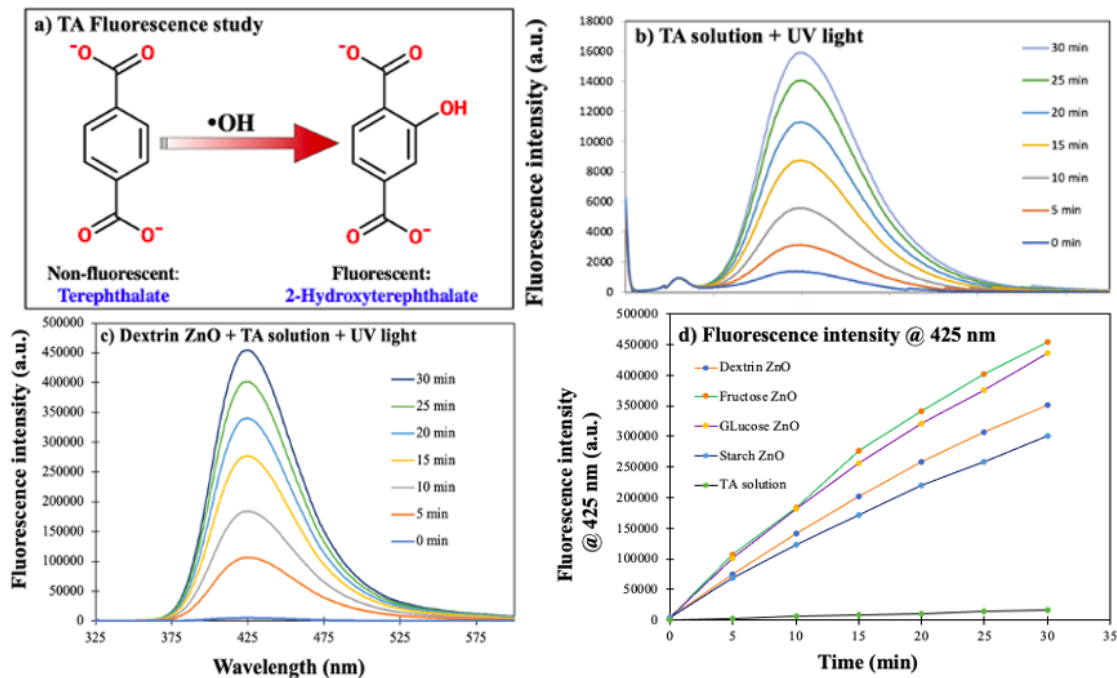
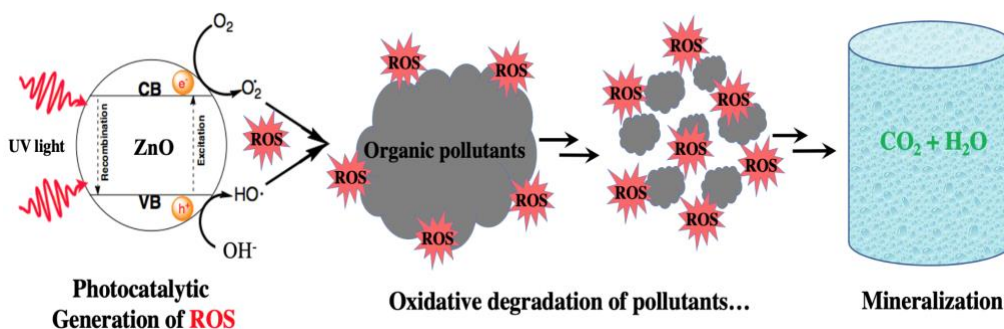


Figure 3.10: a) Reaction of terephthalate with the photo catalytically generated $\bullet\text{OH}$ radical to form 2-hydroxy terephthalate, b) time-dependent fluorescence emission spectra of 2-hydroxy terephthalate solution without ZnO NPs, c) fluorescence emission spectra of 2-hydroxy terephthalate solution photocatalyzed by Dextrin-ZnO with respect to time, and d) fluorescence emission intensity at 425 nm versus time graph for different ZnO NPs.

Based on the results of this PL study, it was found that the PL intensity of the TA solution at 425 nm catalyzed by ZnO NPS was much higher than the control TA solution that did not have any ZnO. These results in turn prove that the $\bullet\text{OH}$ was generated by the ZnO NPs while UV light irradiation. Like the MO degradation, Fructose-ZnO and Glucose-ZnO showed a higher rate of $\bullet\text{OH}$ generation than other ZnO NPs. Starch-ZnO had the slowest rate of $\bullet\text{OH}$ generation among all ZnO prepared in this study. These results further confirmed the higher photocatalytic performance of the ZnO NPs towards the oxidative degradation of MO. It was also confirmed that the ZnO NPs could generate ROS such as $\bullet\text{OH}$ under UV light irradiation, which can degrade organic pollutants in water.

3.2.8. Mechanism •OH Generation and the Organic Pollutants Degradation

The photocatalytic generation of hydroxyl radicals ($\bullet\text{OH}$) and the degradation of organic pollutants (MO) can be depicted as follows, Scheme 2. Since ZnO nanoparticles have a band gap of $\sim 3.2\text{eV}$, (3.32 eV, 3.31 eV, 3.31 eV, and 3.32 were obtained for Dextrin-ZnO, Fructose-ZnO, Glucose-ZnO, and Starch-ZnO, respectively) the photons of the incident UV light excite the conduction band (CB) electrons (e^-) to the valence band (VB). The excitation of electrons leaves an equal number of holes (h^+) on the CB, which can oxidize organic pollutants on the ZnO nanoparticles. The holes (h^+) can oxidize the hydroxyl ions (OH^-) to hydroxyl radicals ($\bullet\text{OH}$) in an aqueous solution, as determined by the terephthalic acid fluorescence study. This highly reactive $\bullet\text{OH}$ can degrade organic pollutants through oxidation.



Scheme 3.2. Proposed mechanism for generating hydroxyl radicals ($\bullet\text{OH}$) and organic pollutants degradation by ZnO NPs.

The photo-excited electrons (e^-) on the CB can reduce oxygen to produce superoxide radical anions ($\text{O}_2^{\bullet-}$), which can combine with protons (H^+) to form $\text{HO}_2\cdot$ radical. The $\text{HO}_2\cdot$ can react with another $\text{HO}_2\cdot$ to form H_2O_2 and O_2 . The H_2O_2 can dissociate into two hydroxyl radicals ($\bullet\text{OH}$) in water. All these ROS degrade organic pollutants to mineralization (harmless gases, *viz.* CO_2 and H_2O) through a series of reactions.

3.2.9. Cyclic Stability of the ZnO NPs.

The cyclic stability experiment was conducted to assess the stability of ZnO NPs by performing photodegradation of MO over 3 cycles. For that experiment, 30 mL of a 5 ppm MO solution with 30 mg of Fructose ZnO NPs (as a representative) was taken in a 250 mL beaker and exposed to the mixture under UV light for 30 minutes. Afterward, the mixture underwent centrifugation at a speed of 4000 rpm for 10 minutes to achieve a transparent supernatant. This transparent liquid was then subjected to UV-vis spectroscopy analysis to quantify the percent degradation of MO. This process was repeated for subsequent cycles using the centrifuged ZnO NPs.

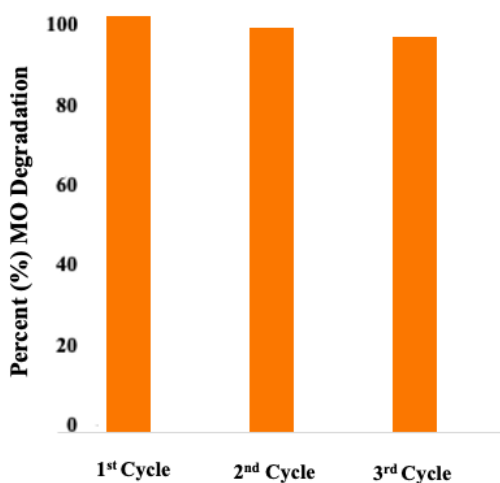


Figure 3.11. Cyclic stability of the ZnO NPs of MO degradation for 3 cycles.

The photocatalytic activity of ZnO NPs over the course of 3 cycles illustrates Figure 12. The results demonstrate that the ZnO NPs exhibited reliable performance throughout the study. In each cycle, more than 95% of MO was degraded by the ZnO NPs. Based on these findings, it can be inferred that the ZnO NPs synthesized in this study have the potential to serve as a durable and effective photocatalyst for the degradation of organic pollutants in wastewater.

3.4. Conclusions

By utilizing the combustion of saccharides (glucose, fructose, dextrin, and starch) and zinc nitrate salt, we successfully prepared ZnO NPs. These saccharide-derived ZnO NPs demonstrated

high efficiency in degrading MO dye from aqueous solutions under UV light and sunlight irradiation. Notably, the effectiveness in degrading MO was nearly equivalent in deionized water and simulated fresh drinking water matrices, highlighting the versatility of various water treatment applications. The ability of the ZnO NPs to generate hydroxyl radicals ($\bullet\text{OH}$) was confirmed through terephthalic acid photoluminescence tests, establishing their role in oxidizing organic pollutants. The stability of the ZnO NPs over multiple cycles demonstrates their durability and long-term effectiveness. This study not only demonstrates the preparation of phototactically active ZnO NPs for sustainable water treatment but also opens avenues for the preparation of various other metal and mixed metal oxide nanoparticles for numerous applications.

Chapter 4: Method Development for the Synthesis of ZnO Nanoparticles to Improve Photocatalytic Performance Under UV Light and Sunlight.

4.1. Introduction

Zinc oxide (ZnO) is a well-established semiconductor material with significant diverse applications ranging from photocatalysis and electronics to optoelectronics and sensors¹³⁶. Its wide band gap energy (~3.37 eV), extraordinary chemical stability, cost-effectiveness, non-toxic property, and tunable morphology have additionally enhanced its versatility^{137,138}. Among the numerous photocatalysts identified so far, zinc oxide ZnO nanoparticles (ZnO NPs) have achieved great potential owing to their excellent performance in photocatalysis for the degradation of pollutants in water^{139,140}. The performance of photocatalysis of ZnO NPs depends on several factors, including the nanoparticle's crystalline structure, specific surface area, surface morphology, and so on^{141,142}. The crystalline ZnO nanoparticles exhibit increased photocatalytic performance due to their well-defined crystal structures, leading to enhanced photodegradation efficiency^{143,144}. On the other hand, surface morphology can increase ZnO NPs surface area thereby providing elevated active sites for photocatalytic reactions^{145,146}. Moreover, it has a favorable unique material property of efficiently absorbing UV light making ZnO an excellent photocatalyst., which represents an effective and promising contestant for photocatalytic purposes and environmental remediation^{145,147}.

Among many other types of dyes, methyl orange (MO) is used in various industries, including the textile industry, dyeing, and printing industries as a coloring product^{148–150}. The discharge of MO from various industries introduces this dye into the water sources and consequently leads to water pollution¹⁵¹. Once MO dye releases into the waterbodies it can persist and cause serious effects on the aquatic system, which disrupts natural ecosystem balance^{152,153}.

Additionally, this vibrant dye color can visually pollute and can cause the unappealing and discolored appearance of the water. As a result, it has social and economic consequences as it may discourage tourism, recreational activities, and the utilization of water for various purposes. As the release of methyl orange dye into the water leads to water contamination and poses serious risks to the aquatic ecosystems, the well-being of aquatic organisms, and the sustainability of human activities dependent on clean water sources, so, it needs special attention to proper treatment, and management of this wastewater sources containing methyl orange dye to protect the water resources as well as the environment^{154,155}.

There are various methods available to synthesize ZnO NPs including Sol-Gel, hydrothermal Method, precipitation method, vapor deposition¹⁵⁶, template-assisted method^{157,158}, combustion method, and so on¹⁵⁹. Each synthesis method offers unique advantages and limitations in terms of ease of synthesis, scalability, stability, and performance. The selection of the method of synthesis relies on ZnO NPs required for specific purposes^{139,160}. In the previous study (chapter 3), ZnO NPs were synthesized by combustion method which is the burning of zinc nitrate hexahydrate [Zn (NO₃)₂·6H₂O] and sucrose (C₁₂H₂₂O₁₁) paste at 500 °C on the hot plate for the degradation of Methyl orange (MO) in water. In this study, we report the development of the combustion synthesis method of ZnO NPs by controlling the burning temperature in a tube furnace instead of on a hot plate at different temperatures for enhancing photocatalytic performance to degrade Methyl orange (MO) in deionized water. Five different ZnO NPs were synthesized at 400 °C, 500 °C, 600 °C, 700 °C, and 800 °C, ZnO NPs samples are named ZnO@400 °C, ZnO@500 °C, ZnO@600 °C, ZnO@700 °C, ZnO@800 °C in this report. Additionally, another ZnO sample was synthesized by combustion method on a hot plate which is named 'ZnO on hotplate' by following the previous study (chapter 3) to compare the photocatalytic activity MO in DIW water

with all the ZnO NPs (ZnO@400 °C, ZnO@500 °C, ZnO@600 °, ZnO@700 °C, ZnO@800 °C) synthesized by the modified method in this report. As far as we are aware that there is no existing published report for the modified synthesis method of ZnO NPs by the combustion method to degrade methyl orange (MO) dye in water.

Moreover, transition metals (Mn, Fe, Co, Ni, Cu, Ce, Cd) doped ZnO nanoparticles (TM-ZnO) with dopant contents of 1.0% and 5.0% (mole %). were prepared using the modified combustion method in a tube furnace at 600 °C to compare the photo catalytic activity with the pure the ZnO NPs (ZnO@600 °C)

Finally, the photocatalytic activity of ZnO NPs was further explored by applying the nanoparticles to the interior of a clay pot using the immobilization technique. The synthesis procedure involves applying the ZnO NPs (Fructose ZnO and ZnO@600 °C) to the clay pot interior and then placed in the furnace for heat treatment to allow the ZnO NPs to be calcined, which was then utilized for photocatalytic degradation of MO dye in the water. The synthesis and application of this technology are the special focus of this report for those who have limited access or no access to clean water.

4.2. Materials and Methods

4.2.1. Materials

Zinc nitrate hexahydrate [$\text{Zn}(\text{NO}_3)_2 \cdot 6\text{H}_2\text{O} \geq 98\%$], Sucrose ($\text{C}_{12}\text{H}_{22}\text{O}_{11} > 99.5\%$), Manganese nitrate hexahydrate [$\text{Mn}(\text{NO}_3)_2 \cdot 6\text{H}_2\text{O}$], Iron zinc nitrate hexahydrate [$\text{Fe}(\text{NO}_3)_2 \cdot 6\text{H}_2\text{O}$], Cobalt nitrate hexahydrate [$\text{Co}(\text{NO}_3)_2 \cdot 6\text{H}_2\text{O}$], Nickel nitrate hexahydrate [$\text{Ni}(\text{NO}_3)_2 \cdot 6\text{H}_2\text{O}$], Copper nitrate hexahydrate [$\text{Cu}(\text{NO}_3)_2 \cdot 6\text{H}_2\text{O}$], Cerium nitrate hexahydrate [$\text{Ce}(\text{NO}_3)_3 \cdot 6\text{H}_2\text{O}$], Cadmium nitrate tetrahydrate [$\text{Cd}(\text{NO}_3)_2 \cdot 4\text{H}_2\text{O}$] were purchased from Sigma Aldrich. Methyl Orange ($\text{C}_{14}\text{H}_{15}\text{N}_3\text{O}_3\text{S} > 98.0\%$) was obtained from TCI AMERICA. The clay pot

was obtained from local sources. The Analogue Hot Plate Stirrer (Fisher Scientific) and a tube furnace were used for the synthesis of ZnO NPs as a heating source. UVP Ultraviolet Crosslinker (Model CL-1000) which is equipped with UV-B fluorescent tube lamps was utilized for the MO photodegradation reaction and a digital light Meter (model LX1330B) was used to obtain the intensity of light which was equipped inside the UV reactor. The UV lamp inside the UV box reactor generated a 360 nm wavelength of light, and the light's intensity on the MO photocatalytic degradation reaction surface was found to be ~22,000 lux. The sunlight intensity of light on the surface of the reaction was measured to be ~ ~100000 lux. A 0.45 μm pore-sized syringe filter (PTFE) was used to filter the MO photocatalytic degradation reaction mixture for the UV-visible spectroscopic analysis. Milli-Q water (resistivity $>18.20 \text{ M}\Omega\cdot\text{cm}$) was used as a source of deionized water.

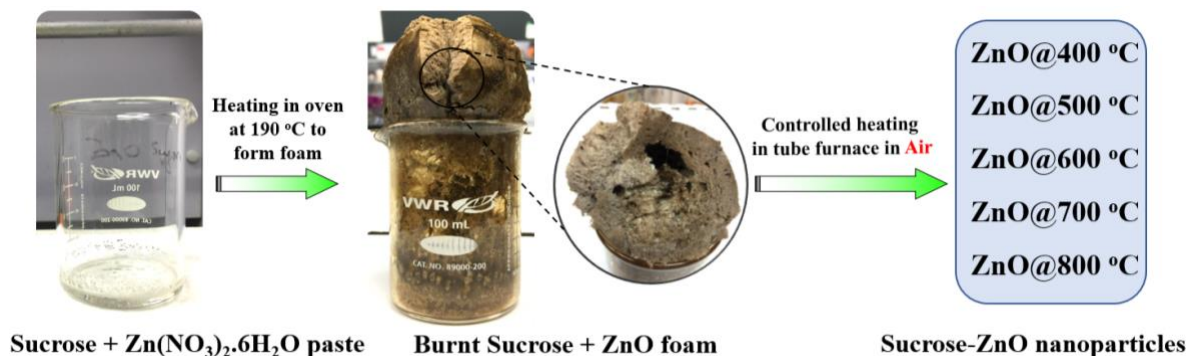
4.2.2. Characterization Techniques

Transmission electron microscopy (TEM) experiments were conducted using a Hitachi H-7650 Microscope with an acceleration voltage of 80 kV. Carbon-filmed copper grid (200 mesh) was deposited with a suspension of ZnO NPs (0.2 mg/mL) in water and air-dried before imaging. Scanning Electron Microscopy (SEM) images and Energy Dispersive X-ray (EDX) experiments were conducted using the JEOL JSM-IT100 microscope. Bruker D8 Discover X-ray diffractometer equipped with Cu $K\alpha$ radiation was used to obtain the ZnO nanoparticle X-ray diffraction (XRD) pattern. The X-ray photoelectron spectroscopy (XPS) analysis was performed in Thermo Scientific™ K-alpha™ equipment using a monochromatic Al $K\alpha$ X-ray source. The survey spectra were obtained with 130-eV pass energy, while high-resolution analyses for specific core levels were performed at 20-eV pass energy. An argon ions flood gun was used to avert surface charging. All binding energies were corrected with reference to carbon 1s at 284.8 eV. The UV-Visible

spectroscopic analysis was performed on the Agilent Cary 50 Conc UV-Visible Spectrophotometer. Standard quartz cuvette (10 mm path length) was used as the sample holder for the UV- vis studies.

4.2.3. ZnO NPs Synthesis

The ZnO NPs were synthesized by following a two-step preparation which is named a modified synthesis method. Zn (NO₃)₂.6H₂O and sucrose mixture was heated in an oven at 190 °C, for 40 min to form uniform foam, followed by annealing the foam in a tube furnace at different temperatures in the presence of air. An array of Sucrose-ZnO NPs [ZnO@400 °C, ZnO@500 °C, ZnO@600 °C, ZnO@700 °C, and ZnO@800 °C] were synthesized following the modified procedure shown in Scheme 4.1.



Scheme 4.1: Preparation of ZnO NPs by the modified method.

As an example, the detailed synthesis of ZnO@400 °C is explained below. First, 1200 mg (3.51 mmol) sucrose and 3569.88 mg (12 mmol) Zn (NO₃)₂.6H₂O salt were mixed with 2 ml deionized water in a 150 ml glass beaker. This mixture was dissolved by gentle heating on a hotplate. Then the beaker was placed in a preheated oven at 190 °C for 40 min to make blackish-brown foam. Afterward, the obtained blackish-brown foam was transferred to a ceramic crucible holder from the beaker, which was placed in a tube furnace for heating at 400 °C with a heating

rate of 2 °C/min under continuous airflow. Natural cooling was used to cool the furnace. Following the same procedure, four different ZnO nanoparticle samples were prepared.

Additionally, another ZnO sample was synthesized by a combustion method named ‘ZnO on hotplate’ which employs burning a mixture of 1200 mg (3.51 mmol) sucrose, 3569.88 mg (12 mmol) Zn (NO₃)₂·6H₂O salt, and 3 ml DIW at ~500 °C in a 150 ml glass beaker on the same hot plate. Upon heating Zinc nitrate salt underwent decomposition and produced blackish-brownish gases thereby forming brownish foam. Then the foam was transferred on top of the hotplate for further burning for around 20 min to obtain yellowish-white ZnO NPs. The hotplate was turned off and resulting in yellowish white ZnO NPs being allowed to cool down to obtain white ZnO NPs.

4.2.4. Photocatalytic Degradation Experiments Procedure

A Methyl orange solution with 5 ppm (mg/L) concentration was used for the photocatalytic experiments. In detail, 30 mg of the ZnO NPs (catalyst) was taken in 30 ml of 5 ppm MO solution in a 250 mL glass beaker and dispersed 10 min of bath sonication under the dark condition. Afterward, the mixture was irradiated under UV light with continuous agitation of about 300 rpm. At a regular interval of 5 min, 1 mL sample (MO solution) was withdrawn and filtered through a syringe filter (0.45µm) for UV–visible spectroscopic analysis. The MO percent degradation was monitored by observing the absorbance at 464 nm.

4.3. Results and Discussion

Recently the potential of semiconductor-type metal oxide photocatalysts has sparked the significant need for developing a facile method for the synthesis of highly active and environmentally friendly metal oxide nanoparticles. This report represents a straightforward and remarkably sustainable method for the synthesis of ZnO NPs by burning sucrose and Zinc nitrate

hexahydrate paste in a hot plate to make foam followed by carbonizing in the presence of air at different temperatures in a tube furnace. In terms of synthesis and photocatalysis, this synthesis method is more advantageous than other combustion methods previously studied. As ZnO NPs demonstrated efficient photocatalytic degradation of MO in water, this suggests that it could be a potential and viable candidate for making it suitable for practical application in the remediation of organic pollutants and wastewater treatment processes.

4.3.1. SEM and EDX Spectrum of the ZnO NPs

The SEM image was obtained to observe the surface appearance of the ZnO NPs and the EDX spectrum was employed to determine the composition of elements present in ZnO NPs. As a representative, the SEM image of the ZnO @600 °C is shown in Figure 4.1a. The SEM image depicts the ZnO NPs with a highly porous structure resembling a powdery aggregate pattern. This porous feature and aggregated pattern could contribute to the increased surface-to-volume ratio resulting in additional exposed surface area for the interaction in the photocatalytic reaction.

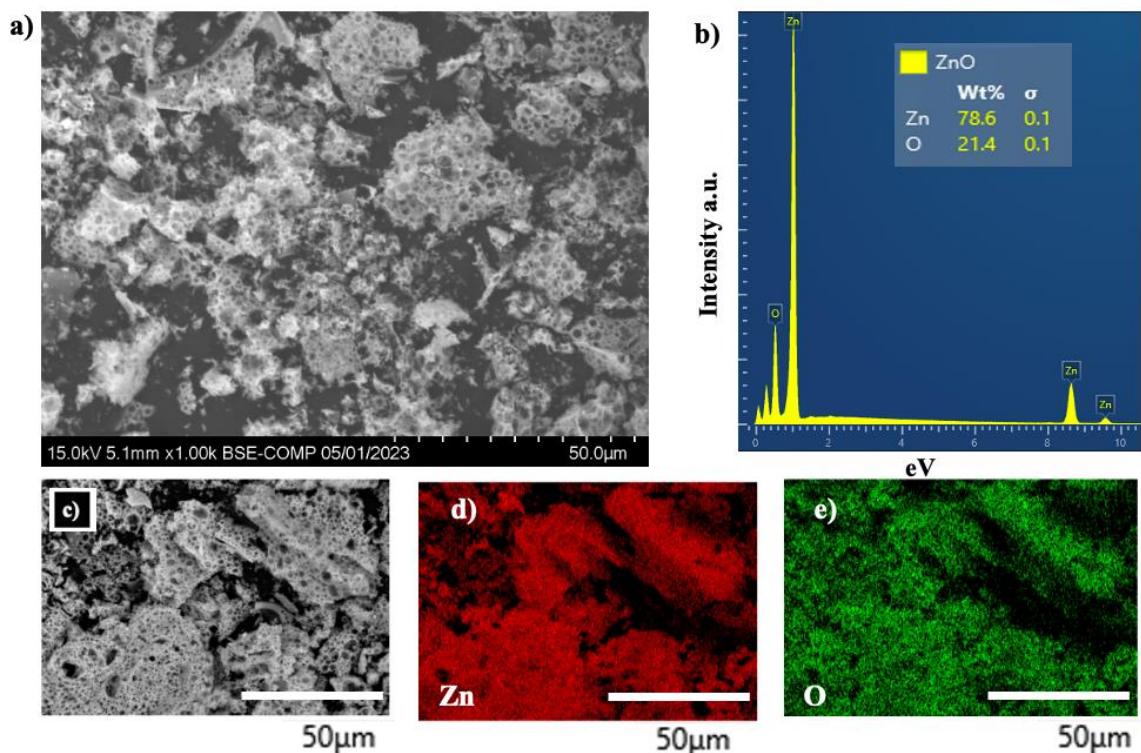


Figure 4.1: a) Typical SEM image of ZnO@600 °C, b) EDX spectra of ZnO showing the elemental composition, c) SEM backscattered electron image of ZnO d) X-ray EDS mapping image of zinc, e) X-ray EDS mapping image of oxygen.

EDX spectrum provides valuable insights about the elemental composition of ZnO@600 °C which is shown in Figure 4.1b. The EDX spectrum primarily depicts here prominent and dominant peaks corresponding to the Zn and O. Additional minor peaks were observed here also and we believe that it was from the carbon tape as during SEM image analysis, carbon tape was used as a substrate. SEM backscattered electron image of ZnO@600 °C is shown in Figure 4.1c. X-ray EDS mapping images of zinc and oxygen are shown in Figures 1d and 1e respectively. The above analysis of SEM and EDX spectra and elemental mapping image showed the successfully synthesized ZnO NPs.

4.3.2. TEM Images of the ZnO NPs

The TEM image of ZnO@800 °C was obtained to reveal the structure and morphology of ZnO NPs which is shown in Figure 4.2. From the figure, it could be observed that the nanoparticles are mostly aggregated and have bimodal size distributions. The average size of the smaller and larger nanoparticles was about 38 nm and 100 nm, respectively. The average size of the nanoparticle was calculated using ImageJ software.

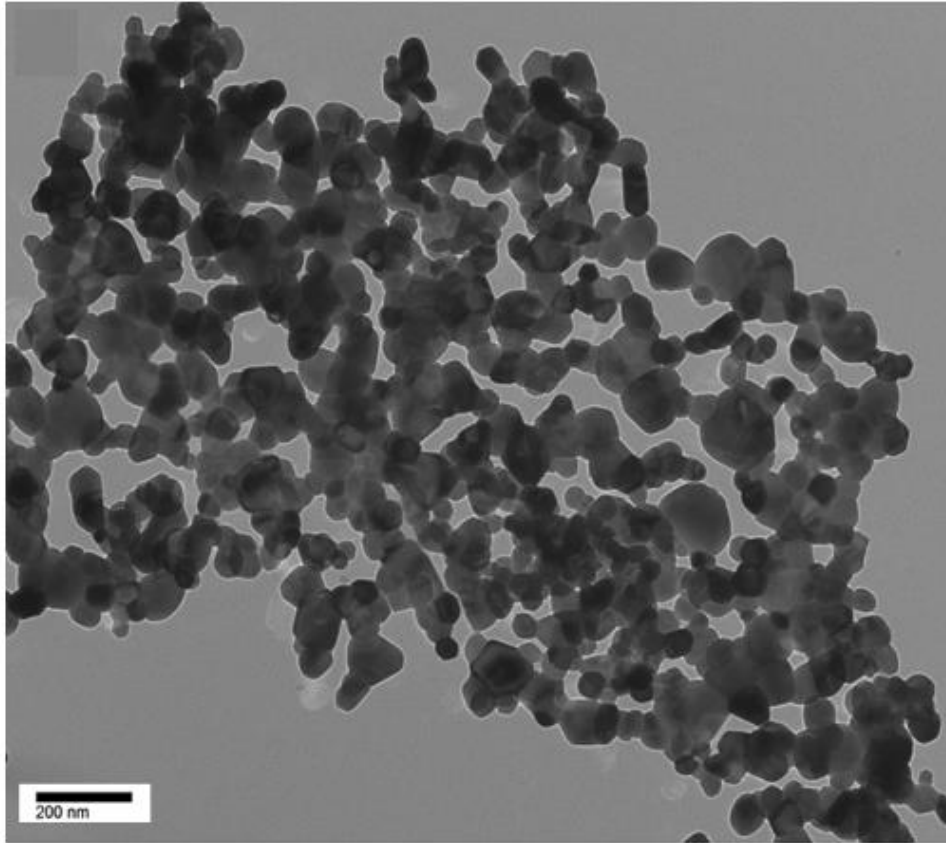


Figure 4.2: TEM image of ZnO@800 °C.

4.3.3. XRD of the ZnO NPs

The purpose of conducting X-ray diffraction (XRD) analysis was to examine the crystal structure and phase composition of the all the ZnO nanoparticles (ZnO@400°C, ZnO@500 °C, ZnO@600 °C, ZnO@700 °C, and ZnO@800 °C) that were synthesized. The resulting XRD pattern is shown in Figure 4.3 which exhibited clear and well-defined diffraction peaks at $2\theta = 31.7^\circ$, 34.4° , 36.2° , 47.5° , 56.5° , 62.8° , 66.3° , 67.9° , 69.0° , 72.6° , and 77.2° are characteristic to (100), (002), (101), (102), (110), (103), (200), (112), (201), (004), and 202 corresponding to the crystal planes of ZnO NPs, indicating the presence of a crystalline structure¹⁶¹. The positions and intensities of these peaks were consistent with the widely recognized wurtzite hexagonal structure

characteristic of ZnO NPs^{162,163}. No additional peaks attributable to impurities or secondary phases were detected, signifying the high purity of the synthesized ZnO nanoparticles.

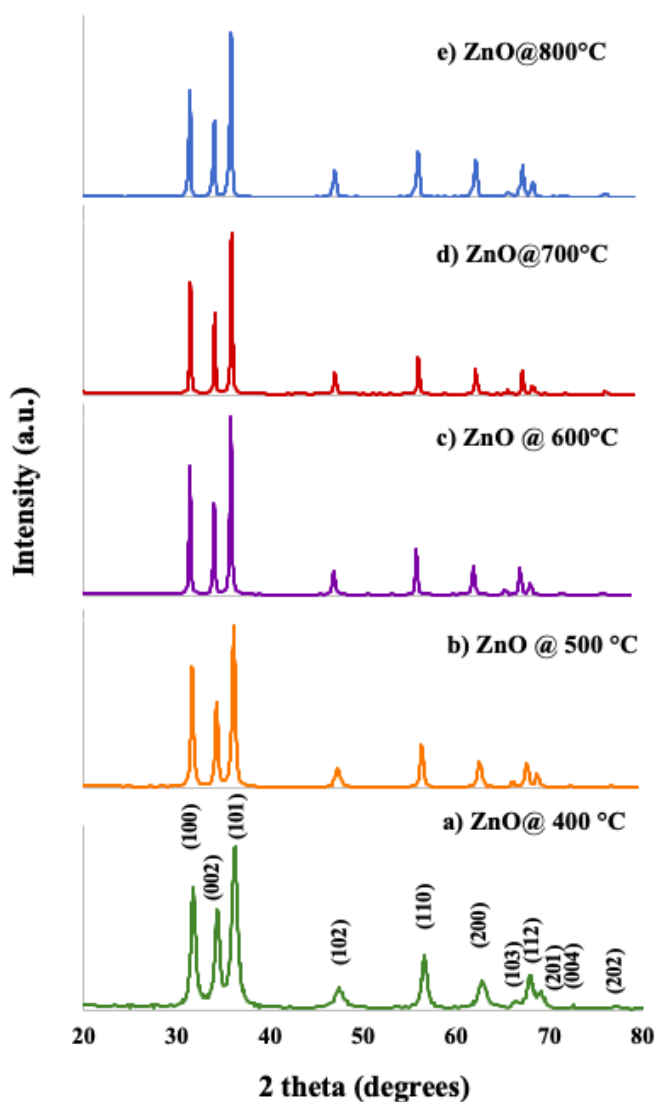


Figure 4.3: XRD of the ZnO NPs

Additionally, this investigation revealed an intriguing relationship between the synthesis temperature and the crystalline property of the ZnO nanoparticles. Figure 4.3.a demonstrates that ZnO@400°C, synthesized at 400 °C, exhibited a predominantly amorphous nature than the other ZnO NPs. However, as the temperature increased, the degree of crystallinity also significantly intensified as shown in this figure. This observation suggests that higher temperatures during

synthesis promote the formation and growth of well-defined crystalline structures within the ZnO nanoparticles. The evolution from amorphousness to enhanced crystallinity provides valuable insights into the thermal effects on the structural properties of ZnO nanoparticles. Finally, the XRD analysis confirmed the successful synthesis of ZnO nanoparticles and provided essential insights into their crystal structure and purity, affirming their potential applications in photocatalysis.

4.3.4. XPS of the ZnO NPs

The purity of the ZnO NPs, chemical states of the synthesized product, and elemental composition were obtained by the XPS analysis¹⁶⁴. It was found from the XPS survey spectrum that the ZnO primarily consists of Zn and O, with Only a trace amount of C in Figure 4.4a. The lowest amount of carbon may be obtained by the contamination of the instrument. This result suggests the purity of the ZnO sample. It was also found in the survey image of the XPS spectrum that the binding energies were characteristic to the ZnO, Zn (2s, 2p, 3s, 3p, 3d), Zn LMM, Zn LMN, O KLL, and O 1s. The Zn 2p_{3/2} and Zn 2p_{1/2} peaks observed at 1022.3 and 1045.5 eV, respectively were assigned to the presence of the Zn element in ZnO in Figure 4.4b¹⁶⁵. The binding energy of O 1s was found to be around the peak at about 531 eV in Figure 4.4c. It was found that O 1s showed two different peaks at 531.2 and 532.9 e. These peaks are associated with the presence of Zn–O and OH on the ZnO surface. It was assumed that the OH group may be obtained due to the breakdown of the Zn–O–Zn bond and the subsequent the formation of Zn–OH bond, during the synthesis process.¹⁶⁶

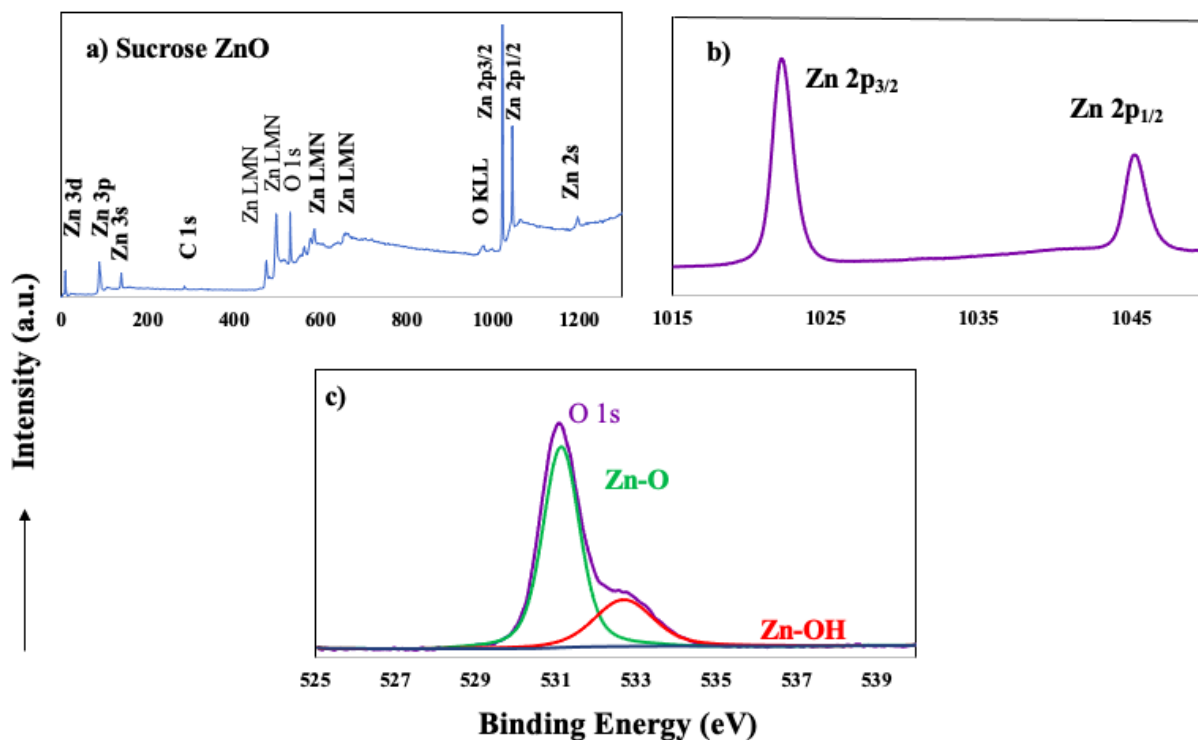


Figure 4.4: (a) XPS survey spectrum of the ZnO NPs, b) XPS spectrum of the Zn 2p, (c) XPS spectrum of the O 1s.

4.3.5. MO Photodegradation Reaction under UV-B Light

The degradation of MO was investigated utilizing ZnO NPs under UV and sunlight irradiation and the percent degradation was calculated using the following equation.

$$\text{Percent degradation} = \frac{C_0 - C_t}{C_0} \times 100\% = \frac{A_0 - A_t}{A_0} \times 100\% \quad (1)$$

C_0 is the initial concentration, C_t is the equilibrium concentration or concentration at time t of MO, A_0 is the initial absorbance, and A_t is the absorbance at time t of MO at 464 nm on the absorbance spectra, respectively.

The photocatalytic degradation kinetics of MO by ZnO NPs was obtained by the pseudo-first-order kinetic model, which is as follows.

$$kt = -\ln (C_t/C_0) \quad (2)$$

k is the reaction's photodegradation rate constant (min^{-1}). C_0 is the initial concentration of the MO, which was at the beginning of the reaction, and C_t is the concentration of the MO at time t .

The photocatalytic activity of the ZnO NPs prepared by modified methods was compared with the ZnO NPs that were prepared by the hotplate method. Figure 4.5. For this comparative study, the degradation of 5 ppm methyl orange solution in DIW under UV-B light irradiation was employed. It could be observed that the ZnO NPs synthesized by the modified method had a higher MO degradation rate than the ZnO NPs that were synthesized on the hotplate. For example, it took 25 min for almost complete degradation of MO by ZnO@500 °C, whereas the ZnO prepared on the hotplate had about 85 % MO degradation. Overall, the photocatalytic performance of the ZnO NPs synthesized by modified methods was about 40-45 % higher than the ZnO NPs that were prepared by the hotplate method. All the ZnO nanoparticle samples synthesized by the modified method had a similar MO degradation rate; however, ZnO@500 °C demonstrated the highest rate. This indicates that annealing at 500 °C in a tube furnace provides optimum conditions to achieve the highest photocatalytic performance.

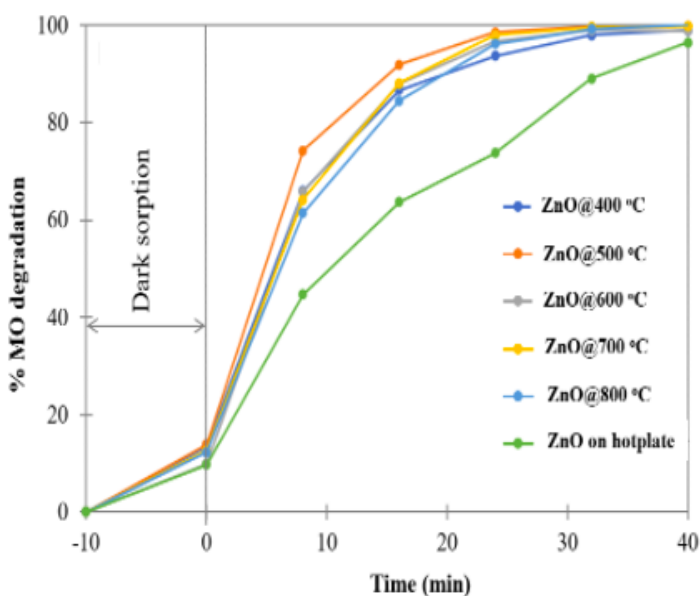


Figure 4.5: Time-dependent percent degradation of MO by ZnO prepared by the modified method compared with the hotplate method.

From this experiment, it could be inferred that the modified synthesis procedure (controlled heating in an oven followed by annealing in a tube furnace) could be utilized to improve the photocatalytic activity of the ZnO nanoparticles. We assume that the controlled heating in a tube furnace provides higher purity and better crystallinity of the ZnO nanoparticles, which was proved by XRD measurements, and eventually increases their photocatalytic activity.

4.3.6. MO Photodegradation Reaction under Sunlight

Considering the presence of approximately 5% UV light in solar radiation, and much higher intensity (100 000 lux) of UV radiation in sunlight, the MO photodegradation reaction was performed using ZnO@600 °C in DIW under sunlight illumination. For that 30 mg ZnO@600 °C catalyst in 30ml 5ppm MO solution was taken in a beaker and sonicated for 5 min and put the beaker under the sunlight light with continuous stirring. About 1 ml was withdrawn for UV-vis analysis for a certain period. Figure 4.6a represents the complete MO degradation of the UV-vis spectrum of 5 ppm MO solution in DIW with time in the presence of ZnO@600 °C. It could be observed that the ZnO NPs synthesized by the modified method had a higher MO degradation rate under sunlight illumination and achieved almost 100 percent decolorization in 15 min which is shown in Figure 4.6b and in Figure 4.6c shows the $-\ln(C_t/C_0)$ vs. time (t) graph followed a linear trend in MO degradation in DIW followed the Langmuir-Hinshelwood (LH) mechanism as well.

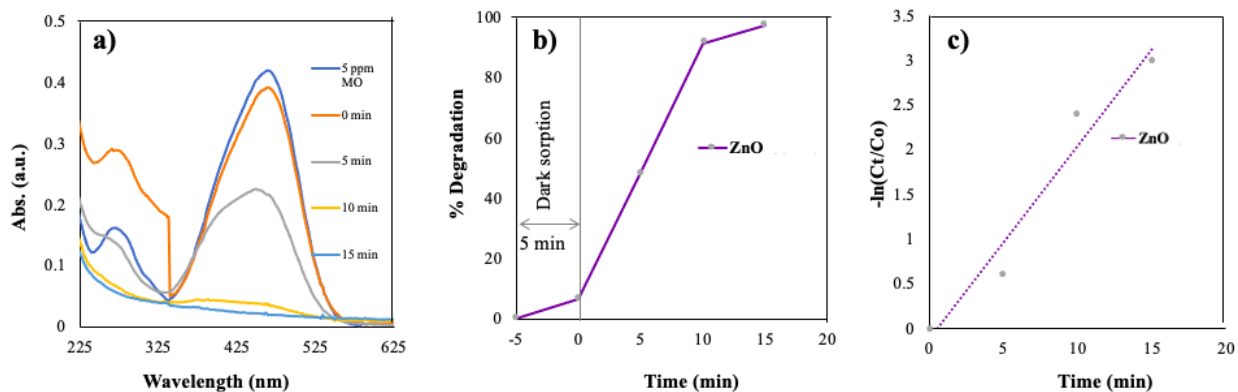


Figure 4.6: UV-vis spectra of MO (5 ppm) solution in DIW by ZnO @ 600 b) percent degradation of MO with time by ZnO NPs, c) Pseudo-first order kinetics reaction of MO degradation.

4.4. Synthesis of Transition Metal Doped ZnO NPs

Transition metal (Mn, Fe, Co, Ni and Cu, Ce, Cd) doped ZnO nanoparticles (TM-ZnO) with 1.0% and 5.0% (mole %) dopant content were prepared via the combustion method as described above. Stoichiometric amounts of dopant metal nitrate salt were used along with zinc nitrate salt and sugar mixture. Then the mixture was combusted and annealed at a high temperature to prepare the doped ZnO nanoparticles. Manganese nitrate hexahydrate $[\text{Mn}(\text{NO}_3)_2 \cdot 6\text{H}_2\text{O}]$, Iron zinc nitrate hexahydrate $[\text{Fe}(\text{NO}_3)_2 \cdot 6\text{H}_2\text{O}]$, Cobalt nitrate hexahydrate $[\text{Co}(\text{NO}_3)_2 \cdot 6\text{H}_2\text{O}]$, Nickel nitrate hexahydrate $[\text{Ni}(\text{NO}_3)_2 \cdot 6\text{H}_2\text{O}]$, Copper nitrate hexahydrate $[\text{Cu}(\text{NO}_3)_2 \cdot 6\text{H}_2\text{O}]$, Cerium nitrate hexahydrate $[\text{Ce}(\text{NO}_3)_3 \cdot 6\text{H}_2\text{O}]$, Cadmium nitrate tetrahydrate $[\text{Cd}(\text{NO}_3)_2 \cdot 4\text{H}_2\text{O}]$ was utilized as the precursors of Mn, Fe, Co, Ni, Cu, Ce, and Cd respectively. Sucrose was used as the fuel and zinc nitrate hexahydrate $[\text{Zn}(\text{NO}_3)_2 \cdot 6\text{H}_2\text{O}]$ acted as the oxidizing agent in the synthesis. After synthesizing, they named as Mn-ZnO, Fe-ZnO, Co-ZnO, Ni-ZnO, Cu-ZnO, Ce-ZnO, and Cd-ZnO, respectively.

A total of 14 samples were prepared following the same experimental procedure. Two different TM-ZnO (1.0% and 5.0%) nanoparticle samples were synthesized from each transition

metal. As a representative, 1.0 % Co-ZnO was described here. 1.0% Co-doped ZnO was prepared by mixing 1200 mg (3.51 mmol) sucrose, 3534.18 mg (11.88 mmol) $[\text{Zn}(\text{NO}_3)_2 \cdot 6\text{H}_2\text{O}]$, and 34.99 mg (0.12 mmol) $[\text{Co}(\text{NO}_3)_2 \cdot 6\text{H}_2\text{O}]$ with 2 mL deionized water in a 150 mL glass beaker. The mixture was dissolved by placing the beaker on a preheated hot plate. Then the beaker was placed in the oven at 190°C for 40 min to make partially combusted blackish-brown foam. Afterward, the blackish-brown foam was transferred from the beaker to a ceramic crucible (sample holder) and placed in a tube furnace for heating at 600°C to synthesize the Co-ZnO. The heating rate of 2 °C/min and natural cooling will be used for the ramp and cooling, respectively. Following the same experimental procedure, other transition metal-doped ZnO nanoparticle samples were synthesized. The only distinction among these samples was the variation in the molar ratio of the zinc nitrate hexahydrate to the dopant metal salt content. The as-synthesized Co-Zno was utilized for the degradation of MO under visible light/ sunlight.

The performance of the synthesized samples in terms of photocatalysis was evaluated by studying the degradation of aqueous MO under sunlight exposure. The photocatalytic degradation experiments were conducted in a glass beaker with a capacity of 250 mL. The initial concentration of MO in the solutions used for the experiments was 5 ppm (mg/L). In a typical procedure, 30 mg of the catalyst was dispersed uniformly in 30 mL of the MO solution using 5 minutes of bath sonication in the absence of light. This step ensured the establishment of an adsorption-desorption equilibrium between the MO molecules and the photocatalyst. Once the solution mixture was prepared, it was exposed to the sunlight source, and at regular intervals of 5 minutes, a 1 mL sample was extracted and filtered using a syringe filter. The filtered solution was then subjected to UV-visible spectroscopic analysis to determine the rate of MO degradation. This was done by

measuring the absorbance of the solution at a wavelength of 464 nm in the UV-visible spectrum specifically associated with MO.

As a representative, the photocatalytic activity of the Co-ZnO NPs is shown in Figure 4.7 as it was found that dopant metal oxide is not a good catalyst for the photodegradation of MO. In Figure 4.7a, UV-vis of 1.0% Co-ZnO was shown as a representative. It was observed from the UV-vis spectra that the 1.0% Co-ZnO showed no noticeable degradation of MO in DIW. Percent degradation of MO with respect to the time of 1.0% Co-ZnO, 5.0% Co-ZnO, ZnO@600 °C, and Only 5 ppm Mo solution was shown in Figure 4.7b. Here ZnO@600 °C is which was synthesized by the modified method in this report. From Figure 4.7b, it was found that both 1.0% Co-ZnO and 5.0% Co-ZnO did only about 6 percent of MO orange degradation or adsorption in 20 min whereas a ZnO@600°C degraded almost 100 percent of MO in 15 min. Moreover, there was no MO solution photodegradation observed in this case under sunlight as it was observed previously. Based on these findings, it can be inferred that the ZnO nanoparticles synthesized using the modified method described in this report exhibit higher photocatalytic activity compared to the Co-ZnO nanoparticles synthesized using the same synthesis procedure. It could also be concluded that the addition of transition metals (Mn, Fe, Co, Ni, Cu, Ce, Cd) to ZnO nanoparticles did not result in significant degradation of MO. Only pure ZnO nanoparticles exhibited high activity in degrading MO under sunlight irradiation.

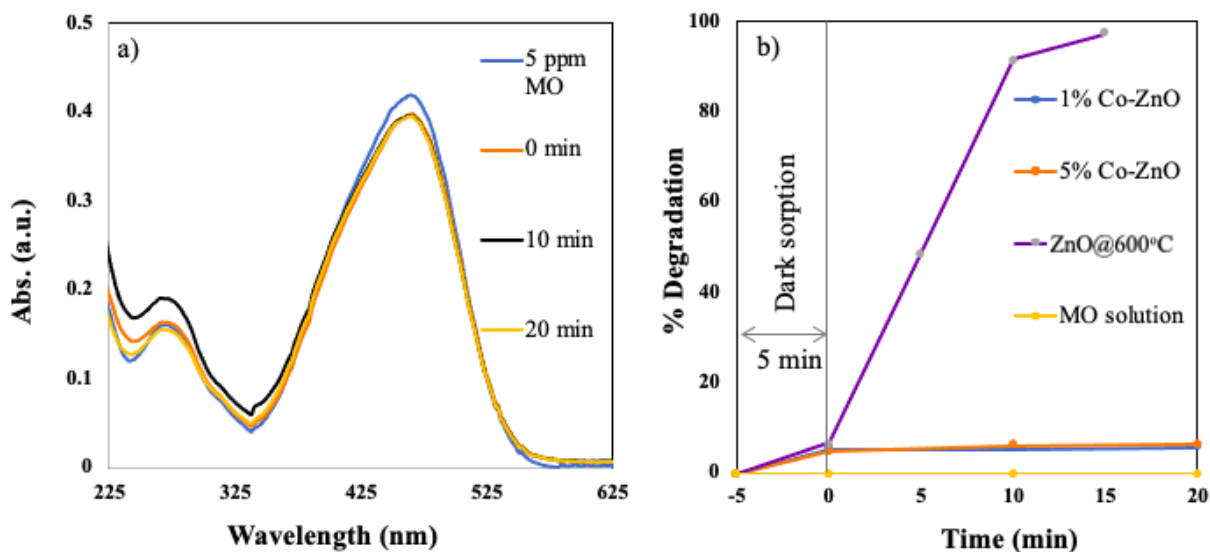
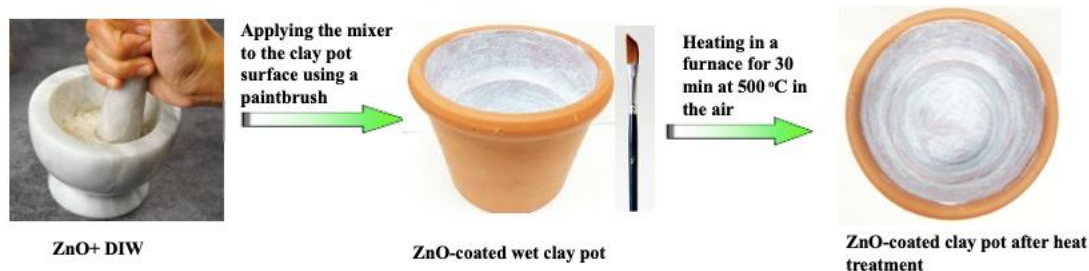


Figure 4.7: a) UV-vis spectra of the 5 ppm MO solution with time in DWI during the photocatalysis by Fructose ZnO-coated clay pot, b) percent degradation of MO with time by and ZnO@600C coated clay pot.

4.5. Surface Coating of Clay Pot Interior using ZnO NPs

This experiment was aimed at developing a prototype clay pot by coating the inner surface of the pot with Fructose ZnO nanoparticles for application in water sanitation and the degradation of organic pollutants (MO) in the water. Several methods have been developed for the immobilization of nanoparticles, e.g., the impregnation method, sol-gel, dip-coating, and chemical deposition. Among them, dip-coating is the most extensively used method owing to its simplicity, and it offers a convenient procedure that allows the direct immobilization of the ZnO NPs on the clay pot¹⁶⁷⁻¹⁶⁹. The detailed synthesis procedure is explained below and shown in Scheme 4.2. First, 250 mg of previously synthesized Fructose Zinc oxide nanoparticles powder) was mixed with 2 ml of deionized water in a mortar and pestle and grind it well for 30 min to make a white milky paint-like solution. Afterward, the milky paint-like ZnO solution was applied onto the clay pot interior as evenly as possible using a paintbrush and let dry for 30 min. This was followed by furnace heating at 500 °C for 30 min. Finally, natural cooling was used to cool the

furnace. Following the same synthesis procedure, another clay pot was coated with ZnO@600 °C, which was synthesized by a modified method to compare the activity with Fructose ZnO. In this case, instead of 250 mg only 5 mg ZnO NPs was used to coat the clay pot.



Scheme 4.2: Preparation of ZnO-coated clay pot by a dip coating method.

The photocatalytic photodegradation of MO in an aqueous solution was studied directly in the prepared ZnO-coated clay pot under Sunlight illumination. For effective photodegradation, 100 ml of 5 ppm MO solution was taken in a ZnO-coated clay pot. Then the pot was put under dark conditions for 10 min for the establishment of the adsorption-desorption equilibrium between the ZnO photocatalyst and MO dye. Afterward, the MO solution-containing clay pot was directly irradiated under the sunlight and at a given time interval, around 1 mL sample was drawn and filtered with a 0.45 μ m pore size syringe filter for UV-vis spectroscopic analysis. The MO percent degradation rate was observed by monitoring the absorbance of MO at 464 nm wavelength. The photocatalytic activity of the clay pot coated with ZnO NPs is shown in Figure 4.8. In Figure 4.8a, it could be observed from the UV vis spectra that the Fructose ZnO-coated clay pot showed almost complete degradation of MO in DIW. From Figure 4.8b it was found that a Fructose ZnO-coated clay pot which is coated with 250 mg of ZnO took 60 min almost 100 percent of 5 ppm MO degradation whereas a ZnO@600C coated clay pot which was synthesized by the modified synthesized method using only 5 mg of ZnO NPs took 60 min to degrade 35 percent of 5ppm MO.

From this result, it could be concluded that ZnO NPs synthesized by the modified method which is reported here are more active than the ZnO NPs synthesized by the hot plate method.

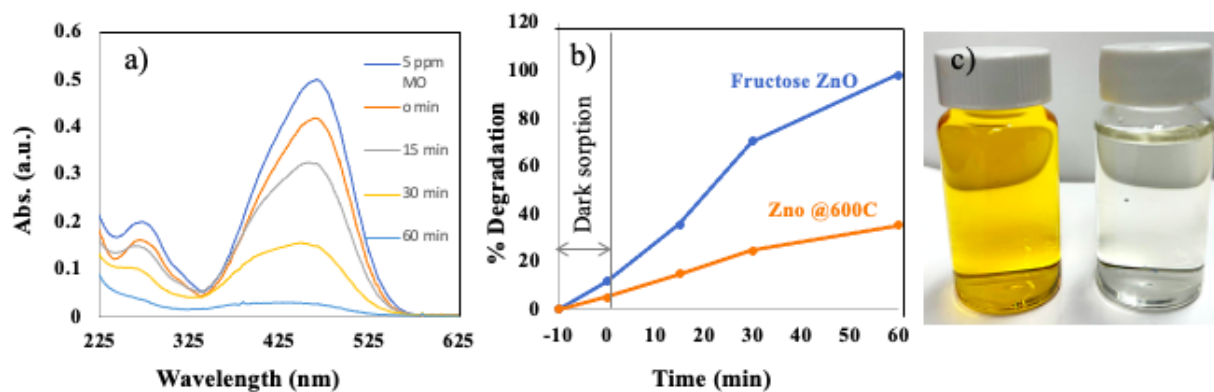


Figure 4.8: a) UV-vis spectra of the 5 ppm MO solution with time in DWI during the photocatalysis by Fructose ZnO-coated clay pot, b) percent degradation of MO with time by and ZnO@600C coated clay pot, c) digital photograph representing the decolorization of 5 ppm MO solution after photocatalysis by Fructose ZnO.

4.6. Conclusion

In summary, this report aims to explore the development of a method to improve the photocatalytic performance of ZnO NPs by controlling the heating rate during synthesis. The investigation of the photocatalytic performance of MO under both UV light and sunlight provided a clear understanding of the importance of heating rate during synthesis and results showed that photocatalytic activity is much more increased by the modified synthesis method. The SEM image showed the ZnO NPs synthesized with high surface area and the EDX image proved the successful formation of ZnO NPs. XRD pattern of all the ZnO NPs showed the crystallinity of ZnO NPs. The XPS results showed the purity of ZnO NPs. This study will contribute insights into the optimal heating rate necessarily required to achieve high crystallinity and high surface area in ZnO NPs and thereby improvement of their photocatalytic performance. The findings of this study will also provide implications for the development of sustainable, efficient, and environmentally friendly

methods for the treatment of water contaminated with organic pollutants, leading to a cleaner and healthier environment.

Chapter 5: Adsorptive Removal of Methyl Orange, Methylene Blue, Congo Red, and Bisphenol A from Water Using Zinc Oxide and Carbon Nanocomposite.

5.1. Introduction

The usage of organic dyes and endocrine-disrupting chemicals in different industries, coupled with their uncontrolled disposal into the environment, leads to the pollution of valuable water resources at multiple stages^{170,171}. Organic dyes are abundantly used in textile industries for coloring fibers and fabrics, and in food and beverage industries as food colorants to add the visual appeal of the product^{170,172}. They are also utilized in the cosmetic and personal care products, packaging and printing industries, ink production industries, and so on^{173,174}. Organic dyes have significant importance in the field of medical diagnostics, specifically in procedures such as medical imaging¹⁷⁵. The global annual production of various commercial synthetic dyes exceeds 700,000 tons. It is estimated that over 10,000 tons of dyes are used in textile sectors alone as they are the primary users of dyes and around 10-15% of the dye is discharged as wastewater throughout the dyeing process^{176,177}. As synthetic dyes, Methyl orange (MO), Methylene blue (MB), Congo red (CR) are considered highly toxic, non-degradable, and carcinogenic, and making it a significant concern for both visual aesthetics as well as the well-being of humans and aquatic organisms¹⁷⁸⁻¹⁸⁰. Consequently, it is crucial to eliminate these organic dyes from wastewater prior to its release into aquatic environments to address this issue¹⁸¹.

Bisphenol A (BPA) is an endocrine-disrupting chemical that can disrupt the regular functioning of the endocrine system in both humans and animals¹⁸²⁻¹⁸⁴. The endocrine system plays a vital role in regulating a wide range of biological processes by producing and releasing hormones into the bloodstream^{185,186}. These hormones are essential for controlling growth, development, metabolism, reproduction, and various other important functions within the body. It

has been found that even extremely low concentrations of BPA, measured in part-per-trillion (ppt), have the potential to induce birth defects, cancerous tumors, and various developmental disorders. In recent years BPA is a widely used monomer in the production of various plastics, polycarbonates, and epoxy resins. It possesses a mild estrogenic effect that can be detrimental to organisms, classifying it as a significant environmental pollutant due to its potential harm. Contamination of BPA has been found in various water sources through different pathways^{187–190}. Improper disposal or inadequate treatment of industrial effluents from BPA-utilizing industries, involved in the production of plastics, epoxy resins, and related materials, can result in the release of BPA-containing wastewater into the environment, thereby polluting nearby water bodies. When BPA-containing products, such as plastic bottles or food containers, are discarded or washed down drains, they ultimately end up in wastewater^{191–193}. Contaminated soil or landfill sites can serve as a source of BPA migration, allowing it to seep into groundwater and subsequently contaminate drinking water wells and other groundwater sources. Therefore, the elimination of BPA from water is essential for preserving human well-being, safeguarding the environment, considering the safety of drinking water, and upholding public confidence in water resources.

Several methods, such as advanced oxidation, electrical mineralization, chemical reduction, biological treatments method, adsorption, coagulation, and membrane separation are employed for the removal of organic pollutants from wastewater^{194–198}. Among them, adsorption is considered a highly efficient, straightforward, and economical approach for eliminating organic pollutants from contaminated water^{199–201}. Considering the chemical stability, diverse pore size distribution, enhanced surface area, and scalability, carbonaceous materials like graphene oxide, porous carbon, carbon nanotubes, and activated carbon have attracted significant attention for wastewater treatments^{176,202–206}. Therefore, there is a need to develop a novel carbon-based

adsorbent that exhibits enhanced adsorption capacity, faster adsorption rate, and specific surface reactivity.

In this study, we report a facile method for the preparation of ZnO and Carbon-based nanocomposites (ZnO@C) that can remove organic pollutants such as MO, MB, CR, and BPA from water. The ZnO@C nanocomposites were prepared in two steps, viz. heating the mixture of Zn (NO₃)₂·6H₂O and sucrose in an oven to form uniform foam followed by the carbonization of a foam in a tube furnace at 800 °C. Multiple ZnO@Carbon nanocomposites were prepared by following the same experimental procedure with varying the ratio of zinc nitrate salt and sucrose. The adsorption capacity of the nanocomposites towards BPA, MO, MB, and CR was studied under various adsorption parameters such as equilibration time, initial pollutants concentration, temperature, etc.

5.2. Materials and Methods

5.2.1. Materials

Sucrose (C₁₂H₂₂O₁₁ > 99.5%), Zinc nitrate hexahydrate [Zn (NO₃)₂·6H₂O ≥ 98%), and BPA (C₁₅H₁₆O₂ >97%), were purchased from Sigma Aldrich. CR (C₃₂H₂₂N₆Na₂O₆S₂ ≥35 %) was purchased from Alfa Aesar. MO (C₁₄H₁₄N₃NaO₃S > 98.0%) and MB (C₁₆H₁₈ClN₃S > 98%) were obtained from TCI America and Consolidated Chemical, respectively. An ultrasonic bath sonicator (VWR 50 T) was used to make the adsorption mixture uniform. A Fisher Scientific 11-600-49sh Isotemp Analog Hot Plate Stirrer was used for stirring the reaction mixture during the adsorption study. Syringe filters with 0.45 μm pore size were purchased from VWR and utilized to filter the reaction mixture for the UV–visible spectroscopic analysis. Milli-Q water (resistivity >18.20 MΩ.cm) was obtained from the Milli-Q water filter system, which was used as a source of deionized water in the experiment.

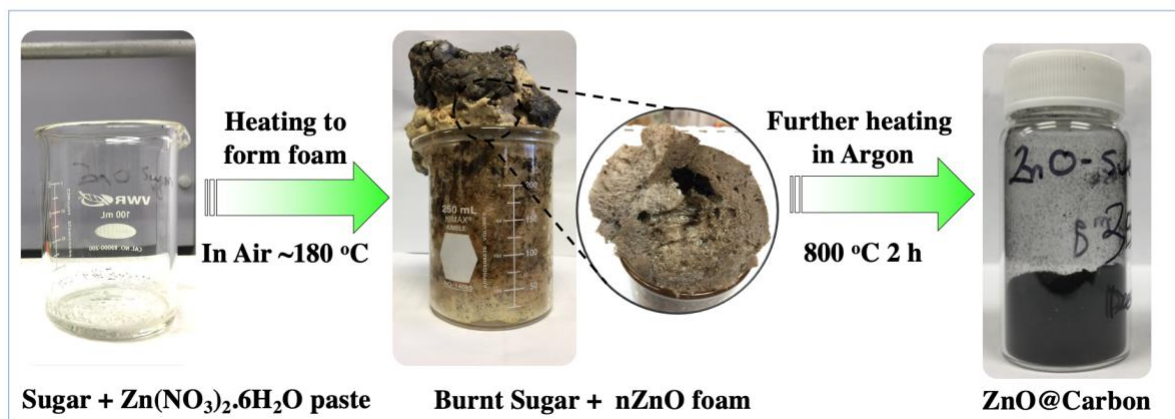
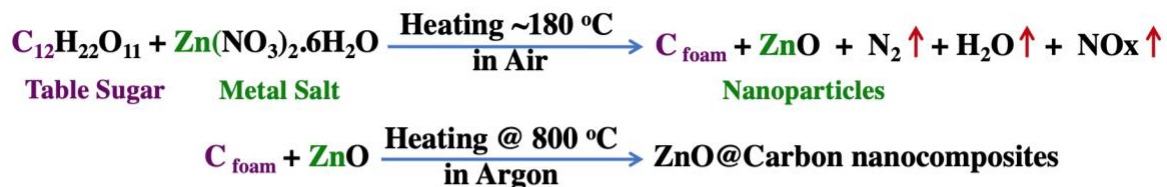
5.2.2. Characterization Techniques

The morphologies of the prepared ZnO@C nanocomposites were studied by Scanning Electron Microscopy (SEM), and Energy Dispersive X-ray spectroscopy (EDS) was utilized to obtain the quantitative and qualitative elemental composition of the as-synthesized nanocomposites. SEM images and EDS experiments, a JEOL JSM-IT100 microscope was used with the acceleration voltage of 10 and 30 kV, and carbon tape was used as the sample holder for both imaging and EDS analyses. Transmission electron microscopy (TEM) images were obtained by using a Hitachi H-7650 Microscope with an acceleration voltage of 80 kV. Bruker D8 Discover X-ray diffractometer equipped with Cu K α radiation was used to obtain the ZnO nanoparticle's X-ray diffraction (XRD) pattern. The X-ray photoelectron spectroscopy (XPS) analysis was performed in Thermo Scientific™ K-alpha™ equipment using a monochromatic Al Ka X-ray source. The survey spectra were obtained with 130-eV pass energy, while high-resolution analyses for specific core levels were performed at 20-eV pass energy. An argon ions flood gun was used to avert surface charging. All binding energies were corrected with reference to carbon 1s at 284.8 eV. UV-Visible spectrum was obtained by UV-Visible Spectrophotometer (Agilent Cary 50 Conc) using quartz cuvette and path length 10 mm.

5.2.3. Preparation of the ZnO@C Nanocomposite

Three different ZnO@C nanocomposite samples were synthesized following the same experimental procedure. The only difference was the variation in the mass ratio of the sucrose to zinc nitrate hexahydrate. In the entire synthesis procedure, the amount of Zn (NO₃)₂·6H₂O was kept constant while the amount of sucrose was varied. In the synthesis where 1 g sucrose was used, the ZnO@C nanocomposite sample was named ZnO@C-1. Likewise, where 2 g sucrose was used the sample was named ZnO@C-2, and where 4 g sucrose was used the sample was named

ZnO@C-4. As a representative, the synthesis of ZnO@C-2 is explained in detail. 2.0 g sucrose and 3.50 g Zn(NO₃)₂·6H₂O salt was mixed with 2 ml deionized water in a 250 ml glass beaker. Then the beaker was put on the preheated hot plate to dissolve the mixture. Afterward, the beaker was placed in the oven at 190 °C for 40 min to make foam and after 40 min, a blackish brown foam was obtained from the decomposition of zinc nitrate salt. Then the blackish brown foam was transferred from the beaker to a ceramic crucible which was used as a sample holder and placed in a tube furnace for heating at 800 °C for 2 hours in the presence of argon to synthesize the ZnO@C-2. The heating rate of 5 °C/min was used and natural cooling was used to cool the furnace. The amount of product obtained was about 815 mg, which was stored under ambient conditions for the characterization as well as adsorption studies. Likewise, two other nanocomposite (ZnO@C-1 and ZnO@C-4) samples were synthesized following the same experimental procedure which is shown in Scheme 5.1.



Scheme 5.1: Chemical reactions and pictorial scheme showing the steps involved in the preparation of ZnO@C nanocomposites.

5.2.4. Batch Adsorption Experiments

Stock solutions of MO (300 ppm), MB (300 ppm), and CR (300 ppm) were made by dissolving the reagents in deionized water. A stock solution of BPA (300 ppm) was prepared by dissolving the reagents in 2% methanol, followed by the addition of deionized water because BPA does not readily dissolve in DIW water. Then 50, 100, and 200 ppm concentration of each solution was prepared by diluting their respective stock solution (300 ppm). As a representative, the procedure for the batch adsorption experiment is explained using ZnO@C-2 nanocomposite. For the adsorption study, 10 mg of adsorbent (ZnO@C-2) was added to the 20 mL of adsorbate (BPA, MO, MB, and CR) solution in a glass vial and put in the bath sonicated for 30 min for proper mixing. Then the mixture was stirred for 24 hours on a magnetic stirring plate at 600 rpm. The temperature-dependent adsorption study was conducted using an oil bath, with the adsorption process performed at three different temperatures: 22°C, 52°C, and 70°C for 24 hours with stirring as well. After 24 hours, 1 mL of the sample was withdrawn and filtered through a syringe filter (0.45 µm pore size) for UV-vis analysis to obtain the adsorption capacity. The concentrations of MO, MB, CR, and BPA were analyzed using UV-vis spectroscopy, specifically by measuring the absorbance at its characteristic maximum wavelength of 464, 665, 498, and 276nm, respectively.

The adsorption capacity was determined by measuring the change in concentrations of the adsorbates from the beginning (initial concentration) to the end (final concentration) of the process. The equilibrium and percent adsorption capacity were calculated using the following equations, respectively.

$$\text{Equilibrium adsorption capacity, } Q_e = \frac{C_0 - C_e}{m} \times V \quad (1)$$

$$\text{Percent adsorption} = \frac{C_0 - C_t}{C_0} = \frac{A_0 - A_t}{A_0} \times 100\% \quad (2)$$

where Q_e represents the equilibrium adsorption capacities (mg/g) of adsorbent at a particular time t (min), C_0 , and C_t denotes the concentrations of pollutants (mg/L or ppm) at the beginning and at time t , respectively. A_0 and A_t represent the absorbance of the pollutants at concentrations C_0 and C_t , respectively. The specific details of the experimental conditions can be found in Table 5.1.

Table 5.1: Experimental parameters for the batch adsorption study of MO, MB, CR, and BPA.

Batch adsorption Study	Pollutant	Adsorbent (mg)	Volume (mL)	Conc. (ppm)	Time (hr.)
Conc. dependent	MO	10	20	50,100,200,300	24
Conc. dependent	MB	10	20	50,100, 200, 300	24
Conc. dependent	CR	10	20	50,100,200,300	24
Conc. dependent	BPA	10	20	50,100,200,300	24
Time dependent	MO	20	20	50	0-3
Time dependent	MB	20	20	50	0-3
Time dependent	CR	20	20	50	0-3
Time dependent	BPA	20	20	50	0-3
Temp. dependent	BPA	10	20	100	24

5. 3. Results and Discussions

5.3.1. SEM and EDX Spectrum of the ZnO@C Nanocomposite

The SEM analysis was conducted to obtain visual information about the surface morphology as well as the topography of the ZnO@C nanocomposite and EDX spectroscopy was employed to analyze the qualitative and quantitative composition of the synthesized nanocomposite. As a representative, the SEM image of ZnO@C-2 is shown in Figure 5.1a. From the SEM image, it was found that the morphology of the zinc oxide and carbon nanocomposite is

highly porous with a high surface area. This could be a reason for the high adsorptive capacity of the nanocomposite. The EDX spectra and the elemental mapping image of the zinc oxide and carbon nanocomposite are shown in Figure 5.1 (b-f). The EDX elemental mapping image has confirmed the presence of Zinc, oxygen, and Carbon which fits well with the results found from the EDX spectra of the nanocomposite which is shown in Figure 5.1.b.

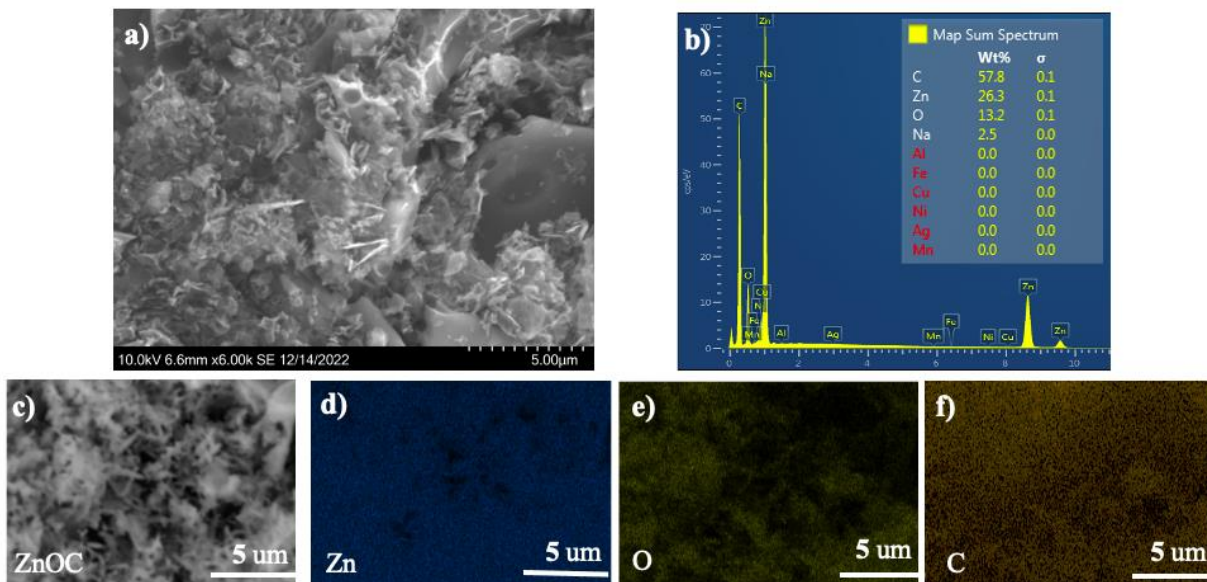


Figure 5.1: a) Typical SEM image of ZnO@C-2 b) EDX spectra of ZnO@C-2 showing the elemental composition, c) SEM backscattered electron image of ZnO@C-2 d) X-ray EDS mapping image of zinc, e) X-ray EDS mapping image of oxygen, and f) X-ray EDS mapping image of carbon.

5.3.2. TEM image of the ZnO@C Nanocomposite

The morphology and crystal structure of ZnO and carbon nanocomposite (ZnO@C-2) were obtained using transmission electron microscopy (TEM) in both dark field and bright field imaging models at different positions of the samples in Figure 5.2. From the TEM images, the presence and distribution of ZnO nanoparticles within the carbon matrix was visualized which is indicated in Figure 5.2. In the dark field images (Figure 5.2.a and c), the nanocomposite exhibited bright, well-dispersed nanoparticles against a dark background, indicating their distinct scattering properties.

This observation suggested that the ZnO nanoparticles were effectively incorporated within the carbon matrix, forming a composite structure. Conversely, the bright field images (Figure 5.2.b and d) provided further insights into the nanocomposite's morphology and internal structure. They showed interconnected two-dimensional carbon nanosheets with embedded ZnO nanoparticles. The nanosheets displayed a layered structure, while the ZnO nanoparticles appeared as dark spots within the carbon matrix, confirming successful integration. The TEM analysis in both dark field and bright field modes indicated that the ZnO and carbon nanocomposites exhibited high porosity and surface area, which likely contributed to their strong adsorptive properties. Furthermore, this characterization not only confirmed the formation of the ZnO and carbon nanocomposite but also provided valuable information about its morphology and internal arrangement. Such insights are crucial for understanding the structural properties and potential applications of the nanocomposite, particularly in the context of adsorption studies as discussed in this report.

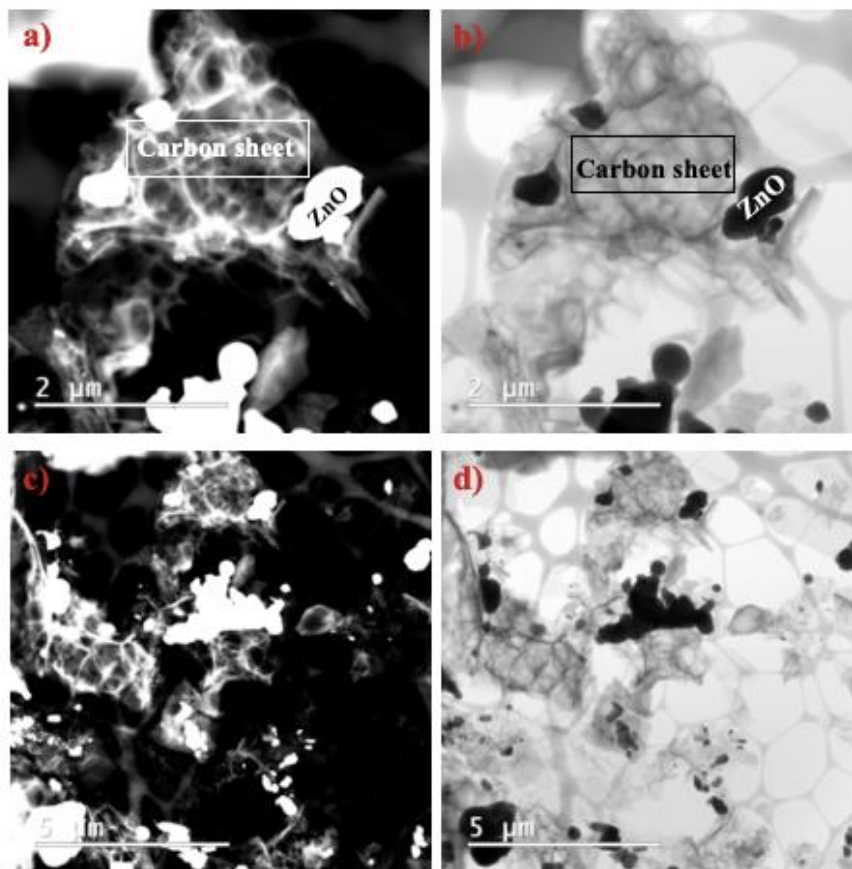


Figure 5.2: a) and c) are the dark field image, b) and d) are the bright field image at two different sites of ZnO@C-2, respectively.

5.3.3. XRD of the ZnO@C Nanocomposite

The significance of X-ray diffraction (XRD) in analyzing ZnO and carbon nanocomposites lies in its ability to identify crystal structure, phase composition, and nanoscale characteristics. This technique plays a crucial role in optimizing synthesis methods and gaining valuable information about material properties, ultimately facilitating their application across various fields.

The XRD pattern of ZnO in Figure 5.3 reveals distinctive diffraction peaks observed at specific 2θ angles of approximately 31.7° , 34.4° , 36.2° , 47.5° , 56.5° , 62.8° , 66.3° , 67.9° , 69.0° , 72.6° , and 77.2° correspond to the crystallographic planes (100), (002), (101), (102), (110), (103),

(200), (112), (201), (004), and (202) of the hexagonal wurtzite structure in ZnO indicating the presence of highly crystalline ZnO nanoparticles^{200,207–209}.

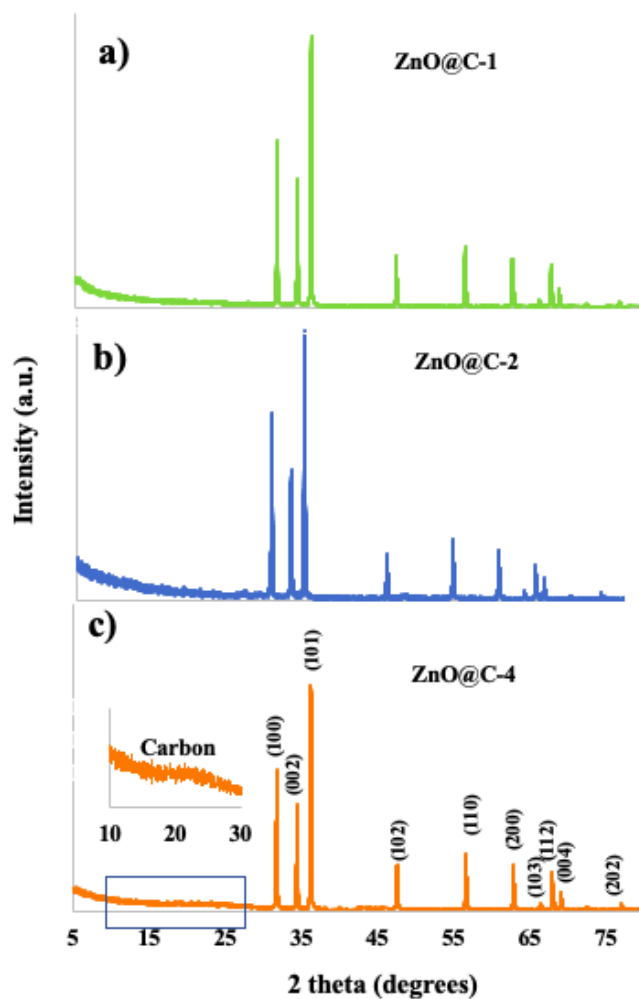


Figure 5.3: XRD pattern of ZnO@C nanocomposite.

On the other hand, the XRD pattern of the carbon nanocomposite displays broad and diffuse peaks, suggesting an amorphous or nanocrystalline structure. Amorphous carbon lacks well-defined crystallographic planes, leading to a broad peak centered around 25-30 degrees in the XRD pattern. This peak signifies the presence of disordered carbon, where the atoms lack long-range order.

5.3.4. XPS of the ZnO@C-2 Nanocomposite

The purity of the ZnO@C-2 nanocomposite, chemical states of the synthesized product, and elemental composition were obtained by the XPS analysis. It was found from the XPS survey spectrum that the ZnO@C-2 consists of Zn, C, N, and O in the sample which is shown in Figure 5.4.a Quantitative analysis was performed using high-resolution spectra of specific core levels of the different elements. Table 5.2 presents a summary of the XPS-determined composition for the sample.

Table 5.2: Atomic % of elements calculated through XPS and key molar ratios.

Sam ple	Atomic %								Molar ratios		
	C			Zn	O		N		O/Zn	O/N	N/Zn
	a	b	c		a ^{&}	b	a	b			
ZnO @C C-2	56.0	17.3	12.3	2.9	2.0	5.5	0.5	3.5	2.54	1.87	1.36

[&] two overlapped O1s signals are considered as one in peak O a.

After quantification, it may be observed that excess oxygen is detected in the sample. The substrate was obtained by pyrolysis of sucrose and zinc nitrate hexahydrate. This result suggests that some oxygen may be present in the carbon structure after treatment or different Zn-based compounds could have been formed: Zn (OH)₂, ZnCO₃, ZnO. Furthermore, nitrogen is present in two different electronic states which could be nitrates, nitrides, or amine groups in either the carbon substrate or Zn compounds.

Binding energy determinations are summarized in Table 5.3. The spin-orbit doublets for Zn are also included, showing the expected energy difference of *c.a.* 23 eV between 2p_{3/2} and 2p_{1/2}.

Table 5.3: Binding energy of the sample.

Sample	Binding Energy (eV)								
	C 1s			Zn 2p		O 1s		N 1s	
	a	b	c	2p _{3/2}	2p _{1/2}	a	b	a	b
ZnO@C-2	284.80	285.78	287.62	1022.55	1045.60	531.31	532.68	398.59	400.63

The binding energies observed in carbon 1s correspond to a = aliphatic carbon at 284.8 eV fixed for charge correction of all samples, b = carbon bonded to oxygen (C-O-C) at *c.a.* 286 eV, c = does not correspond to identifiable species since it is slightly lower than the values that could be expected in a carbonate (usually above 288 eV). This last signal could be associated with the tailing of the main carbon signal as observed in SP² C containing materials like graphene or carbon nanotubes, considering that a sheet-like structure is observed in the sample. Figure 5.4 shows all core-level high-resolution spectra of the different elements present in the sample.

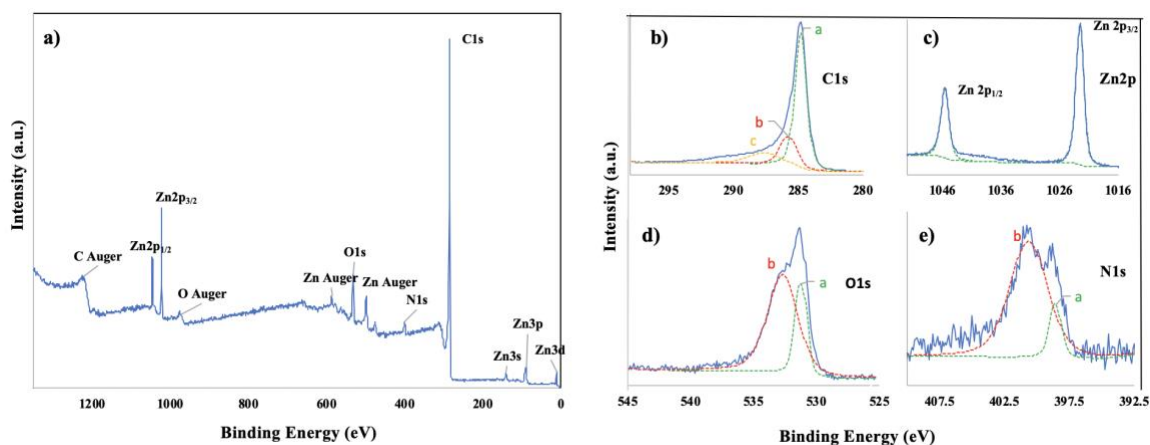


Figure 5.4: XPS High-resolution spectra for core levels of a) XPS survey of 2gZnOC. b) C 1s, c) Zn 2p, d) O 1s and e) N 1s, along with deconvolution peaks.

Zn 2p_{3/2} binding energy is above the range that corresponds to typical ZnO values. The observed 1022.5 eV value could be associated with either zinc carbonate or zinc hydroxide. Only one Zn peak could be observed, which suggests that all Zn is in the same state, considering the synthesis procedure and signal c of C 1s, it is likely that zinc carbonate was formed and is present

in the samples surface. Oxygen 1s binding energy around 531.5 eV may be related to organic C-O bonds or has been associated with Zn-OH while O1s BE around 532.6 eV has been assigned to carboxyl (COO⁻) groups bound to Zn²⁺. Samples were pyrolyzed at 800 °C using sucrose as a carbon source, considering the large amount of oxygen contained in sucrose signal O 1s a is proposed to proceed from C-O organic bonds that were not eliminated after treatment. Surface zinc carbonate or zinc bound to surface carboxyl groups correspond adequately to the BEs observed in peaks: Zn 2p_{2/3}, C 1s c, and O 1s b. Two clearly defined peaks of nitrogen were observed, nitrates would show at far higher binding energy of 407 eV, while metallic nitrides appear at about 397 eV²¹¹. It is not possible to determine the nature of the observed nitrogen; amine groups would show BEs in the observed range but are unlikely to be present after treatment at 800 °C.

5.3.5. Adsorption Capacity of ZnO@C-2 for MO, MB, CR, and BPA

The adsorption capacity of the ZnO@C-2 composite for MO, MB, CR, and BPA was determined using equation 1, as depicted in Figure 5.5. As ZnO@C-2 nanocomposite performed best from the three adsorbents synthesized in this study, the result of this nanocomposite is shown in the figure. The results indicated that the equilibrium adsorption capacity (Q_e) for all target pollutants increased with higher initial concentrations. The increase in initial concentration provides a greater concentration gradient, facilitating a higher adsorption capacity. This observation can be attributed to the stronger driving forces that overcome mass transfer resistances, allowing for more adsorbate molecules to transfer from the aqueous phase to the solid phase. These interactions result in the accumulation of pollutant molecules on the composite surface, leading to an increased adsorption capacity.

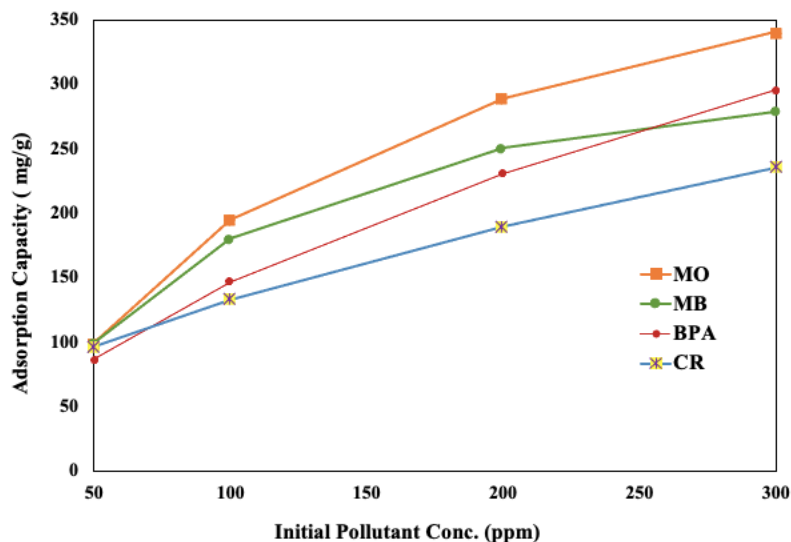


Figure 5.5: Adsorption capacity of ZnO@C-2 composite for MO, MB, CR, and BPA at different initial concentrations.

The Q_e was calculated to be about 340 mg/g, 279 mg/g, 236 mg/g, and 296 mg/g at an initial MO, MB, CR, and BPA concentration of 300 ppm respectively. Additionally, the percent adsorption of the pollutants was calculated by using equation 2 and it was found that the adsorption percentage decreased with the increase in initial MO, MB, CR, and BPA concentration. About 57 %, 47%, 40%, and 95% of the MO, MB, CR, and BPA, respectively were adsorbed at an initial concentration of 300 ppm.

5.3.6. Adsorption Isotherms (Langmuir and Freundlich) Model

The adsorption isotherm illustrates the relationship between the amount of dye adsorbed onto a specific amount of adsorbent and the concentration of dyes at a constant temperature. In this study, we employed two widely used adsorption isotherms, namely the Langmuir and Freundlich isotherms, to gain insights into the adsorption mechanism of MO, MB, CR, and BPA on the ZnO@C-2 composite. The Langmuir adsorption isotherm model is based on the concept of

monolayer adsorption, where the adsorbate molecules form a single layer on the surface of the adsorbent.

The linear form of the Langmuir adsorption isotherm model is expressed by the following equation.

$$\frac{C_e}{Q_e} = \frac{1}{Q_m} C_e + \frac{1}{K_L Q_m} \quad (3)$$

In the adsorption process, C_e represents the equilibrium concentrations of the dyes in milligrams per liter (mg/L), while Q_e and Q_m represent the equilibrium and maximum dye adsorption capacity in milligrams per gram (mg/g) by the adsorbent, respectively. The Langmuir constant, K_L , which is expressed in liters per milligram (L/mg), is a measure of the binding sites' affinity for the dyes.

Freundlich adsorption isotherm model a widely used model used in adsorption study field and it holds the adsorption process by considering the both the mono and multi-layer on the adsorptions of adsorbate on the adsorbent. The linear form of the Freundlich isotherm model is described as follows.

$$\ln Q_e = \frac{1}{n} \ln C_e + \ln K_F \quad (4)$$

where C_e represents the equilibrium concentrations of the dyes in milligrams per liter (mg/L), while Q_e represents the equilibrium dye adsorption capacity in milligrams per gram (mg/g) by the adsorbent, respectively and K_F and n are constants for a given adsorbate and adsorbent at a particular temperature.

The experimental data was analyzed using the linear forms of the Langmuir and Freundlich isotherm models, using Equation 3 and Equation 4, respectively. The results of this analysis are depicted in Figure 5.6.

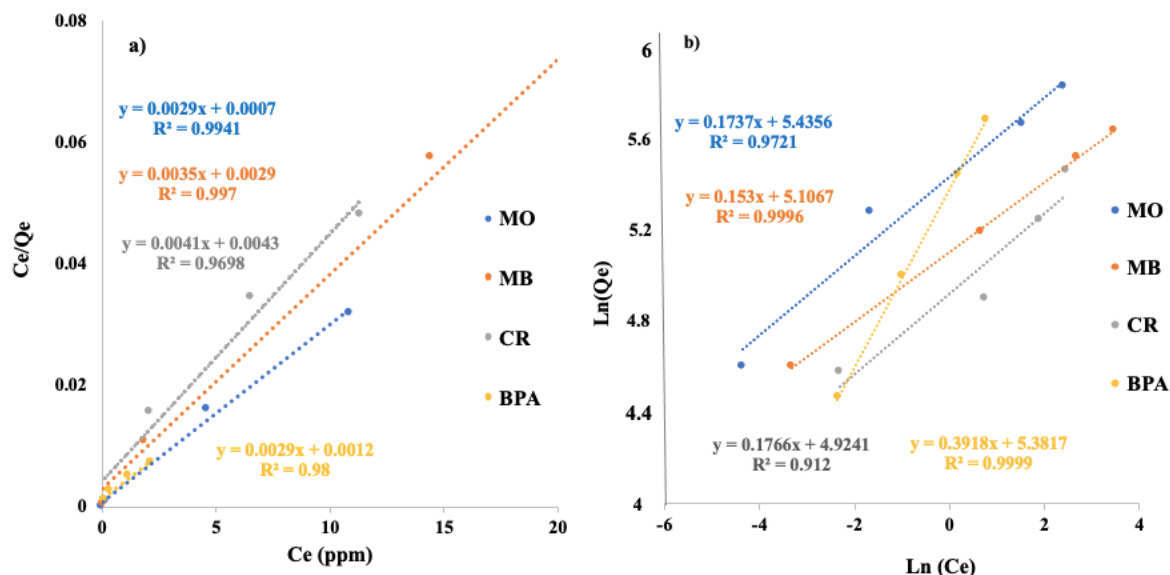


Figure 5.6: The linear form of the a) Langmuir and b) Freundlich adsorption isotherms for the adsorption of MO, MB, CR, and BPA by ZnO@C-2 composite, respectively.

From Figure 5.6.a, it was found that the relationship between the experimental data and the Langmuir model isotherm with coefficient (R^2) values indicates that the adsorption of MO, MB, CR, and BPA supported the occurrence of a monolayer adsorption mechanism. Using the Langmuir isotherm equation, the maximum adsorption capacity (Q_m) was determined to be 385, 286, 244, and 385 mg/g, for MO, MB, CR, and BPA, respectively. Figure 5.6.b represents the Freundlich isotherm, and it was observed that the coefficient (R^2) values of all the pollutants are not as good as the Langmuir isotherm model as some of the coefficient (R^2) values are far from 1. From the figure, it could be concluded that is clear that the Langmuir isotherm model fits the experimental data best compared to Freundlich isotherm models since it has higher determination coefficient (R^2) values toward the removal of MO, MB, CR, and BPA as shown in Figure 5.6.

5.3.7. Adsorption Kinetics

The adsorption kinetics were assessed using two commonly employed models: pseudo-first-order and pseudo-second-order models. The linear representation of the pseudo-first-order model is given by the following equation.

$$\log(Q_e - Q_t) = \log Q_e - \frac{K_1 t}{2.303} \quad (5)$$

The linear form of the pseudo-second-order model is given by the following equation.

$$\frac{t}{Q_t} = \frac{t}{Q_e} + \frac{1}{K_2 Q_e} \quad (6)$$

In the equations, Q_e and Q_t represent the adsorption capacities (mg/g) at equilibrium and at a specific time point t (min). The rate constants for the pseudo-first-order and pseudo-second-order kinetic models are denoted as K_1 (1/min) and K_2 [g/ (mg min)], respectively.

The time-dependent adsorption behavior of MO, MB, CR, and BPA by the ZnO@C-2 composite is depicted in Figure 5.7.a. The results demonstrated the rapid adsorption capability of the ZnO@C-2 composite, where CR achieved complete adsorption within 60 minutes, with approximately 99% of MB being adsorbed within 60 minutes. Similarly, BPA required 180 minutes to achieve 90% adsorption while MO reached 78% adsorption after 180 minutes. It is evident that the ZnO@C-2 composite exhibited excellent and efficient removal of MB and CR from solutions with initial concentrations of 50 ppm within 60 min than the MO and BPA.

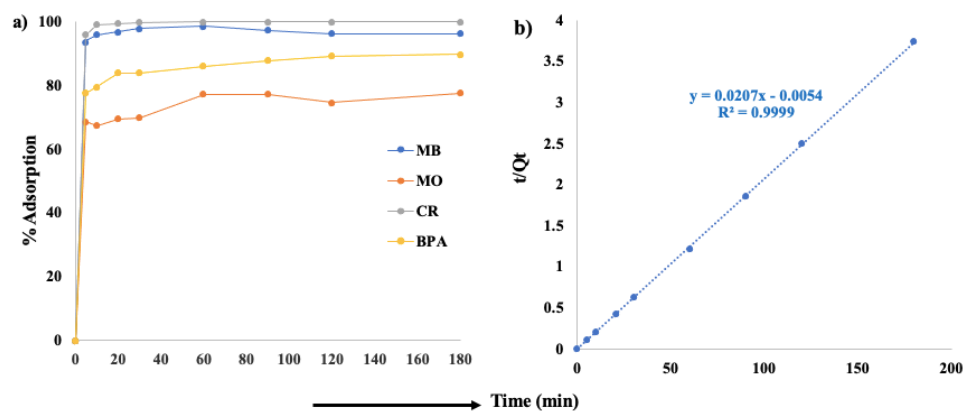
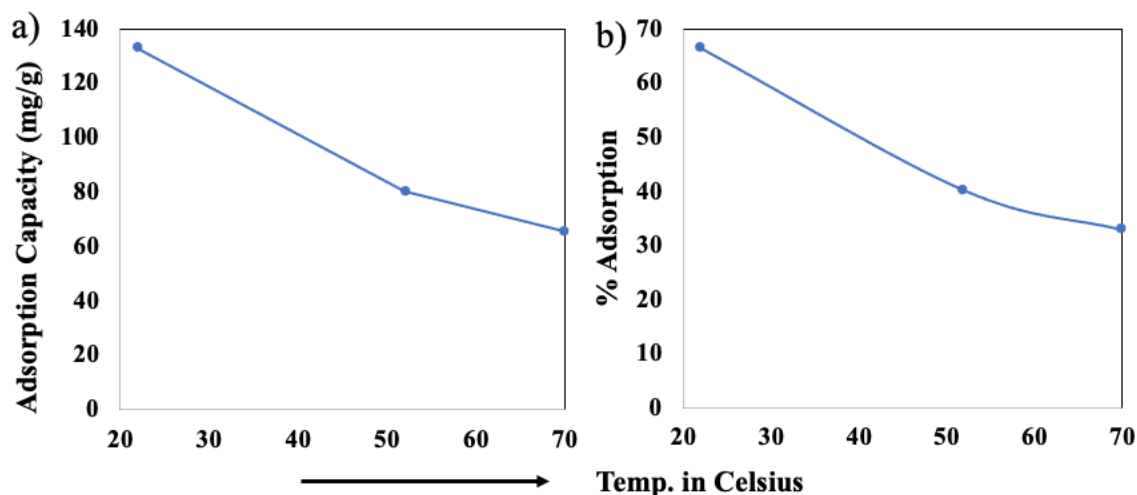


Figure 5.7: a) Time-dependent percent adsorption of MO, MB, CR, and BPA by ZnO@C-2 composite, (Initial concentration = 50 ppm, $V = 20$ mL and adsorbent = 20 mg) and (b) the corresponding pseudo-second-order kinetics adsorption.

The kinetics of adsorption for all the pollutants (MO, MB, CR, and BPA) were studied using both the pseudo-first-order and pseudo-second-order kinetic models. Figure 5.7.b demonstrates the linear correlation observed when applying the Pseudo-second-order kinetic model using equation 6 suggesting that the adsorption of all the pollutants adhered to this model.

5.3.8. Adsorption Thermodynamics

To observe the impact of temperature on the adsorption of BPA using ZnO@C-2, experiments were conducted at three different temperatures: 22°C, 52°C, and 70°C. The adsorption capacities of BPA, as illustrated in Figure 5.8.a, revealed a clear trend of decreasing adsorption capacity with increasing temperature. This observation suggests that the adsorption process is exothermic in nature. Figure 5.8.b shows the percentage of BPA adsorption with different temperatures, and it was found that with temperature increase decreases the percent removal of pollutants. It is concluded from the figure that the adsorption capacity and pollutant removal percentage decrease with increasing temperature showing that the adsorption process is suitable and favorable at low temperatures.



5.8: Temperature-dependent a) adsorption capacity b) percent adsorption of BPA by ZnO@C-2 composite, (Initial concentration = 100 ppm, V = 20 mL and adsorbent = 10 mg).

5.4. Regeneration Study of ZnO@C-2 Nanocomposite

Regeneration studies have become essential in evaluating the recyclability of adsorbents for practical applications, driven by the increasing emphasis on sustainability from economic and ecological perspectives. The ability of adsorbents to be effectively rejuvenated and reused is crucial to meet these demands. Through these studies, we gain insights into the potential for adsorbents to be regenerated, leading to reduced waste generation and improved resource utilization. By exploring the feasibility of recycling adsorbents, it could be actively contributed to sustainability principles and address the urgent need for economic viability across diverse industries. Such research paves the way for innovative and environmentally friendly approaches that align with our goal of a sustainable future.

Various ways of regeneration capability ZnO@C-2 for the adsorption of MO dye are illustrated in Figure 5.9. Figure 5.9.a presents the adsorption study of MO using the ZnO@C-2 nanocomposite, also referred to as the control. In this experiment, 200 mg of ZnO@C-2 was combined with 80 mL of 500 ppm MO and subjected to 30 minutes of bath sonication to ensure

proper mixing. The mixture was then stirred for 24 hours at 600 rpm on a magnetic stirring plate. After this duration, 1 mL of the sample was withdrawn and passed through a syringe filter (0.45 μm pore size) for UV-vis analysis, enabling the determination of the percentage of pollutant (MO) removal. This step is known as the 0 regeneration or first cycle of the adsorption study, and it demonstrated that the ZnO@C-2 adsorbent achieved 100 percent removal of the MO dye. The remaining filtrate and residue were subjected to vacuum filtration. The solid residue collected was dried and reserved for the next cycle or first regeneration. In the first regeneration, the collected residue was measured, and the required amount of 500 ppm MO was added. The mixture was sonicated for 30 minutes and left for 24 hours for adsorption before being filtered for UV-vis analysis. The same procedure was repeated for the second and third regenerations. The results revealed 100 percent removal of MO in the 0-regeneration cycle, about 18 percent in the first regeneration, about 17 percent in the second regeneration, and about 15 percent in the third regeneration.

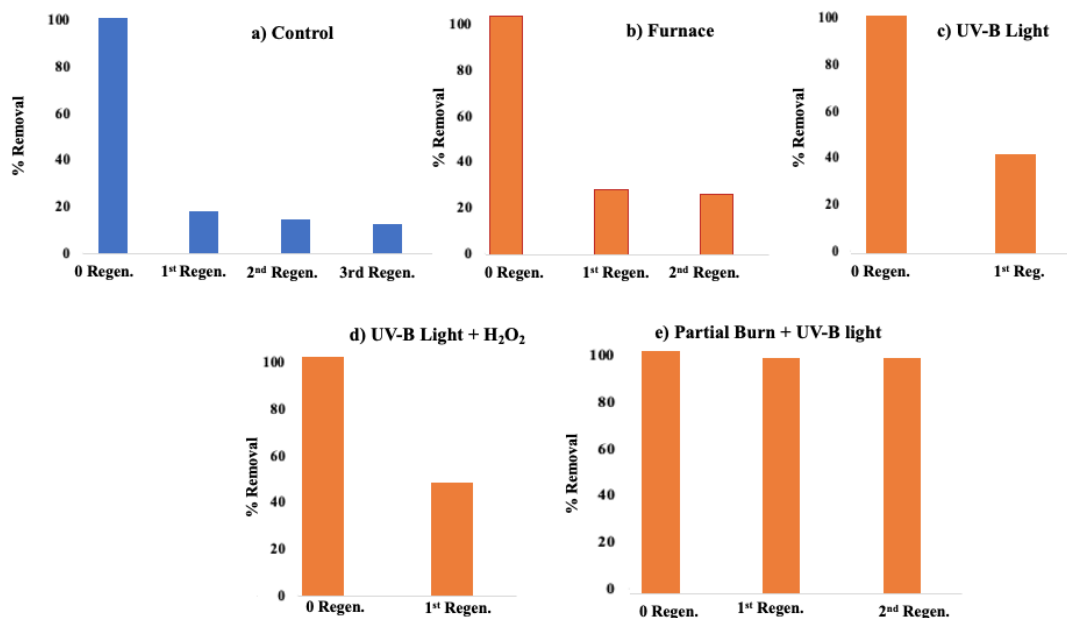


Figure 5.9: Regeneration of ZnO@C-2 for the adsorption of MO dye.

Based on the results obtained, it can be concluded that the method employed for regenerating the adsorbent was not effective. The study revealed a significant decrease in the percentage removal of MO dye with each successive regeneration cycle. While the initial regeneration cycle demonstrated complete removal of the pollutant (100 percent), subsequent regenerations showed a noticeable decline in performance, with only 18 percent removal in the first regeneration, followed by 17 percent in the second and 15 percent in the third. These findings indicate that the chosen regeneration procedure was not suitable for maintaining the adsorbent's optimal performance over multiple cycles. Further research and alternative regeneration approaches are necessary to ensure sustained and efficient adsorption performance of the ZnO@C-2 nanocomposite.

Therefore, we tried four different ways to regenerate the adsorbent for obtaining successive adsorptions. The first attempt for regeneration of ZnO@C-2 adsorbent is shown in Figure 5.9.b which is named furnace. In this experiment, 200 mg of ZnO@C-2 was mixed with 80 mL of 500 ppm MO and sonicated for 30 minutes. After 24 hours of stirring, the sample was filtered and analyzed, revealing 100 percent removal of the MO dye. This initial step is referred to as the 0 regeneration. After filtration, the solid residue was dried and carbonized in a ceramic crucible at 500°C for 30 minutes in the presence of argon gas in the furnace. The aim was to burn off adsorbed MO dye from the adsorbent, potentially enabling its regeneration. The carbonization process involved subjecting the residue to high temperatures, causing thermal decomposition of the organic compounds (MO) dye. Chemical bonds within the MO dye molecules are broken, resulting in the release of gaseous byproducts such as carbon dioxide, water vapor, and volatile organic compounds. After carbonization collected the sample and the required amount of 500 ppm MO solution were added to run the adsorption study for the first regeneration and it was found that it

removed only 27 percent of MO in the first regeneration cycle. Following the same procedure, it was carried out the experiment for the second regeneration and it was found the MO removal was about 25 percent. The hypothesis was this carbonization treatment will effectively burn MO dye, restoring the adsorbent's adsorption capacity and making it potentially suitable for subsequent cycles of adsorption but the results did not come out like that as after carbonization the nanocomposites lost their high surface area, and it was sand like appearance and thereby lost its adsorption capability.

Figure 5.9.c, referred to as UV-B light, illustrates the second attempt at regenerating the adsorbent. In this case, after 0 regeneration it was collected the solid residue after the filtration process and taken in a 100 mL beaker. Added an adequate amount of water to it and put them under the UV-B light (360 nm) inside a UV reactor for 72 hours to degrade the MO (which was adsorbed during the 0 regeneration) from the ZnO@C-2 nanocomposite. From Figure 5.5.c, it is evident that the first regeneration cycle resulted in only 41 percent removal of the MO dye. This limited regeneration efficiency can be attributed to the inability of UV light to adequately reach and interact with the MO dye molecules for photodegradation, thus hindering complete regeneration. In the presence of UV-B light, the MO dye molecules absorb photons with sufficient energy to initiate a photochemical degradation process. This absorption leads to the breaking of chemical bonds within the dye molecules, resulting in the formation of highly reactive species like free radicals. These reactive species react with the dye, causing its degradation into smaller, less complex molecules. However, in the first regeneration cycle, the UV light may have struggled to effectively penetrate the adsorbent and reach all the adsorbed MO dye molecules. The insufficient contact between UV light and the MO dye molecules prevents complete photodegradation and hampers the regeneration process. Therefore, the observed limited removal of the dye in the first

regeneration cycle suggests the need for optimization in the setup to ensure better contact between UV light and the adsorbed MO dye, enabling more efficient photodegradation and subsequent regeneration of the adsorbent.

Figure 5.9.d, labeled as UV-B light+H₂O₂, represents the third attempt at regenerating the adsorbent. In this case, the solid residue obtained after the 0-regeneration cycle was collected and placed in a 100 mL beaker. An appropriate amount of water and hydrogen peroxide (30 mg solid residue + 12 mL 500 ppm MO + 10 mL DIW + 3 mL hydrogen peroxide) were added to the beaker. The mixture was then exposed to UV-B light with a wavelength of 360 nm inside a UV reactor for 16 hours. The aim was to degrade the MO dye, which had been adsorbed during the 0-regeneration cycle, from the ZnO@C-2 nanocomposite. In this regeneration approach, the combination of UV-B light and hydrogen peroxide acts synergistically to enhance the degradation of the MO dye. When exposed to UV-B light, the absorbed photons provide energy for the photochemical degradation process, breaking the chemical bonds within the dye molecules. Meanwhile, hydrogen peroxide, as an oxidizing agent, reacts with the dye molecules and generates hydroxyl radicals (\bullet OH), which are highly reactive species. These hydroxyl radicals further contribute to the degradation of the MO dye by reacting with and breaking down the dye molecules into simpler compounds. The extended exposure of the solid residue to UV-B light in the presence of hydrogen peroxide enables the efficient degradation of the adsorbed MO dye on the ZnO@C-2 nanocomposite. However, it is noteworthy that the first regeneration cycle achieved only 48 percent removal of the MO dye, suggesting the need for further optimization to enhance the regeneration efficiency.

Figure 5.9.e, labeled as partial burn + UV-B light, represents the final attempt in the regeneration process of the adsorbent. In this experiment, 200 mg of fresh ZnO@C-2 adsorbent

was subjected to partial burning of carbon by placing it on a preheated hotplate at 500°C for two hours, with occasional stirring. This process aimed to increase the concentration of ZnO nanoparticles by reducing carbon content, thereby enabling better contact between UV light and the adsorbent for enhanced MO degradation. During the regeneration process, 50 mg of partially burnt ZnO@C-2 was mixed with 20 mL of 500 ppm MO and subjected to 30 minutes of bath sonication for thorough mixing. The mixture was then stirred for 24 hours, followed by a withdrawal of 1 mL for UV-vis analysis to determine the percentage of MO removal. This step, known as the 0 regeneration, demonstrated that the ZnO@C-2 adsorbent achieved 100 percent removal of the MO dye. The remaining mixture of filtrate and residue underwent vacuum filtration, and the collected solid residue was dried and reserved for the next cycle or first regeneration. For the first regeneration, the solid residue was combined with an adequate amount of water in a 100 mL beaker and exposed to UV-B light (360 nm) inside a UV reactor for 16 hours. This step aimed to degrade the MO dye adsorbed during the 0 regeneration from the ZnO@C-2 nanocomposite. From the results depicted in Figure 5.5.e, it is evident that the first regeneration cycle achieved nearly 100 percent removal of the MO dye. The partial burning of carbon facilitated the exposure of more ZnO nanoparticles, enhancing their interaction with MO in the presence of UV light. This favorable combination led to complete regeneration in the first cycle. The same procedure was repeated for the second regeneration, yielding similar results as the second regeneration. Based on these findings, it can be concluded that the regeneration study was successful in achieving efficient removal of the MO dye using the partial burn + UV-B light approach.

5.5. Quantification of the Percentage of Carbon and ZnO from ZnO@C Nanocomposite

Three different sample holder containing 200 mg of the as-synthesized ZnO@C-1, ZnO@C-2, and ZnO@C-4 nanocomposites were subjected to carbonization. The carbonization

process facilitated to extraction of ZnO nanoparticles from the ZnO and carbon nanocomposite (ZnO@C) through the removal of the carbon component. This process involved heating the ZnO@C samples at a ramp rate of 2 °C/min in the presence of air at a temperature of 600 °C for a duration of 2 hours in a tube furnace. During this process, the carbon component of the nanocomposites was combusted away, leading to the removal of carbon, and leaving behind only the ZnO nanoparticles. The ZnO samples obtained from ZnO@C-1, ZnO@C-2, and ZnO@C-4 nanocomposite was labeled as ZnO@-1, ZnO@-2, and ZnO@-4, respectively. The table 5.4 below summarizes the amount of carbon combusted and the remaining amount of ZnO after the carbonization process, based on the initial 200 mg of each sample:

Table 5.4: Percentage of the carbon combustion and the remaining ZnO content after the carbonization process.

Sample	Initial weight (Before carbonization)	% of C combusted (After Carbonization)	% of remaining ZnO (After Carbonization)
ZnO@C-1	200 mg	5.64	94.36 (ZnO@-1)
ZnO@C-2	200 mg	31.24	68.76 (ZnO@-2)
ZnO@C-4	200 mg	61.50	38.50 (ZnO@-2)

After the carbonization process, the obtained amount of ZnO nanoparticles was utilized to assess their performance in the photodegradation of methyl orange (MO) under UV-B light irradiation in deionized water (DIW).

5.6. Photodegradation Of MO using ZnO Derived from ZnO@C

The purpose of this experiment was to evaluate the photodegradation capabilities of the ZnO nanoparticles obtained from the ZnO@C nanocomposite. By subjecting the ZnO

nanoparticles to UV-B light, their ability to initiate the degradation of MO in the aqueous solution could be observed. The photodegradation process involved the exposure of the MO solution containing the ZnO nanoparticles to UV-B light, followed by monitoring the degradation progress over a specific period which is shown in Figure 5.10.

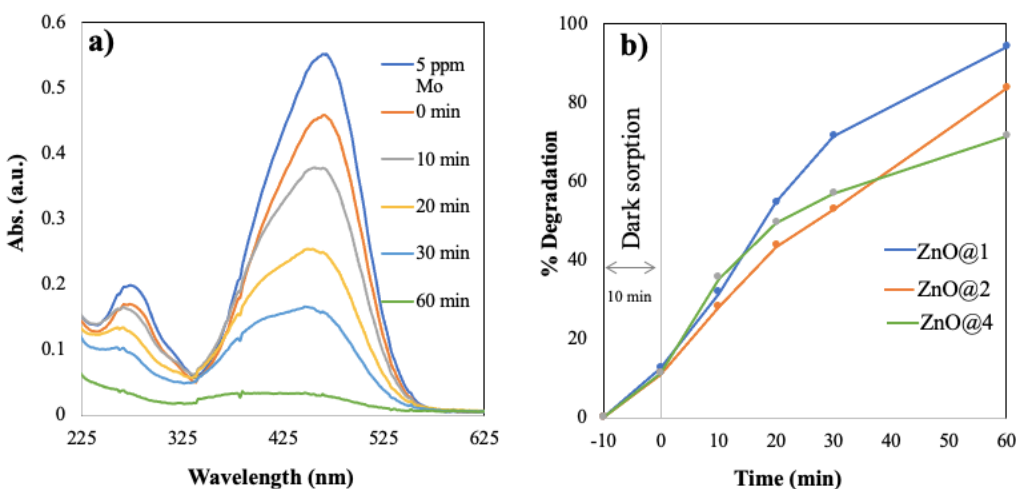


Figure 5.10: a) The UV-vis spectra of the 5 ppm MO solution by ZnO@1 were recorded at different time intervals during the photocatalytic degradation process, b) time-dependent percent degradation of MO by solution by ZnO@1, ZnO@2, and ZnO@4.

For the photodegradation experiments, 30 mg of ZnO@1 was evenly dispersed in 30 mL of 5 ppm MO solution through a 10-minute bath sonication process and the experiment was conducted in the absence of light. The purpose of bath sonication was to ensure the uniform dispersion of the ZnO@1 nanoparticle and to establish an adsorption-desorption equilibrium between the nanoparticles and the dye molecules. The resulting mixture was subjected to UV illumination within a box reactor while being continuously stirred. At regular intervals of 10, 20, 30, and 60 minutes, about 1 mL of the sample was drawn and filtered using a syringe filter to prepare it for UV-vis spectroscopic analysis. The percent degradation of the dyes was determined by measuring the absorbance at their characteristic absorption maxima, which was 464 nm for the

MO solution. The Figure 5.10. a, it was found that the photodegradation performance of ZnO@1 resulted in the almost complete degradation of the 5 ppm MO dye under UB-B light irradiation. In Figure 5.10.b, the percentage of degradation for ZnO@1, ZnO@2, and ZnO@4 is depicted, demonstrating their respective degradation efficiencies. It was observed that ZnO@1 achieved the highest degradation rate, reaching approximately 95 percent degradation of MO within 60 minutes. ZnO@2 exhibited a degradation rate of 83 percent, while ZnO@4 showed a degradation rate of 71 percent within the same timeframe. This variation in performance could be attributed to the composition of the nanocomposites. ZnO@C-1, which contained a higher concentration of Zn source and a lower amount of carbon source, resulted in a larger amount of ZnO@1 after the carbonization process, leading to its superior photocatalytic activity. This investigation aimed to gain insights into the photocatalytic performance of the ZnO nanoparticles derived from the ZnO and carbon nanocomposite. By studying their efficiency in degrading MO under UV-B light illumination, the potential application of these ZnO nanoparticles as effective photocatalysts for the removal of organic pollutants could be assessed. The results obtained from this study would contribute to our understanding of the photocatalytic properties of ZnO and their potential use in water treatment and environmental remediation.

5.7. Conclusion

This study focused on the investigation of the adsorption capacity of a ZnO and carbon (ZnO@C-2) nanocomposite for the removal of various model pollutants such as MO, MB, CR, and BPA. The findings demonstrated remarkable adsorption efficiency of the ZnO@C nanocomposite towards all the targeted pollutants. The batch adsorption studies were carried out by different experimental parameters including the initial concentration of pollutants and contact time and temperature. The maximum adsorption capacities of MO, MB, CR, and BPA were found

to be 345, 285, 245 and 345 mg/g, respectively. The surface area and porous structure of ZnO@C facilitated the availability of active sites for pollutant adsorption and thereby enhanced the adsorption performance. The adsorption process followed pseudo-second-order kinetics, indicating the involvement of chemical interactions. Moreover, the adsorption isotherms adhered to the Langmuir isotherm model suggesting monolayer adsorption mechanisms. Furthermore, the nanocomposite showed excellent recyclability with multiple adsorption-regeneration cycles maintaining consistent performance. In conclusion, the ZnO and carbon nanocomposite demonstrated great potential as an effective adsorbent for the removal of MO, MB, CR, and BPA, highlighting its significance in applications such as water purification and environmental remediation.

Chapter 6: Conclusion and Future Directions

In conclusion, this dissertation has made substantial contributions to the field by focusing on the synthesis of ZnO nanoparticles and a regenerable adsorbent, the ZnO@C nanocomposite by combustion method, with the aim of exploring their potential in two important applications: photocatalytic degradation of MO under UV-B light and sunlight irradiation, and adsorptive removal of various pollutants such as MO, MB, CR, and BPA. The photocatalytic degradation of MO was influenced by various factors such as initial concentration of MO, catalyst dosage, and irradiation intensity. The results revealed that ZnO nanoparticles effectively generated ROS, such as hydroxyl radicals ($\bullet\text{OH}$) and superoxide radicals during the irradiation process. These ROS played a crucial role in the degradation of MO by initiating oxidative reactions and breaking down the dye molecules. The photocatalytic process followed pseudo-first-order kinetics, indicating the involvement of the degradation steps. Overall, the results highlight the potential of ZnO nanoparticles as an effective and environmentally friendly approach for the degradation of MO in both UV light and sunlight conditions, with implications for the treatment of dye-contaminated wastewater. The outcomes of the research mentioned above, particularly the innovative synthesis approaches of ZnO have the potential to stimulate future investigations in synthesizing a wide range of metallic nanoparticles, mixed metallic nanoparticles, their metal oxides, and composites. Furthermore, the nanomaterials developed in this report have potential applications in diverse areas including electrocatalysis, solar harvesting, energy storage, drug delivery systems photothermal therapies, and so on. These findings present opportunities for further exploration and utilization of these nanomaterials across various fields.

The remarkable performance of the ZnO@C nanocomposite can be attributed to the synergistic effects resulting from the combination of ZnO and carbon components. These synergies played a crucial role in enhancing the adsorption performance, while the nanocomposite's high surface area and porous structure provided an abundance of active sites for efficient pollutant adsorption. Furthermore, the adsorbents hold promise for the removal of heavy metals and other organic pollutants from water, broadening their potential applications in water treatment and environmental remediation. The adsorption processes investigated in this study were influenced by several factors, including initial pollutant concentration, contact time, and temperature. Optimal conditions were determined to achieve maximum pollutant removal efficiency, offering practical insights for real-world applications. The adsorption mechanisms were elucidated through the analysis of adsorption isotherms and kinetic modeling was employed to assess the adsorption kinetics, proving to be the most suitable for describing the adsorption of the pollutants. Moreover, the regeneration capabilities of the ZnO and carbon nanocomposite were demonstrated, indicating its potential for repeated use in water treatment processes. For future studies, this adsorbent has the potential to be utilized in water treatment for the effective removal of heavy metals and various organic pollutants from aqueous solutions. In summary, the findings have far-reaching implications for environmental remediation and water treatment, and future research in this area holds great promise for tackling the challenges posed by water pollution and ensuring the preservation of our ecosystems.

References

- (1) Feldman, V. I.; Ryazantsev, S. V.; Saenko, E. V.; Kameneva, S. V.; Shiryayeva, E. S. Matrix Isolation Model Studies on the Radiation-Induced Transformations of Small Molecules of Astrochemical and Atmospheric Interest. *Radiation Physics and Chemistry* **2016**, *124*, 7–13. <https://doi.org/10.1016/j.radphyschem.2015.12.005>.
- (2) Farimani, A. B.; Wu, Y.; Aluru, N. R. Rotational Motion of a Single Water Molecule in a Buckyball. *Physical Chemistry Chemical Physics* **2013**, *15* (41), 17993–18000. <https://doi.org/10.1039/c3cp53277a>.
- (3) Laing, M. *No Rabbit Ears on Water the Structure of the Water Molecule: What Should We Tell the Students?* <https://pubs.acs.org/sharingguidelines>.
- (4) Hossain, M. Z. WATER: THE MOST PRECIOUS RESOURCE OF OUR LIFE. **2015**.
- (5) Jewitt, G. *Can Integrated Water Resources Management Sustain the Provision of Ecosystem Goods and Services?* www.elsevier.com/locate/pce.
- (6) Flint, R. W. *UNIVERSITIES COUNCIL ON WATER RESOURCES The Sustainable Development of Water Resources Why Be Concerned About Water Quantity and Quality;* 2004; Vol. 127.
- (7) *Guidelines for Drinking-Water Quality SECOND ADDENDUM TO THIRD EDITION;* 2008.
- (8) Angelakis, A. N.; Bontoux, L. *Wastewater Reclamation and Reuse in Eureau Countries;* 2001; Vol. 3.
- (9) Caprara, A.; Wellington, J.; Lima, O.; Correia, A.; Marinho, P.; Gondim Calvasina, P.; Landim, L. P.; Sommerfeld, J. *Irregular Water Supply, Household Usage and Dengue: A*

Bio-Social Study in the Brazilian Northeast Abastecimento Irregular de Água, Seu Uso Domiciliar e Dengue: Uma Pesquisa Biossocial No Nordeste Do Brasil.

- (10) Emenike, C. P.; Tenebe, I. T.; Omole, D. O.; Ngene, B. U.; Oniemayin, B. I.; Maxwell, O.; Onoka, B. I. Accessing Safe Drinking Water in Sub-Saharan Africa: Issues and Challenges in South–West Nigeria. *Sustain Cities Soc* **2017**, *30*, 263–272. <https://doi.org/10.1016/j.scs.2017.01.005>.
- (11) Shiklomanov, I. A. Appraisal and Assessment of World Water Resources. *Water Int* **2000**, *25* (1), 11–32. <https://doi.org/10.1080/02508060008686794>.
- (12) Flörke, M.; Kynast, E.; Bärlund, I.; Eisner, S.; Wimmer, F.; Alcamo, J. Domestic and Industrial Water Uses of the Past 60 Years as a Mirror of Socio-Economic Development: A Global Simulation Study. *Global Environmental Change* **2013**, *23* (1), 144–156. <https://doi.org/10.1016/j.gloenvcha.2012.10.018>.
- (13) Palit, K.; Rath, S.; Chatterjee, S.; Das, S. Microbial Diversity and Ecological Interactions of Microorganisms in the Mangrove Ecosystem: Threats, Vulnerability, and Adaptations. *Environmental Science and Pollution Research*. Springer Science and Business Media Deutschland GmbH May 1, 2022, pp 32467–32512. <https://doi.org/10.1007/s11356-022-19048-7>.
- (14) Ringler, C.; Bhaduri, A.; Lawford, R. The Nexus across Water, Energy, Land and Food (WELF): Potential for Improved Resource Use Efficiency? *Current Opinion in Environmental Sustainability*. December 2013, pp 617–624. <https://doi.org/10.1016/j.cosust.2013.11.002>.
- (15) Thompson, S. E.; Sivapalan, M.; Harman, C. J.; Srinivasan, V.; Hipsey, M. R.; Reed, P.; Montanari, A.; Blöschl, G. Developing Predictive Insight into Changing Water Systems:

- Use-Inspired Hydrologic Science for the Anthropocene. *Hydrol Earth Syst Sci* **2013**, *17* (12), 5013–5039. <https://doi.org/10.5194/hess-17-5013-2013>.
- (16) Gleick, P. H.; Palaniappan, M. Peak Water Limits to Freshwater Withdrawal and Use. *Proc Natl Acad Sci U S A* **2010**, *107* (25), 11155–11162. <https://doi.org/10.1073/pnas.1004812107>.
- (17) Li, X.; Mei, Q.; Chen, L.; Zhang, H.; Dong, B.; Dai, X.; He, C.; Zhou, J. Enhancement in Adsorption Potential of Microplastics in Sewage Sludge for Metal Pollutants after the Wastewater Treatment Process. *Water Res* **2019**, *157*, 228–237. <https://doi.org/10.1016/j.watres.2019.03.069>.
- (18) Smith, S. C.; Rodrigues, D. F. Carbon-Based Nanomaterials for Removal of Chemical and Biological Contaminants from Water: A Review of Mechanisms and Applications. *Carbon*. Elsevier Ltd May 30, 2015, pp 122–143. <https://doi.org/10.1016/j.carbon.2015.04.043>.
- (19) Wingender, J.; Flemming, H. C. Biofilms in Drinking Water and Their Role as Reservoir for Pathogens. *Int J Hyg Environ Health* **2011**, *214* (6), 417–423. <https://doi.org/10.1016/j.ijheh.2011.05.009>.
- (20) Ayres, R. U.; Turton, H.; Casten, T. Energy Efficiency, Sustainability, and Economic Growth. *Energy* **2007**, *32* (5), 634–648. <https://doi.org/10.1016/j.energy.2006.06.005>.
- (21) Zhao, X.; Yu, X.; Wang, X.; Lai, S.; Sun, Y.; Yang, D. Recent Advances in Metal-Organic Frameworks for the Removal of Heavy Metal Oxoanions from Water. *Chemical Engineering Journal*. Elsevier B.V. March 1, 2021. <https://doi.org/10.1016/j.cej.2020.127221>.

- (22) Papapostolou, C. M.; Kondili, E. M.; Zafirakis, D. P.; Tzanes, G. T. Sustainable Water Supply Systems for the Islands: The Integration with the Energy Problem. *Renew Energy* **2020**, *146*, 2577–2588. <https://doi.org/10.1016/j.renene.2019.07.130>.
- (23) Gude, V. G. Energy and Water Autarky of Wastewater Treatment and Power Generation Systems. *Renewable and Sustainable Energy Reviews*. Elsevier Ltd 2015, pp 52–68. <https://doi.org/10.1016/j.rser.2015.01.055>.
- (24) Onorato, C.; Banasiak, L. J.; Schäfer, A. I. Inorganic Trace Contaminant Removal from Real Brackish Groundwater Using Electrodialysis. *Sep Purif Technol* **2017**, *187*, 426–435. <https://doi.org/10.1016/j.seppur.2017.06.016>.
- (25) Ghaffour, N.; Missimer, T. M.; Amy, G. L. Technical Review and Evaluation of the Economics of Water Desalination: Current and Future Challenges for Better Water Supply Sustainability. *Desalination* **2013**, *309*, 197–207. <https://doi.org/10.1016/j.desal.2012.10.015>.
- (26) Nong, D.; Wang, C.; Al-Amin, A. Q. A Critical Review of Energy Resources, Policies and Scientific Studies towards a Cleaner and More Sustainable Economy in Vietnam. *Renewable and Sustainable Energy Reviews*. Elsevier Ltd December 1, 2020. <https://doi.org/10.1016/j.rser.2020.110117>.
- (27) Kanwal, S.; Mehran, M. T.; Hassan, M.; Anwar, M.; Naqvi, S. R.; Khoja, A. H. An Integrated Future Approach for the Energy Security of Pakistan: Replacement of Fossil Fuels with Syngas for Better Environment and Socio-Economic Development. *Renewable and Sustainable Energy Reviews*. Elsevier Ltd March 1, 2022. <https://doi.org/10.1016/j.rser.2021.111978>.

- (28) Fiorenza, G.; Sharma, V. K.; Braccio, G. Techno-Economic Evaluation of a Solar Powered Water Desalination Plant. *Energy Convers Manag* **2003**, *44* (14), 2217–2240. [https://doi.org/10.1016/S0196-8904\(02\)00247-9](https://doi.org/10.1016/S0196-8904(02)00247-9).
- (29) Oyedepo, S. O. Towards Achieving Energy for Sustainable Development in Nigeria. *Renewable and Sustainable Energy Reviews*. Elsevier Ltd 2014, pp 255–272. <https://doi.org/10.1016/j.rser.2014.03.019>.
- (30) Chaturvedi, P.; Shukla, P.; Giri, B. S.; Chowdhary, P.; Chandra, R.; Gupta, P.; Pandey, A. Prevalence and Hazardous Impact of Pharmaceutical and Personal Care Products and Antibiotics in Environment: A Review on Emerging Contaminants. *Environmental Research*. Academic Press Inc. March 1, 2021. <https://doi.org/10.1016/j.envres.2020.110664>.
- (31) Cordell, D.; Rosemarin, A.; Schröder, J. J.; Smit, A. L. Towards Global Phosphorus Security: A Systems Framework for Phosphorus Recovery and Reuse Options. *Chemosphere* **2011**, *84* (6), 747–758. <https://doi.org/10.1016/j.chemosphere.2011.02.032>.
- (32) Larsen, T. A.; Gujer, W. The Concept of Sustainable Urban Water Management. *Water Science and Technology* **1997**, *35* (9), 3–10. [https://doi.org/10.1016/S0273-1223\(97\)00179-0](https://doi.org/10.1016/S0273-1223(97)00179-0).
- (33) Saravanan, A.; Senthil Kumar, P.; Jeevanantham, S.; Karishma, S.; Tajsabreen, B.; Yaashikaa, P. R.; Reshma, B. Effective Water/Wastewater Treatment Methodologies for Toxic Pollutants Removal: Processes and Applications towards Sustainable Development. *Chemosphere* **2021**, 280. <https://doi.org/10.1016/j.chemosphere.2021.130595>.

- (34) Sharma, P.; Dutta, D.; Udayan, A.; Kumar, S. Industrial Wastewater Purification through Metal Pollution Reduction Employing Microbes and Magnetic Nanocomposites. *J Environ Chem Eng* **2021**, *9* (6). <https://doi.org/10.1016/j.jece.2021.106673>.
- (35) Gunatilake SK. *Methods of Removing Heavy Metals from Industrial Wastewater*; 2015; Vol. 1. www.jmess.org.
- (36) Ahmad, A.; Mohd-Setapar, S. H.; Chuong, C. S.; Khatoon, A.; Wani, W. A.; Kumar, R.; Rafatullah, M. Recent Advances in New Generation Dye Removal Technologies: Novel Search for Approaches to Reprocess Wastewater. *RSC Advances*. Royal Society of Chemistry 2015, pp 30801–30818. <https://doi.org/10.1039/c4ra16959j>.
- (37) Rashid, R.; Shafiq, I.; Akhter, P.; Muhammad, & Iqbal, J.; Hussain, M. A State-of-the-Art Review on Wastewater Treatment Techniques: The Effectiveness of Adsorption Method. <https://doi.org/10.1007/s11356-021-12395-x>/Published.
- (38) Mojiri, A.; Aziz, H. A.; Aziz, S. Q. Trends in Physical-Chemical Methods for Landfill Leachate Treatment. *International Journal of Scientific Research in Environmental Sciences* **2013**, 16–25. <https://doi.org/10.12983/ijres-2013-p016-025>.
- (39) Raghu, S.; Lee, C. W.; Chellammal, S.; Palanichamy, S.; Basha, C. A. Evaluation of Electrochemical Oxidation Techniques for Degradation of Dye Effluents-A Comparative Approach. *J Hazard Mater* **2009**, *171* (1–3), 748–754. <https://doi.org/10.1016/j.jhazmat.2009.06.063>.
- (40) Medfu Tarekegn, M.; Zewdu Salilih, F.; Ishetu, A. I. Microbes Used as a Tool for Bioremediation of Heavy Metal from the Environment. *Cogent Food and Agriculture*. Informa Healthcare 2020. <https://doi.org/10.1080/23311932.2020.1783174>.

- (41) Intisar, A.; Ramzan, A.; Hafeez, S.; Hussain, N.; Irfan, M.; Shakeel, N.; Gill, K. A.; Iqbal, A.; Janczarek, M.; Jesionowski, T. Adsorptive and Photocatalytic Degradation Potential of Porous Polymeric Materials for Removal of Pesticides, Pharmaceuticals, and Dyes-Based Emerging Contaminants from Water. *Chemosphere* **2023**, 336. <https://doi.org/10.1016/j.chemosphere.2023.139203>.
- (42) Li, P.; Gao, B.; Li, A.; Yang, H. Evaluation of the Selective Adsorption of Silica-Sand/Anionized-Starch Composite for Removal of Dyes and Copper (II) from Their Aqueous Mixtures. *Int J Biol Macromol* **2020**, 149, 1285–1293. <https://doi.org/10.1016/j.ijbiomac.2020.02.047>.
- (43) Dolatabadi, M.; Naidu, H.; Ahmadzadeh, S. A Green Approach to Remove Acetamiprid Insecticide Using Pistachio Shell-Based Modified Activated Carbon; Economical Groundwater Treatment. *J Clean Prod* **2021**, 316. <https://doi.org/10.1016/j.jclepro.2021.128226>.
- (44) Bushra, R.; Mohamad, S.; Alias, Y.; Jin, Y.; Ahmad, M. Current Approaches and Methodologies to Explore the Perceptive Adsorption Mechanism of Dyes on Low-Cost Agricultural Waste: A Review. *Microporous and Mesoporous Materials*. Elsevier B.V. May 1, 2021. <https://doi.org/10.1016/j.micromeso.2021.111040>.
- (45) Khairul Zaman, N.; Rohani, R.; Izni Yusoff, I.; Kamsol, M. A.; Basiron, S. A.; Aina, A. I. Eco-Friendly Coagulant versus Industrially Used Coagulants: Identification of Their Coagulation Performance, Mechanism and Optimization in Water Treatment Process. *Int J Environ Res Public Health* **2021**, 18 (17). <https://doi.org/10.3390/ijerph18179164>.
- (46) Noveron, J. C.; Geoffrey Saupe, C. B.; Fortier, S. A.; Lin, Y.; Ambler, C. H. *SYNTHESIS OF ADVANCED FUNCTIONAL NANOMATERIALS FOR SUSTAINABLE WATER*

- (47) Ngulube, T.; Gumbo, J. R.; Masindi, V.; Maity, A. An Update on Synthetic Dyes Adsorption onto Clay Based Minerals: A State-of-Art Review. *Journal of Environmental Management*. Academic Press April 15, 2017, pp 35–57. <https://doi.org/10.1016/j.jenvman.2016.12.031>.
- (48) Wan Ngah, W. S.; Teong, L. C.; Hanafiah, M. A. K. M. Adsorption of Dyes and Heavy Metal Ions by Chitosan Composites: A Review. *Carbohydrate Polymers*. February 1, 2011, pp 1446–1456. <https://doi.org/10.1016/j.carbpol.2010.11.004>.
- (49) Maleki, A.; Moradi, F.; Shahmoradi, B.; Rezaee, R.; Lee, S. M. The Photocatalytic Removal of Diazinon from Aqueous Solutions Using Tungsten Oxide Doped Zinc Oxide Nanoparticles Immobilized on Glass Substrate. *J Mol Liq* **2020**, 297. <https://doi.org/10.1016/j.molliq.2019.111918>.
- (50) Szostak, K.; Banach, M. Sorption and Photocatalytic Degradation of Methylene Blue on Bentonite-ZnO-CuO Nanocomposite. *J Mol Liq* **2019**, 286. <https://doi.org/10.1016/j.molliq.2019.04.136>.
- (51) Kausar, A.; Iqbal, M.; Javed, A.; Aftab, K.; Nazli, Z. i. H.; Bhatti, H. N.; Nouren, S. Dyes Adsorption Using Clay and Modified Clay: A Review. *J Mol Liq* **2018**, 256, 395–407. <https://doi.org/10.1016/j.molliq.2018.02.034>.
- (52) Ljubas, D.; Smoljanić, G.; Juretić, H. Degradation of Methyl Orange and Congo Red Dyes by Using TiO₂ Nanoparticles Activated by the Solar and the Solar-like Radiation. *J Environ Manage* **2015**, 161, 83–91. <https://doi.org/10.1016/j.jenvman.2015.06.042>.

- (53) Parshetti, G. K.; Telke, A. A.; Kalyani, D. C.; Govindwar, S. P. Decolorization and Detoxification of Sulfonated Azo Dye Methyl Orange by *Kocuria Rosea* MTCC 1532. *J Hazard Mater* **2010**, *176* (1–3), 503–509. <https://doi.org/10.1016/j.jhazmat.2009.11.058>.
- (54) Slokar, Y. M.; Le Marechal, A. M. *Methods of Decoloration of Textile Wastewaters*; 1998; Vol. 37.
- (55) Kepa, U.; Stanczyk-Mazanek, E.; Stepniak, L. The Use of the Advanced Oxidation Process in the Ozone + Hydrogen Peroxide System for the Removal of Cyanide from Water. *Desalination* **2008**, *223* (1–3), 187–193. <https://doi.org/10.1016/j.desal.2007.01.215>.
- (56) Jain, R.; Mathur, M.; Sikarwar, S.; Mittal, A. Removal of the Hazardous Dye Rhodamine B through Photocatalytic and Adsorption Treatments. *J Environ Manage* **2007**, *85* (4), 956–964. <https://doi.org/10.1016/j.jenvman.2006.11.002>.
- (57) Guimarães, J. R.; Guedes Maniero, M.; Nogueira de Araújo, R. A Comparative Study on the Degradation of RB-19 Dye in an Aqueous Medium by Advanced Oxidation Processes. *J Environ Manage* **2012**, *110*, 33–39. <https://doi.org/10.1016/j.jenvman.2012.05.020>.
- (58) Stephenson @, R. J.; Dufft, S. J. B. *COAGULATION AND PRECIPITATION OF A MECHANICAL PULPING EFFLUENT-I. REMOVAL OF CARBON, COLOUR AND TURBIDITY*; 1996; Vol. 30.
- (59) Riera-Torres, M.; Gutiérrez-Bouzán, C.; Crespi, M. Combination of Coagulation-Flocculation and Nanofiltration Techniques for Dye Removal and Water Reuse in Textile Effluents. *Desalination* **2010**, *252* (1–3), 53–59. <https://doi.org/10.1016/j.desal.2009.11.002>.

- (60) Kaur, J.; Bansal, S.; Singhal, S. Photocatalytic Degradation of Methyl Orange Using ZnO Nanopowders Synthesized via Thermal Decomposition of Oxalate Precursor Method. *Physica B Condens Matter* **2013**, *416*, 33–38. <https://doi.org/10.1016/j.physb.2013.02.005>.
- (61) García-Montaña, J.; Domènech, X.; García-Hortal, J. A.; Torrades, F.; Peral, J. The Testing of Several Biological and Chemical Coupled Treatments for Cibacron Red FN-R Azo Dye Removal. *J Hazard Mater* **2008**, *154* (1–3), 484–490. <https://doi.org/10.1016/j.jhazmat.2007.10.050>.
- (62) Abdullah, A. M.; Gracia-Pinilla, M.; Pillai, S. C.; O’Shea, K. UV and Visible Light-Driven Production of Hydroxyl Radicals by Reduced Forms of N, F, and P Codoped Titanium Dioxide. *Molecules* **2019**, *24* (11). <https://doi.org/10.3390/molecules24112147>.
- (63) Lu, Z.; Gao, J.; He, Q.; Wu, J.; Liang, D.; Yang, H.; Chen, R. Enhanced Antibacterial and Wound Healing Activities of Microporous Chitosan-Ag/ZnO Composite Dressing. *Carbohydr Polym* **2017**, *156*, 460–469. <https://doi.org/10.1016/j.carbpol.2016.09.051>.
- (64) Hu, G.; Guo, W.; Yu, R.; Yang, X.; Zhou, R.; Pan, C.; Wang, Z. L. Enhanced Performances of Flexible ZnO/Perovskite Solar Cells by Piezo-Phototronic Effect. *Nano Energy* **2016**, *23*, 27–33. <https://doi.org/10.1016/j.nanoen.2016.02.057>.
- (65) Lin, C. S.; Hwang, C. C.; Lee, W. H.; Tong, W. Y. Preparation of Zinc Oxide (ZnO) Powders with Different Types of Morphology by a Combustion Synthesis Method. *Mater Sci Eng B Solid State Mater Adv Technol* **2007**, *140* (1–2), 31–37. <https://doi.org/10.1016/j.mseb.2007.03.023>.
- (66) Islam, M. T.; Jing, H.; Yang, T.; Zubia, E.; Goos, A. G.; Bernal, R. A.; Botez, C. E.; Narayan, M.; Chan, C. K.; Noveron, J. C. Fullerene Stabilized Gold Nanoparticles Supported on Titanium Dioxide for Enhanced Photocatalytic Degradation of Methyl Orange

- and Catalytic Reduction of 4-Nitrophenol. *J Environ Chem Eng* **2018**, 6 (4), 3827–3836.
<https://doi.org/10.1016/j.jece.2018.05.032>.
- (67) Chen, Y.; He, F.; Ren, Y.; Peng, H.; Huang, K. Fabrication of Chitosan/PAA Multilayer onto Magnetic Microspheres by LbL Method for Removal of Dyes. *Chemical Engineering Journal* **2014**, 249, 79–92. <https://doi.org/10.1016/j.cej.2014.03.093>.
- (68) Islam, M. T.; Dominguez, A.; Turley, R. S.; Kim, H.; Sultana, K. A.; Shuvo, M. A. I.; Alvarado-Tenorio, B.; Montes, M. O.; Lin, Y.; Gardea-Torresdey, J.; Noveron, J. C. Development of Photocatalytic Paint Based on TiO₂ and Photopolymer Resin for the Degradation of Organic Pollutants in Water. *Science of the Total Environment* **2020**, 704. <https://doi.org/10.1016/j.scitotenv.2019.135406>.
- (69) Wahab, R.; Hwang, I. H.; Kim, Y. S.; Shin, H. S. Photocatalytic Activity of Zinc Oxide Micro-Flowers Synthesized via Solution Method. *Chemical Engineering Journal* **2011**, 168 (1), 359–366. <https://doi.org/10.1016/j.cej.2011.01.038>.
- (70) Barreca, D.; Carraro, G.; Gasparotto, A.; Maccato, C.; Altantzis, T.; Sada, C.; Kaunisto, K.; Ruoko, T. P.; Bals, S. Vapor Phase Fabrication of Nanoheterostructures Based on ZnO for Photoelectrochemical Water Splitting. *Adv Mater Interfaces* **2017**, 4 (18). <https://doi.org/10.1002/admi.201700161>.
- (71) Król, A.; Pomastowski, P.; Rafińska, K.; Railean-Plugaru, V.; Buszewski, B. Zinc Oxide Nanoparticles: Synthesis, Antiseptic Activity and Toxicity Mechanism. *Advances in Colloid and Interface Science*. Elsevier B.V. November 1, 2017, pp 37–52. <https://doi.org/10.1016/j.cis.2017.07.033>.

- (72) Rajeswari Yogamalar, N.; Chandra Bose, A. Tuning the Aspect Ratio of Hydrothermally Grown ZnO by Choice of Precursor. *J Solid State Chem* **2011**, *184* (1), 12–20. <https://doi.org/10.1016/j.jssc.2010.10.024>.
- (73) Abdullah, A. M.; O’Shea, K. E. TiO₂ Photocatalytic Degradation of the Flame-Retardant Tris (2-Chloroethyl) Phosphate (TCEP) in Aqueous Solution: A Detailed Kinetic and Mechanistic Study. *J Photochem Photobiol A Chem* **2019**, *377*, 130–137. <https://doi.org/10.1016/j.jphotochem.2019.03.026>.
- (74) Islam, M. T.; Padilla, J. E.; Dominguez, N.; Alvarado, D. C.; Alam, M. S.; Cooke, P.; Tecklenburg, M. M. J.; Noveron, J. C. Green Synthesis of Gold Nanoparticles Reduced and Stabilized by Squaric Acid and Supported on Cellulose Fibers for the Catalytic Reduction of 4-Nitrophenol in Water. *RSC Adv* **2016**, *6* (94), 91185–91191. <https://doi.org/10.1039/c6ra17480a>.
- (75) Mirzaei, H.; Darroudi, M. Zinc Oxide Nanoparticles: Biological Synthesis and Biomedical Applications. *Ceramics International*. Elsevier Ltd January 1, 2017, pp 907–914. <https://doi.org/10.1016/j.ceramint.2016.10.051>.
- (76) Ullah, R.; Dutta, J. Photocatalytic Degradation of Organic Dyes with Manganese-Doped ZnO Nanoparticles. *J Hazard Mater* **2008**, *156* (1–3), 194–200. <https://doi.org/10.1016/j.jhazmat.2007.12.033>.
- (77) Kang, H. W.; Leem, J.; Yoon, S. Y.; Sung, H. J. Continuous Synthesis of Zinc Oxide Nanoparticles in a Microfluidic System for Photovoltaic Application. *Nanoscale* **2014**, *6* (5), 2840–2846. <https://doi.org/10.1039/c3nr06141h>.

- (78) Chen, D.; Ai, S.; Liang, Z.; Wei, F. Preparation and Photocatalytic Properties of Zinc Oxide Nanoparticles by Microwave-Assisted Ball Milling. *Ceram Int* **2016**, *42* (2), 3692–3696. <https://doi.org/10.1016/j.ceramint.2015.10.123>.
- (79) Hossain, M. A.; Karoyo, A. H.; Dehabadi, L.; Fathieh, F.; Simonson, C. J.; Wilson, L. D. Starch Particles, Energy Harvesting, and the “Goldilocks Effect.” *ACS Omega* **2018**, *3* (4), 3796–3803. <https://doi.org/10.1021/acsomega.8b00131>.
- (80) Verma, S.; Dutta, R. K. Enhanced ROS Generation by ZnO-Ammonia Modified Graphene Oxide Nanocomposites for Photocatalytic Degradation of Trypan Blue Dye and 4-Nitrophenol. *J Environ Chem Eng* **2017**, *5* (5), 4776–4787. <https://doi.org/10.1016/j.jece.2017.08.026>.
- (81) Chen, Y.; Fan, Z.; Zhang, Z.; Niu, W.; Li, C.; Yang, N.; Chen, B.; Zhang, H. Two-Dimensional Metal Nanomaterials: Synthesis, Properties, and Applications. *Chemical Reviews*. American Chemical Society July 11, 2018, pp 6409–6455. <https://doi.org/10.1021/acs.chemrev.7b00727>.
- (82) Singh, J.; Dutta, T.; Kim, K. H.; Rawat, M.; Samddar, P.; Kumar, P. “Green” Synthesis of Metals and Their Oxide Nanoparticles: Applications for Environmental Remediation. *Journal of Nanobiotechnology*. BioMed Central Ltd. October 30, 2018. <https://doi.org/10.1186/s12951-018-0408-4>.
- (83) Weldegebrieal, G. K.; Sibhatu, A. K. Photocatalytic Activity of Biosynthesized α -Fe₂O₃ Nanoparticles for the Degradation of Methylene Blue and Methyl Orange Dyes. *Optik (Stuttg)* **2021**, *241*. <https://doi.org/10.1016/j.ijleo.2021.167226>.
- (84) Abd-Elrahim, A. G.; Chun, D. M. Room-Temperature Deposition of ZnO-Graphene Nanocomposite Hybrid Photocatalysts for Improved Visible-Light-Driven Degradation of

- Methylene Blue. *Ceram Int* **2021**, *47* (9), 12812–12825.
<https://doi.org/10.1016/j.ceramint.2021.01.142>.
- (85) Luque, P. A.; Garrafa-Gálvez, H. E.; Nava, O.; Olivas, A.; Martínez-Rosas, M. E.; Vilchis-Nestor, A. R.; Villegas-Fuentes, A.; Chinchillas-Chinchillas, M. J. Efficient Sunlight and UV Photocatalytic Degradation of Methyl Orange, Methylene Blue and Rhodamine B, Using Citrus×paradisi Synthesized SnO₂ Semiconductor Nanoparticles. *Ceram Int* **2021**, *47* (17), 23861–23874. <https://doi.org/10.1016/j.ceramint.2021.05.094>.
- (86) Perillo, P. M.; Atia, M. N. Solar-Assisted Photodegradation of Methyl Orange Using Cu-Doped ZnO Nanorods. *Mater Today Commun* **2018**, *17*, 252–258.
<https://doi.org/10.1016/j.mtcomm.2018.09.010>.
- (87) R., S.; Jebasingh, J. A.; S., M. V.; Stanley, P. K.; Ponmani, P.; Shekinah, M. E.; Vasanthi, J. Excellent Photocatalytic Degradation of Methylene Blue, Rhodamine B and Methyl Orange Dyes by Ag-ZnO Nanocomposite under Natural Sunlight Irradiation. *Optik (Stuttg)* **2021**, *231*. <https://doi.org/10.1016/j.ijleo.2021.166518>.
- (88) Zhao, C.; Chen, A.; Ji, X.; Zhu, Y.; Gui, X.; Huang, F.; Tang, Z. Growth of Vertically Aligned ZnO Nanowire Arrays on ZnO Single Crystals. *Mater Lett* **2015**, *154*, 40–43.
<https://doi.org/10.1016/j.matlet.2015.04.053>.
- (89) Molla, M. A. I.; Furukawa, M.; Tateishi, I.; Katsumata, H.; Kaneco, S. Studies of Effects of Calcination Temperature on the Crystallinity and Optical Properties of Ag-Doped ZnO Nanocomposites. *Journal of Composites Science* **2019**, *3* (1).
<https://doi.org/10.3390/jcs3010018>.
- (90) Shah, A. A.; Bhatti, M. A.; Tahira, A.; Chandio, A. D.; Channa, I. A.; Sahito, A. G.; Chalangar, E.; Willander, M.; Nur, O.; Ibupoto, Z. H. Facile Synthesis of Copper Doped

- ZnO Nanorods for the Efficient Photo Degradation of Methylene Blue and Methyl Orange. *Ceram Int* **2020**, *46* (8), 9997–10005. <https://doi.org/10.1016/j.ceramint.2019.12.024>.
- (91) Uribe-López, M. C.; Hidalgo-López, M. C.; López-González, R.; Frías-Márquez, D. M.; Núñez-Nogueira, G.; Hernández-Castillo, D.; Alvarez-Lemus, M. A. Photocatalytic Activity of ZnO Nanoparticles and the Role of the Synthesis Method on Their Physical and Chemical Properties. *J Photochem Photobiol A Chem* **2021**, *404*. <https://doi.org/10.1016/j.jphotochem.2020.112866>.
- (92) Kumar, R.; Kumar, G.; Umar, A. ZnO Nano-Mushrooms for Photocatalytic Degradation of Methyl Orange. *Mater Lett* **2013**, *97*, 100–103. <https://doi.org/10.1016/j.matlet.2013.01.044>.
- (93) Lang, J.; Wang, J.; Zhang, Q.; Li, X.; Han, Q.; Wei, M.; Sui, Y.; Wang, D.; Yang, J. Chemical Precipitation Synthesis and Significant Enhancement in Photocatalytic Activity of Ce-Doped ZnO Nanoparticles. *Ceram Int* **2016**, *42* (12), 14175–14181. <https://doi.org/10.1016/j.ceramint.2016.06.042>.
- (94) Luo, X.; Killard, A. J.; Morrin, A.; Smyth, M. R. Enhancement of a Conducting Polymer-Based Biosensor Using Carbon Nanotube-Doped Polyaniline. *Anal Chim Acta* **2006**, *575* (1), 39–44. <https://doi.org/10.1016/j.aca.2006.05.064>.
- (95) Lv, Z.; Liu, L.; Zhangyang, X.; Lu, F.; Tian, J. Optimized Design of Gradient Al Component Al_xGa_{1-x}N Nanostructure with Hexagonal Periodic Arrangement for Enhanced Optical Absorption of Ultraviolet Photodetectors. *Photonics and Nanostructures - Fundamentals and Applications*. Elsevier B.V. February 1, 2021. <https://doi.org/10.1016/j.photonics.2020.100885>.

- (96) Krzywiecki, M.; Grządziel, L.; Sarfraz, A.; Iqbal, D.; Szwajca, A.; Erbe, A. Zinc Oxide as a Defect-Dominated Material in Thin Films for Photovoltaic Applications-Experimental Determination of Defect Levels, Quantification of Composition, and Construction of Band Diagram. *Physical Chemistry Chemical Physics* **2015**, *17* (15), 10004–10013. <https://doi.org/10.1039/c5cp00112a>.
- (97) Lang, J.; Wang, J.; Zhang, Q.; Li, X.; Han, Q.; Wei, M.; Sui, Y.; Wang, D.; Yang, J. Chemical Precipitation Synthesis and Significant Enhancement in Photocatalytic Activity of Ce-Doped ZnO Nanoparticles. *Ceram Int* **2016**, *42* (12), 14175–14181. <https://doi.org/10.1016/j.ceramint.2016.06.042>.
- (98) Mofokeng, S. J.; Kumar, V.; Kroon, R. E.; Ntwaeaborwa, O. M. Structure and Optical Properties of Dy³⁺ Activated Sol-Gel ZnO-TiO₂ Nanocomposites. *J Alloys Compd* **2017**, *711*, 121–131. <https://doi.org/10.1016/j.jallcom.2017.03.345>.
- (99) Wang, Z. L. ZnO Nanowire and Nanobelt Platform for Nanotechnology. *Materials Science and Engineering R: Reports*. April 3, 2009, pp 33–71. <https://doi.org/10.1016/j.mser.2009.02.001>.
- (100) Chandekar, K. V.; Shkir, M.; Khan, A.; Al-Shehri, B. M.; Hamdy, M. S.; AlFaify, S.; El-Toni, M. A.; Aldalbahi, A.; Ansari, A. A.; Ghaithan, H. A Facile One-Pot Flash Combustion Synthesis of La@ZnO Nanoparticles and Their Characterizations for Optoelectronic and Photocatalysis Applications. *J Photochem Photobiol A Chem* **2020**, 395. <https://doi.org/10.1016/j.jphotochem.2020.112465>.
- (101) Sultana, K. A.; Islam, M. T.; Silva, J. A.; Turley, R. S.; Hernandez-Viezcas, J. A.; Gardea-Torresdey, J. L.; Noveron, J. C. Sustainable Synthesis of Zinc Oxide Nanoparticles for

- Photocatalytic Degradation of Organic Pollutant and Generation of Hydroxyl Radical. *J Mol Liq* **2020**, *307*. <https://doi.org/10.1016/j.molliq.2020.112931>.
- (102) Yu, J.; Yu, X. Hydrothermal Synthesis and Photocatalytic Activity of Zinc Oxide Hollow Spheres. *Environ Sci Technol* **2008**, *42* (13), 4902–4907. <https://doi.org/10.1021/es800036n>.
- (103) Bekkari, R.; Iâanab, L.; Boyer, D.; Mahiou, R.; Jaber, B. Influence of the Sol Gel Synthesis Parameters on the Photoluminescence Properties of ZnO Nanoparticles. *Mater Sci Semicond Process* **2017**, *71*, 181–187. <https://doi.org/10.1016/j.mssp.2017.07.027>.
- (104) Yu, W.; Zhang, J.; Peng, T. New Insight into the Enhanced Photocatalytic Activity of N-, C- and S-Doped ZnO Photocatalysts. *Appl Catal B* **2016**, *181*, 220–227. <https://doi.org/10.1016/j.apcatb.2015.07.031>.
- (105) Saravanan, R.; Mansoob Khan, M.; Gupta, V. K.; Mosquera, E.; Gracia, F.; Narayanan, V.; Stephen, A. ZnO/Ag/CdO Nanocomposite for Visible Light-Induced Photocatalytic Degradation of Industrial Textile Effluents. *J Colloid Interface Sci* **2015**, *452*, 126–133. <https://doi.org/10.1016/j.jcis.2015.04.035>.
- (106) Yu, J.; Yu, X. Hydrothermal Synthesis and Photocatalytic Activity of Zinc Oxide Hollow Spheres. *Environ Sci Technol* **2008**, *42* (13), 4902–4907. <https://doi.org/10.1021/es800036n>.
- (107) Kumar, S. G.; Rao, K. S. R. K. Zinc Oxide Based Photocatalysis: Tailoring Surface-Bulk Structure and Related Interfacial Charge Carrier Dynamics for Better Environmental Applications. *RSC Advances*. Royal Society of Chemistry 2015, pp 3306–3351. <https://doi.org/10.1039/c4ra13299h>.

- (108) Aruna, S. T.; Mukasyan, A. S. Combustion Synthesis and Nanomaterials. *Current Opinion in Solid State and Materials Science*. June 2008, pp 44–50. <https://doi.org/10.1016/j.cossms.2008.12.002>.
- (109) Naik, M. A.; Mishra, B. G.; Dubey, A. Combustion Synthesized WO₃-ZrO₂ Nanocomposites as Catalyst for the Solvent-Free Synthesis of Coumarins. *Colloids Surf A Physicochem Eng Asp* **2008**, *317* (1–3), 234–238. <https://doi.org/10.1016/j.colsurfa.2007.10.019>.
- (110) Xu, C.; Nasrollahzadeh, M.; Sajjadi, M.; Maham, M.; Luque, R.; Puente-Santiago, A. R. Benign-by-Design Nature-Inspired Nanosystems in Biofuels Production and Catalytic Applications. *Renewable and Sustainable Energy Reviews* **2019**, *112*, 195–252. <https://doi.org/10.1016/j.rser.2019.03.062>.
- (111) Hariharan, C. Photocatalytic Degradation of Organic Contaminants in Water by ZnO Nanoparticles: Revisited. *Appl Catal A Gen* **2006**, *304* (1–2), 55–61. <https://doi.org/10.1016/j.apcata.2006.02.020>.
- (112) Maleki, A.; Moradi, F.; Shahmoradi, B.; Rezaee, R.; Lee, S. M. The Photocatalytic Removal of Diazinon from Aqueous Solutions Using Tungsten Oxide Doped Zinc Oxide Nanoparticles Immobilized on Glass Substrate. *J Mol Liq* **2020**, *297*. <https://doi.org/10.1016/j.molliq.2019.111918>.
- (113) Ljubas, D.; Smoljanić, G.; Juretić, H. Degradation of Methyl Orange and Congo Red Dyes by Using TiO₂ Nanoparticles Activated by the Solar and the Solar-like Radiation. *J Environ Manage* **2015**, *161*, 83–91. <https://doi.org/10.1016/j.jenvman.2015.06.042>.

- (114) Wan Ngah, W. S.; Teong, L. C.; Hanafiah, M. A. K. M. Adsorption of Dyes and Heavy Metal Ions by Chitosan Composites: A Review. *Carbohydrate Polymers*. February 1, 2011, pp 1446–1456. <https://doi.org/10.1016/j.carbpol.2010.11.004>.
- (115) Maleki, A.; Moradi, F.; Shahmoradi, B.; Rezaee, R.; Lee, S. M. The Photocatalytic Removal of Diazinon from Aqueous Solutions Using Tungsten Oxide Doped Zinc Oxide Nanoparticles Immobilized on Glass Substrate. *J Mol Liq* **2020**, 297. <https://doi.org/10.1016/j.molliq.2019.111918>.
- (116) Kumar, R.; Kumar, G.; Akhtar, M. S.; Umar, A. Sonophotocatalytic Degradation of Methyl Orange Using ZnO Nano-Aggregates. *J Alloys Compd* **2015**, 629, 167–172. <https://doi.org/10.1016/j.jallcom.2014.12.232>.
- (117) Kausar, A.; Iqbal, M.; Javed, A.; Aftab, K.; Nazli, Z. i. H.; Bhatti, H. N.; Nouren, S. Dyes Adsorption Using Clay and Modified Clay: A Review. *J Mol Liq* **2018**, 256, 395–407. <https://doi.org/10.1016/j.molliq.2018.02.034>.
- (118) Pirkarami, A.; Olya, M. E. Removal of Dye from Industrial Wastewater with an Emphasis on Improving Economic Efficiency and Degradation Mechanism. *Journal of Saudi Chemical Society* **2017**, 21, S179–S186. <https://doi.org/10.1016/j.jscs.2013.12.008>.
- (119) Hwang, C.-C.; Wu, T.-Y. Synthesis and Characterization of Nanocrystalline ZnO Powders by a Novel Combustion Synthesis Method. *Materials Science and Engineering: B* **2004**, 111 (2–3), 197–206. <https://doi.org/10.1016/j.mseb.2004.04.021>.
- (120) Slokar, Y. M.; Le Marechal, A. M. *Methods of Decoloration of Textile Wastewaters*; 1998; Vol. 37.

- (121) Tripathy, N.; Ahmad, R.; Eun Song, J.; Ah Ko, H.; Hahn, Y. B.; Khang, G. Photocatalytic Degradation of Methyl Orange Dye by ZnO Nanoneedle under UV Irradiation. *Mater Lett* **2014**, *136*, 171–174. <https://doi.org/10.1016/j.matlet.2014.08.064>.
- (122) Sharma, H.; Kaur, N.; Singh, N.; Jang, D. O. Synergetic Catalytic Effect of Ionic Liquids and ZnO Nanoparticles on the Selective Synthesis of 1,2-Disubstituted Benzimidazoles Using a Ball-Milling Technique. *Green Chemistry* **2015**, *17* (8), 4263–4270. <https://doi.org/10.1039/c5gc00536a>.
- (123) Ngulube, T.; Gumbo, J. R.; Masindi, V.; Maity, A. An Update on Synthetic Dyes Adsorption onto Clay Based Minerals: A State-of-Art Review. *Journal of Environmental Management*. Academic Press April 15, 2017, pp 35–57. <https://doi.org/10.1016/j.jenvman.2016.12.031>.
- (124) Sajjad, A. K. L.; Sajjad, S.; Iqbal, A.; Ryma, N. ul A. ZnO/WO₃ Nanostructure as an Efficient Visible Light Catalyst. *Ceram Int* **2018**, *44* (8), 9364–9371. <https://doi.org/10.1016/j.ceramint.2018.02.150>.
- (125) Xia, S.; Liu, L.; Kong, Y.; Wang, M. Uniaxial Strain Effects on the Optoelectronic Properties of GaN Nanowires. *Superlattices Microstruct* **2016**, *97*, 327–334. <https://doi.org/10.1016/j.spmi.2016.06.040>.
- (126) Kaur, J.; Bansal, S.; Singhal, S. Photocatalytic Degradation of Methyl Orange Using ZnO Nanopowders Synthesized via Thermal Decomposition of Oxalate Precursor Method. *Physica B Condens Matter* **2013**, *416*, 33–38. <https://doi.org/10.1016/j.physb.2013.02.005>.
- (127) Pirkarami, A.; Olya, M. E. Removal of Dye from Industrial Wastewater with an Emphasis on Improving Economic Efficiency and Degradation Mechanism. *Journal of Saudi Chemical Society* **2017**, *21*, S179–S186. <https://doi.org/10.1016/j.jscs.2013.12.008>.

- (128) Islam, M. T.; Dominguez, A.; Alvarado-Tenorio, B.; Bernal, R. A.; Montes, M. O.; Noveron, J. C. Sucrose-Mediated Fast Synthesis of Zinc Oxide Nanoparticles for the Photocatalytic Degradation of Organic Pollutants in Water. *ACS Omega* **2019**, *4* (4), 6560–6572. <https://doi.org/10.1021/acsomega.9b00023>.
- (129) Ong, C. B.; Ng, L. Y.; Mohammad, A. W. A Review of ZnO Nanoparticles as Solar Photocatalysts: Synthesis, Mechanisms and Applications. *Renewable and Sustainable Energy Reviews*. Elsevier Ltd 2018, pp 536–551. <https://doi.org/10.1016/j.rser.2017.08.020>.
- (130) He, Z.; Zhang, Z.; Bi, S. Nanoparticles for Organic Electronics Applications. *Mater Res Express* **2020**, *7* (1). <https://doi.org/10.1088/2053-1591/ab636f>.
- (131) Vafaei, M.; Ghamsari, M. S. Preparation and Characterization of ZnO Nanoparticles by a Novel Sol-Gel Route. *Mater Lett* **2007**, *61* (14–15), 3265–3268. <https://doi.org/10.1016/j.matlet.2006.11.089>.
- (132) Wang, X.; Song, J.; Wang, Z. L. Nanowire and Nanobelt Arrays of Zinc Oxide from Synthesis to Properties and to Novel Devices. *J Mater Chem* **2007**, *17* (8), 711–720. <https://doi.org/10.1039/b616963p>.
- (133) Senthil Kumar, P.; Saravanan, A. Sustainable Wastewater Treatments in Textile Sector. In *Sustainable Fibres and Textiles*; Elsevier Inc., 2017; pp 323–346. <https://doi.org/10.1016/B978-0-08-102041-8.00011-1>.
- (134) Wang, Q.; Li, J.; Bai, Y.; Lu, X.; Ding, Y.; Yin, S.; Huang, H.; Ma, H.; Wang, F.; Su, B. Photodegradation of Textile Dye Rhodamine B over a Novel Biopolymer–Metal Complex Wool-Pd/CdS Photocatalysts under Visible Light Irradiation. *J Photochem Photobiol B* **2013**, *126*, 47–54. <https://doi.org/10.1016/j.jphotobiol.2013.07.007>.

- (135) Lin, H. F.; Liao, S. C.; Hung, S. W. The Dc Thermal Plasma Synthesis of ZnO Nanoparticles for Visible-Light Photocatalyst. *J Photochem Photobiol A Chem* **2005**, *174* (1), 82–87. <https://doi.org/10.1016/j.jphotochem.2005.02.015>.
- (136) Siva, N.; Sakthi, D.; Ragupathy, S.; Arun, V.; Kannadasan, N. Synthesis, Structural, Optical and Photocatalytic Behavior of Sn Doped ZnO Nanoparticles. *Mater Sci Eng B Solid State Mater Adv Technol* **2020**, *253*. <https://doi.org/10.1016/j.mseb.2020.114497>.
- (137) Shah, A. A.; Bhatti, M. A.; Tahira, A.; Chandio, A. D.; Channa, I. A.; Sahito, A. G.; Chalangar, E.; Willander, M.; Nur, O.; Ibupoto, Z. H. Facile Synthesis of Copper Doped ZnO Nanorods for the Efficient Photo Degradation of Methylene Blue and Methyl Orange. *Ceram Int* **2020**, *46* (8), 9997–10005. <https://doi.org/10.1016/j.ceramint.2019.12.024>.
- (138) Lin, J.; Luo, Z.; Liu, J.; Li, P. Photocatalytic Degradation of Methylene Blue in Aqueous Solution by Using ZnO-SnO₂ Nanocomposites. *Mater Sci Semicond Process* **2018**, *87*, 24–31. <https://doi.org/10.1016/j.mssp.2018.07.003>.
- (139) Goswami, M. Enhancement of Photocatalytic Activity of Synthesized Cobalt Doped Zinc Oxide Nanoparticles under Visible Light Irradiation. *Opt Mater (Amst)* **2020**, *109*. <https://doi.org/10.1016/j.optmat.2020.110400>.
- (140) Domõ Ânguez, C.; Garcõ Âa, J.; Pedraz, M. A.; Torres, A.; Ân, M. A. G. *Photocatalytic Oxidation of Organic Pollutants in Water*.
- (141) Hariharan, C. Photocatalytic Degradation of Organic Contaminants in Water by ZnO Nanoparticles: Revisited. *Appl Catal A Gen* **2006**, *304* (1–2), 55–61. <https://doi.org/10.1016/j.apcata.2006.02.020>.

- (142) El-Kemary, M.; El-Shamy, H.; El-Mehasseb, I. Photocatalytic Degradation of Ciprofloxacin Drug in Water Using ZnO Nanoparticles. *J Lumin* **2010**, *130* (12), 2327–2331. <https://doi.org/10.1016/j.jlumin.2010.07.013>.
- (143) Akmehmet Balcioglu, I.; Arslan, I. *Application of Photocatalytic Oxidation Treatment to Pretreated and Raw Effluents from the Kraft Bleaching Process and Textile Industry*.
- (144) Abdel Messih, M. F.; Ahmed, M. A.; Soltan, A.; Anis, S. S. Synthesis and Characterization of Novel Ag/ZnO Nanoparticles for Photocatalytic Degradation of Methylene Blue under UV and Solar Irradiation. *Journal of Physics and Chemistry of Solids* **2019**, *135*. <https://doi.org/10.1016/j.jpics.2019.109086>.
- (145) Gerischer, H. *PHOTOELECTROCHEMICAL CATALYSIS OF THE OXIDATION OF ORGANIC MOLECULES BY OXYGEN ON SMALL SEMICONDUCTOR PARTICLES WITH TiO₂ AS AN EXAMPLE**.
- (146) Siva, N.; Sakthi, D.; Ragupathy, S.; Arun, V.; Kannadasan, N. Synthesis, Structural, Optical and Photocatalytic Behavior of Sn Doped ZnO Nanoparticles. *Mater Sci Eng B Solid State Mater Adv Technol* **2020**, *253*. <https://doi.org/10.1016/j.mseb.2020.114497>.
- (147) Perillo, P. M.; Atia, M. N. Solar-Assisted Photodegradation of Methyl Orange Using Cu-Doped ZnO Nanorods. *Mater Today Commun* **2018**, *17*, 252–258. <https://doi.org/10.1016/j.mtcomm.2018.09.010>.
- (148) Robinson, T.; McMullan, G.; Marchant, R.; Nigam, P. *Remediation of Dyes in Textile Effluent: A Critical Review on Current Treatment Technologies with a Proposed Alternative*.
- (149) Goncalves, M. S. T.; Oliveira-Campos, A. M. F.; Pinto, E. M. M. S.; Plasmancina, P. M. S.; Jo~o, M.; Queiroz, R. P. *PHOTOCHEMICAL TREATMENT OF SOLUTIONS OF AZO DYES CONTAINING TiO₂*; 1999; Vol. 39.

- (150) Robinson, T.; McMullan, G.; Marchant, R.; Nigam, P. *Remediation of Dyes in Textile Effluent: A Critical Review on Current Treatment Technologies with a Proposed Alternative*.
- (151) Gupta, V. K.; Ali, I.; Saini, V. K.; Van Gerven, T.; Van Bruggen, B. Der; Vandecasteele, C. Removal of Dyes from Wastewater Using Bottom Ash. *Ind Eng Chem Res* **2005**, *44* (10), 3655–3664. <https://doi.org/10.1021/ie0500220>.
- (152) Vignesh, K.; Rajarajan, M.; Suganthi, A. Visible Light Assisted Photocatalytic Performance of Ni and Th Co-Doped ZnO Nanoparticles for the Degradation of Methylene Blue Dye. *Journal of Industrial and Engineering Chemistry* **2014**, *20* (5), 3826–3833. <https://doi.org/10.1016/j.jiec.2013.12.086>.
- (153) Sun, F.; Sun, B.; Hu, J.; He, Y.; Wu, W. Organics and Nitrogen Removal from Textile Auxiliaries Wastewater with A2O-MBR in a Pilot-Scale. *J Hazard Mater* **2015**, *286*, 416–424. <https://doi.org/10.1016/j.jhazmat.2015.01.031>.
- (154) Sivakumar, R.; Lee, N. Y. Adsorptive Removal of Organic Pollutant Methylene Blue Using Polysaccharide-Based Composite Hydrogels. *Chemosphere* **2022**, *286*. <https://doi.org/10.1016/j.chemosphere.2021.131890>.
- (155) Chandekar, K. V.; Shkir, M.; Al-Shehri, B. M.; AlFaify, S.; Halor, R. G.; Khan, A.; Al-Namshah, K. S.; Hamdy, M. S. Visible Light Sensitive Cu Doped ZnO: Facile Synthesis, Characterization, and High Photocatalytic Response. *Mater Charact* **2020**, *165*. <https://doi.org/10.1016/j.matchar.2020.110387>.
- (156) Suresh, M.; Sivasamy, A. Fabrication of Graphene Nanosheets Decorated by Nitrogen-Doped ZnO Nanoparticles with Enhanced Visible Photocatalytic Activity for the Degradation of Methylene Blue Dye. *J Mol Liq* **2020**, *317*. <https://doi.org/10.1016/j.molliq.2020.114112>.

- (157) Sriram, S.; K.C., L.; Thayumanavan, A. Experimental and Theoretical Investigations of Photocatalytic Activity of Cu Doped ZnO Nanoparticles. *Optik (Stuttg)* **2017**, *139*, 299–308. <https://doi.org/10.1016/j.ijleo.2017.04.013>.
- (158) Qi, K.; Xing, X.; Zada, A.; Li, M.; Wang, Q.; Liu, S. yuan; Lin, H.; Wang, G. Transition Metal Doped ZnO Nanoparticles with Enhanced Photocatalytic and Antibacterial Performances: Experimental and DFT Studies. *Ceram Int* **2020**, *46* (2), 1494–1502. <https://doi.org/10.1016/j.ceramint.2019.09.116>.
- (159) Rani, M.; Shanker, U. Sun-Light Driven Rapid Photocatalytic Degradation of Methylene Blue by Poly (Methyl Methacrylate)/Metal Oxide Nanocomposites. *Colloids Surf A Physicochem Eng Asp* **2018**, *559*, 136–147. <https://doi.org/10.1016/j.colsurfa.2018.09.040>.
- (160) Vignesh, K.; Rajarajan, M.; Suganthi, A. Visible Light Assisted Photocatalytic Performance of Ni and Th Co-Doped ZnO Nanoparticles for the Degradation of Methylene Blue Dye. *Journal of Industrial and Engineering Chemistry* **2014**, *20* (5), 3826–3833. <https://doi.org/10.1016/j.jiec.2013.12.086>.
- (161) Bojorge, C. D.; Cánepa, H. R.; Gilabert, U. E.; Silva, D.; Dalchiele, E. A.; Marotti, R. E. Synthesis and Optical Characterization of ZnO and ZnO Nanocrystalline Films Obtained by the Sol-Gel Dip-Coating Process. In *Journal of Materials Science: Materials in Electronics*; 2007; Vol. 18, pp 1119–1125. <https://doi.org/10.1007/s10854-007-9274-9>.
- (163) Srivastava, V.; Gusain, D.; Sharma, Y. C. Synthesis, Characterization and Application of Zinc Oxide Nanoparticles (n-ZnO). *Ceram Int* **2013**, *39* (8), 9803–9808. <https://doi.org/10.1016/j.ceramint.2013.04.110>.
- (164) Al-Gaashani, R.; Radiman, S.; Daud, A. R.; Tabet, N.; Al-Douri, Y. XPS and Optical Studies of Different Morphologies of ZnO Nanostructures Prepared by Microwave

- Methods. *Ceram Int* **2013**, 39 (3), 2283–2292.
<https://doi.org/10.1016/j.ceramint.2012.08.075>.
- (165) Hsieh, P. T.; Chen, Y. C.; Kao, K. S.; Wang, C. M. Luminescence Mechanism of ZnO Thin Film Investigated by XPS Measurement. *Appl Phys A Mater Sci Process* **2008**, 90 (2), 317–321. <https://doi.org/10.1007/s00339-007-4275-3>.
- (166) Zhang, Y.; Mao, X.; Liu, J.; Wang, M.; Qian, Y.; Gao, C.; Qi, Y. Direct Determination of Cadmium in Foods by Solid Sampling Electrothermal Vaporization Inductively Coupled Plasma Mass Spectrometry Using a Tungsten Coil Trap. *Spectrochim Acta Part B At Spectrosc* **2016**, 118, 119–126. <https://doi.org/10.1016/j.sab.2016.02.017>.
- (167) Le, A. T.; Le, T. D. H.; Cheong, K. Y.; Pung, S. Y. Immobilization of Zinc Oxide-Based Photocatalysts for Organic Pollutant Degradation: A Review. *J Environ Chem Eng* **2022**, 10 (5). <https://doi.org/10.1016/j.jece.2022.108505>.
- (168) Mustapha, S.; Ndamitso, M. M.; Abdulkareem, A. S.; Tijani, J. O.; Shuaib, D. T.; Ajala, A. O.; Mohammed, A. K. Application of TiO₂ and ZnO Nanoparticles Immobilized on Clay in Wastewater Treatment: A Review. *Applied Water Science*. Springer Science and Business Media Deutschland GmbH January 1, 2020. <https://doi.org/10.1007/s13201-019-1138-y>.
- (169) Aghdasi, S.; Shokri, M. *IRANIAN JOURNAL OF CATALYSIS Photocatalytic Degradation of Ciprofloxacin in the Presence of Synthesized ZnO Nano catalyst: The Effect of Operational Parameters*; 2016; Vol. 6.
- (170) Liu, D.; Yang, X.; Zhang, L.; Tang, Y.; He, H.; Liang, M.; Tu, Z.; Zhu, H. Immobilization of Biomass Materials for Removal of Refractory Organic Pollutants from Wastewater.

- International Journal of Environmental Research and Public Health*. MDPI November 1, 2022. <https://doi.org/10.3390/ijerph192113830>.
- (171) Al Sharabati, M.; Abokwiek, R.; Al-Othman, A.; Tawalbeh, M.; Karaman, C.; Orooji, Y.; Karimi, F. Biodegradable Polymers and Their Nanocomposites for the Removal of Endocrine-Disrupting Chemicals (EDCs) from Wastewater: A Review. *Environ Res* **2021**, *202*. <https://doi.org/10.1016/j.envres.2021.111694>.
- (172) Mei, J.; Tao, Y.; Gao, C.; Zhu, Q.; Zhang, H.; Yu, J.; Fang, Z.; Xu, H.; Wang, Y.; Li, G. Photo-Induced Dye-Sensitized BiPO₄/BiOCl System for Stably Treating Persistent Organic Pollutants. *Appl Catal B* **2021**, *285*. <https://doi.org/10.1016/j.apcatb.2020.119841>.
- (173) Tan, K. A.; Morad, N.; Ooi, J. Q. Phytoremediation of Methylene Blue and Methyl Orange Using Eichhornia Crassipes. *International Journal of Environmental Science and Development* **2016**, *7* (10), 724–728. <https://doi.org/10.18178/ijesd.2016.7.10.869>.
- (174) Tan, K. A.; Morad, N.; Ooi, J. Q. Phytoremediation of Methylene Blue and Methyl Orange Using Eichhornia Crassipes. *International Journal of Environmental Science and Development* **2016**, *7* (10), 724–728. <https://doi.org/10.18178/ijesd.2016.7.10.869>.
- (175) Kobayashi, H.; Ogawa, M.; Alford, R.; Choyke, P. L.; Urano, Y. New Strategies for Fluorescent Probe Design in Medical Diagnostic Imaging. *Chem Rev* **2010**, *110* (5), 2620–2640. <https://doi.org/10.1021/cr900263j>.
- (176) Bel, N.; Mohamed, H.; Ouni, S.; Bouzid, M.; Bouzidi, M.; Bonilla-Petriciolet, A. Adsorption and Photocatalytic Degradation of an Industrial Azo Dye Using Colloidal Semiconductor Nanocrystals. **2022**. <https://doi.org/10.21203/rs.3.rs-1057236/v2>.

- (177) Drumond Chequer, F. M.; Dorta, D. J.; Palma De Oliveira, D. *2 Azo Dyes and Their Metabolites: Does the Discharge of the Azo Dye into Water Bodies Represent Human and Ecological Risks?*
- (178) Adeel, S.; Gulzar, T.; Azeem, M.; Fazal-ur-Rehman; Saeed, M.; Hanif, I.; Iqbal, N. Appraisal of Marigold Flower Based Lutein as Natural Colorant for Textile Dyeing under the Influence of Gamma Radiations. *Radiation Physics and Chemistry* **2017**, *130*, 35–39. <https://doi.org/10.1016/j.radphyschem.2016.07.010>.
- (179) Mouri, C.; Mozaffarian, V.; Zhang, X.; Laursen, R. Characterization of Flavonols in Plants Used for Textile Dyeing and the Significance of Flavonol Conjugates. *Dyes and Pigments* **2014**, *100* (1), 135–141. <https://doi.org/10.1016/j.dyepig.2013.08.025>.
- (180) Shahid-Ul-Islam; Shahid, M.; Mohammad, F. Perspectives for Natural Product Based Agents Derived from Industrial Plants in Textile Applications - A Review. *Journal of Cleaner Production*. October 15, 2013, pp 2–18. <https://doi.org/10.1016/j.jclepro.2013.06.004>.
- (181) Rasheed, T.; Shafi, S.; Bilal, M.; Hussain, T.; Sher, F.; Rizwan, K. Surfactants-Based Remediation as an Effective Approach for Removal of Environmental Pollutants—A Review. *Journal of Molecular Liquids*. Elsevier B.V. November 15, 2020. <https://doi.org/10.1016/j.molliq.2020.113960>.
- (182) Rochester, J. R. Bisphenol A, and Human Health: A Review of the Literature. *Reproductive Toxicology*. December 2013, pp 132–155. <https://doi.org/10.1016/j.reprotox.2013.08.008>.
- (183) Byun, Y.; Zhang, Y.; Geng, X. Plasticization and Polymer Morphology. In *Innovations in Food Packaging: Second Edition*; Elsevier Ltd., 2013; pp 87–108. <https://doi.org/10.1016/B978-0-12-394601-0.00005-9>.

- (184) Gingrich, J.; Ticiani, E.; Veiga-Lopez, A. Placenta Disrupted: Endocrine Disrupting Chemicals and Pregnancy. *Trends in Endocrinology and Metabolism*. Elsevier Inc. July 1, 2020, pp 508–524. <https://doi.org/10.1016/j.tem.2020.03.003>.
- (185) Welshons, W. V.; Thayer, K. A.; Judy, B. M.; Taylor, J. A.; Curran, E. M.; vom Saal, F. S. Large Effects from Small Exposures. I. Mechanisms for Endocrine-Disrupting Chemicals with Estrogenic Activity. *Environmental Health Perspectives*. Public Health Services, US Dept of Health and Human Services August 1, 2003, pp 994–1006. <https://doi.org/10.1289/ehp.5494>.
- (186) Cooper, J. E.; Kendig, E. L.; Belcher, S. M. Assessment of Bisphenol A Released from Reusable Plastic, Aluminium and Stainless-Steel Water Bottles. *Chemosphere* **2011**, 85 (6), 943–947. <https://doi.org/10.1016/j.chemosphere.2011.06.060>.
- (187) Gogate, P. R.; Pandit, A. B. A Review of Imperative Technologies for Wastewater Treatment I: Oxidation Technologies at Ambient Conditions. *Advances in Environmental Research* **2004**, 8 (3–4), 501–551. [https://doi.org/10.1016/S1093-0191\(03\)00032-7](https://doi.org/10.1016/S1093-0191(03)00032-7).
- (188) Schug, T. T.; Janesick, A.; Blumberg, B.; Heindel, J. J. Endocrine Disrupting Chemicals and Disease Susceptibility. *Journal of Steroid Biochemistry and Molecular Biology*. November 2011, pp 204–215. <https://doi.org/10.1016/j.jsbmb.2011.08.007>.
- (189) Chouhan, S.; Yadav, S. K.; Prakash, J.; Swati; Singh, S. P. Effect of Bisphenol A on Human Health, and Its Degradation by Microorganisms: A Review. *Annals of Microbiology*. March 2014, pp 13–21. <https://doi.org/10.1007/s13213-013-0649-2>.
- (190) Garrick, D.; Siebentritt, M. A.; Aylward, B.; Bauer, C. J.; Purkey, A. Water Markets and Freshwater Ecosystem Services: Policy Reform and Implementation in the Columbia and

- Murray-Darling Basins. *Ecological Economics* **2009**, *69* (2), 366–379. <https://doi.org/10.1016/j.ecolecon.2009.08.004>.
- (191) Kumar, V.; Singh, E.; Singh, S.; Pandey, A.; Bhargava, P. C. Micro- and Nano-Plastics (MNPs) as Emerging Pollutant in Ground Water: Environmental Impact, Potential Risks, Limitations and Way Forward towards Sustainable Management. *Chemical Engineering Journal*. Elsevier B.V. March 1, 2023. <https://doi.org/10.1016/j.cej.2023.141568>.
- (192) Velusamy, S.; Roy, A.; Sundaram, S.; Kumar Mallick, T. A Review on Heavy Metal Ions and Containing Dyes Removal Through Graphene Oxide-Based Adsorption Strategies for Textile Wastewater Treatment. *Chemical Record*. John Wiley and Sons Inc July 1, 2021, pp 1570–1610. <https://doi.org/10.1002/tcr.202000153>.
- (193) Zheng, M.; Xu, L.; Chen, C.; Labiadh, L.; Yuan, B.; Fu, M. L. MOFs and GO-Based Composites as Deliberated Materials for the Adsorption of Various Water Contaminants. *Separation and Purification Technology*. Elsevier B.V. August 1, 2022. <https://doi.org/10.1016/j.seppur.2022.121187>.
- (194) Khan, S. A.; Shah, L. A. Polymer Membranes for Wastewater Treatment; 2021; pp 175–194. https://doi.org/10.1007/978-981-16-3164-1_6.
- (195) Yang, F.; Hu, G.; He, H.; Yi, M.; Ge, Y.; Ran, L.; Peng, K. Effect of Amorphous Carbon on the Tensile Behavior of Polyacrylonitrile (PAN)-Based Carbon Fibers. *J Mater Sci* **2019**, *54* (11), 8800–8813. <https://doi.org/10.1007/s10853-018-03256-z>.
- (196) Alberti, S.; Rucco, M.; Di Carro, M.; Magi, E.; Ferretti, M.; Benedetti, B. A Multidisciplinary Approach to the Environmental Problem of Emerging Pollution: Synthesis and Application of a Novel Composite Photocatalyst and the Case Study of

- Salbutamol Degradation. *J Environ Chem Eng* **2023**, *11* (3).
<https://doi.org/10.1016/j.jece.2023.110262>.
- (197) Naghdi, S.; Shahrestani, M. M.; Zendeabad, M.; Djahaniani, H.; Kazemian, H.; Eder, D. Recent Advances in Application of Metal-Organic Frameworks (MOFs) as Adsorbent and Catalyst in Removal of Persistent Organic Pollutants (POPs). *Journal of Hazardous Materials*. Elsevier B.V. January 15, 2023. <https://doi.org/10.1016/j.jhazmat.2022.130127>.
- (198) Liang, M. K.; Limo, M. J.; Sola-Rabada, A.; Roe, M. J.; Perry, C. C. New Insights into the Mechanism of ZnO Formation from Aqueous Solutions of Zinc Acetate and Zinc Nitrate. *Chemistry of Materials* **2014**, *26* (14), 4119–4129. <https://doi.org/10.1021/cm501096p>.
- (199) Xia, J.; Di, J.; Li, H.; Xu, H.; Li, H.; Guo, S. Ionic Liquid-Induced Strategy for Carbon Quantum Dots/BiOX (X=Br, Cl) Hybrid Nanosheets with Superior Visible Light-Driven Photocatalysis. *Appl Catal B* **2016**, *181*, 260–269.
<https://doi.org/10.1016/j.apcatb.2015.07.035>.
- (200) Bang, S.; Lee, S.; Ko, Y.; Park, J.; Shin, S.; Seo, H.; Jeon, H. *Photocurrent Detection of Chemically Tuned Hierarchical ZnO Nanostructures Grown on Seed Layers Formed by Atomic Layer Deposition*; 2012. <http://www.nanoscalereslett.com/content/7/1/290>.
- (201) Wong, Y. C.; Szeto, Y. S.; Cheung, W. H.; McKay, G. Equilibrium Studies for Acid Dye Adsorption onto Chitosan. *Langmuir* **2003**, *19* (19), 7888–7894.
<https://doi.org/10.1021/la030064y>.
- (202) Siyal, A. A.; Shamsuddin, M. R.; Low, A.; Rabat, N. E. A Review on Recent Developments in the Adsorption of Surfactants from Wastewater. *Journal of Environmental Management*. Academic Press January 15, 2020. <https://doi.org/10.1016/j.jenvman.2019.109797>.

- (204) Hyder, A. H. M. G.; Begum, S. A.; Egiebor, N. O. Adsorption Isotherm and Kinetic Studies of Hexavalent Chromium Removal from Aqueous Solution onto Bone Char. *J Environ Chem Eng* **2015**, *3* (2), 1329–1336. <https://doi.org/10.1016/j.jece.2014.12.005>.
- (205) Ramutshatsha-Makhwedzha, D.; Mavhungu, A.; Moropeng, M. L.; Mbaya, R. Activated Carbon Derived from Waste Orange and Lemon Peels for the Adsorption of Methyl Orange and Methylene Blue Dyes from Wastewater. *Heliyon* **2022**, *8* (8). <https://doi.org/10.1016/j.heliyon.2022.e09930>.
- (206) Zhou, T.; Lu, W.; Liu, L.; Zhu, H.; Jiao, Y.; Zhang, S.; Han, R. Effective Adsorption of Light Green Anionic Dye from Solution by CPB Modified Peanut in Column Mode. *J Mol Liq* **2015**, *211*, 909–914. <https://doi.org/10.1016/j.molliq.2015.08.018>.
- (207) Wang, J.; Wang, S. Reactive Species in Advanced Oxidation Processes: Formation, Identification and Reaction Mechanism. *Chemical Engineering Journal*. Elsevier B.V. December 1, 2020. <https://doi.org/10.1016/j.cej.2020.126158>.
- (208) Ganiyu, S. O.; Van Hullebusch, E. D.; Cretin, M.; Esposito, G.; Oturan, M. A. Coupling of Membrane Filtration and Advanced Oxidation Processes for Removal of Pharmaceutical Residues: A Critical Review. *Sep Purif Technol* **2015**, *156*, 891–914. <https://doi.org/10.1016/j.seppur.2015.09.059>.
- (209) Oller, I.; Malato, S.; Sánchez-Pérez, J. A. Combination of Advanced Oxidation Processes and Biological Treatments for Wastewater Decontamination-A Review. *Science of the Total Environment*. September 15, 2011, pp 4141–4166. <https://doi.org/10.1016/j.scitotenv.2010.08.061>.

- (210) Ballerini, G.; Ogle, K.; Barthés-Labrousse, M. G. The Acid-Base Properties of the Surface of Native Zinc Oxide Layers: An XPS Study of Adsorption of 1,2-Diaminoethane. *Appl Surf Sci* **2007**, *253* (16), 6860–6867. <https://doi.org/10.1016/j.apsusc.2007.01.126>.
- (211) Bang, S.; Lee, S.; Ko, Y.; Park, J.; Shin, S.; Seo, H.; Jeon, H. *Photocurrent Detection of Chemically Tuned Hierarchical ZnO Nanostructures Grown on Seed Layers Formed by Atomic Layer Deposition*; 2012. <http://www.nanoscalereslett.com/content/7/1/290>.

Appendix

Characterization Techniques

Transmission electron microscopy (TEM) images were obtained using a Hitachi H-7650 with an acceleration voltage of 80 kV. Carbon-filmed copper grids with 200 mesh were used for TEM imaging. Scanning Electron Microscopy (SEM) images and the Energy Dispersive X-ray (EDX) experiments were carried out using a JEOL JSM-IT100 microscope was used. Carbon tape was used as the substrate for the SEM imaging. Powder X-ray diffraction (XRPD) spectrum was obtained by using Bruker D8 Discover X-ray diffractometer with Cu K α radiation ($\lambda = 0.15418$ nm). The X-ray photoelectron spectroscopy (XPS) analysis was performed in Thermo Scientific™ K-alpha™ equipment using a monochromatic Al Ka X-ray source. The survey spectra were obtained with 130-eV pass energy, while high-resolution analyses for specific core levels were performed at 20-eV pass energy. An argon ions flood gun was used to avert surface charging. All binding energies were corrected with reference to carbon 1s at 284.8 eV. Elemental analysis was performed using PerkinElmer Optima 4300 DV ICP-OES UV–Visible spectroscopic analysis was performed on Agilent Cary 50 Conc UV–Visible Spectrophotometer. Standard quartz cuvette (10 mm path length) was used as the sample holder and the measurements were in the ranges of 200–800 nm with an accuracy of 1 nm.

Licenses, Copyright, and Permissions

Chapter 2 was published in the Journal of Molecular Liquids and reproduced from “Journal of Molecular Liquids 307 (2020): 112931.” with permission from the Journal of Molecular Liquids.

Vita

Kazi Afroza Sultana was born and raised in Gazipur, Bangladesh. She earned her Bachelor of Science degree with Honors in pharmacy from Gono Bishwabidyalay, Dhaka, Bangladesh in 2012. Later, she earned a master's degree in Pharmaceutical Technology from the University of Asia Pacific, Dhaka, Bangladesh. To pursue her Doctoral Degree in Environmental Science and Engineering, she joined the University of Texas at El Paso in the spring of 2019. Her research interest was the synthesis of advanced functional nanomaterials and their applications in sustainable water treatment, and energy storage systems. She has published four research articles in peer-reviewed journals and currently working on three manuscripts. While at UTEP, Kazi Afroza Sultana had the opportunity to work with undergraduate students as a teaching assistant and she had the mentoring experience with undergraduate students in different research projects in the lab. During her leisure time, she loves to spend time with her family.

Contact Information: sultanakazi2015@gmail.com